

Multi-species electrochemical reaction modeling using Lattice Boltzmann Method

Study of transport phenomena in alkaline water electrolyzer

Vignesh Murugesan

Multi-species electrochemical reaction modeling using Lattice Boltzmann Method

Study of transport phenomena in alkaline water electrolyzer

by

Vignesh Murugesan

Thesis report

in partial fulfillment of the requirement for the degree of
Master of Science in mechanical engineering
(Energy, Flow, and Process Technology)

Faculty supervisors:	Prof. dr. ir. Johan Padding, Dr. ir. Remco Hartkamp,	TU Delft TU Delft
Daily supervisor:	Ir. Arvind Pari,	TU Delft
Thesis Committee:	Prof. dr. ir. Johan Padding, Dr. ir. Remco Hartkamp, Dr. ir. Bijoy Bera.	TU Delft TU Delft TU Delft

Acknowledgement

I would like to take this opportunity to express my sincere gratitude to all those who have contributed to the completion of this thesis. Their support, guidance, and encouragement have been invaluable throughout this journey.

I am deeply grateful to my advisors Prof. Johan, Dr. Remco, Ir. Arvind, for their unwavering support and invaluable guidance. Their expertise, insightful feedback, and patient mentoring have been instrumental in shaping this research. I'm also grateful for the code debugging sessions that we used to have every Friday. Honestly after the meetings with you, my brain works better in fixing the issues.

I extend my heartfelt thanks to the members of my thesis committee, Prof. dr. ir. J. T. Padding, Dr. R.M. (Remco) Hartkamp, and Dr. ir. Bijoy Bera, for their valuable insights and constructive critiques that have significantly improved the quality of this work.

I would also like to express my appreciation to my colleagues, friends and flex room boys who have been a source of encouragement and support. Their discussions, feedback, and camaraderie have enriched my research experience. I am indebted to TU Delft and EFPT for providing the necessary resources and facilities that facilitated the execution of this research.

Lastly, I want to express my deepest appreciation to my family. Their unwavering belief in me and their constant encouragement have been my driving force. I also sincerely thank Mr. RadhaKrishnan Govindaraj for the immense support and advice, paving a better path for this journey in my life. In conclusion, this work would not have been possible without the support of these individuals and organizations. Their contributions have been vital in shaping the outcome of this thesis.

Abstract

Enhancing the efficiency of industrial water electrolysis for hydrogen production is vital for the energy transition. In Alkaline Water Electrolysis (AWE), hydrogen is produced at the cathode, and the bubbles are formed when the local hydrogen concentration exceeds the solubility limit. It is important to understand the exact local conditions that result in the nucleation of bubbles in this multi-phase and reactive system. With modeling, it is possible to gain insight into the relation between various local properties, but the model needs to include all relevant physics and chemistry. Thus, this work focuses on the multi-species electrochemical transport phenomena with reaction occurring on the electrode-electrolyte interface.

The electrochemical transport phenomena and the bubble nucleation are meso-scale phenomena occurring at the electrode-electrolyte interface. Lattice Boltzmann Method (LBM) is well suited for modeling meso-scale behavior but it is computationally memory expensive. Consequently, a hybrid approach combining Finite Difference Method (FDM) and LBM has been developed to simulate transport phenomena in the migration-diffusion problem with heterogeneous reaction kinetics. The Debye-Hückel theory is used as a benchmark to validate the developed model. Subsequently, the model is employed to simulate the transport phenomena occurring in the hydrogen half-cell of AWE, with a specific focus on the Hydrogen Evolution Reaction (HER) governed by the Butler-Volmer kinetics equation.

The model captures the dynamic evolution of physical parameters such as electric potential, concentration of species, and fluxes within the system particularly in the Electric-Double layer (EDL). The effect of electrode potential on the distribution of species involved in the reaction are studied by performing simulations for different electrode potential. The influence of secondary fluxes on the species distribution is studied by implementing a spatially varying boundary condition to the reacting site. Finally, the formulated methodology is extended to solve a multi-phase system with species transportation occurring around a catalyst particle.

Contents

List of Figures	vii
List of Tables	ix
1 General introduction	1
1.1 Water electrolysis	2
1.1.1 Solid oxide electrolyzer cell (SOEC)	3
1.1.2 Polymer electrolyte membrane (PEM) water electrolysis	4
1.1.3 Alkaline water electrolysis (AWE)	4
1.2 Thesis scope	5
1.2.1 Thesis vision	6
1.2.2 Structure of the report	6
2 Electrochemistry	8
2.1 Thermodynamics and potential	8
2.2 Ion transport mechanisms	9
2.2.1 Migration	9
2.2.2 Diffusion	9
2.2.3 Convection	9
2.3 Electrode kinetics, reaction rate	10
2.3.1 Butler-Volmer equation	10
2.3.2 Effect of double layer on kinetics	12
2.4 Transport phenomena	13
2.4.1 Dilute solution theory	13
3 Lattice Boltzmann method	15
3.1 Lattice-Boltzmann equation	15
3.2 Lattice configurations	16
3.2.1 One dimensional lattice	16
3.2.2 Two dimensional lattice	16
3.2.3 Three dimensional lattice	17
3.3 BGK Stability	18
3.4 Similitude	19
3.5 Boundary conditions	20
4 Diffusion	21
4.1 Scaling	21
4.2 BGK-LBM scheme for diffusion problem	22
4.3 Initialization	22
4.4 Collision \rightarrow Streaming	22
4.5 Boundary Conditions	23
4.6 Implementation and validation	25
4.6.1 One-dimensional diffusion problem	25
4.6.2 Two-dimensional diffusion problem	26

5	Multi-species migration-diffusion	27
5.1	Poisson's equation solver	27
5.1.1	Pseudo-transient BGK-LBM approach	27
5.1.2	FDM in lattice space	29
5.2	Nernst-Planck model	31
5.2.1	Scaling	32
5.2.2	BGK-LBM scheme for Nernst-Planck Model	32
5.2.3	Common vs different relaxation time for species	33
5.2.4	Initialization	33
5.2.5	Collision \rightarrow Streaming	33
5.2.6	Boundary condition	34
5.3	Migration-diffusion problem with reaction kinetics	36
6	Validation: ion migration	38
6.1	Debye-Hückel theory	38
6.2	Grid independence study	39
6.3	Ion migration	39
7	HER: Constant reaction rate	42
7.1	Low cathode potential	43
7.1.1	Electric field and potential	44
7.1.2	Species concentration	45
7.2	High cathode potential	46
8	HER: species transport with kinetics	50
8.1	Uniform electrode potential	50
8.1.1	Influence of electrode potential Φ_o	53
8.2	Spatially varying boundary condition	54
9	Heterogeneous reaction on a catalyst particle	58
9.1	Modeling Methodology	59
9.1.1	Bounce-Back	59
9.1.2	Modeling species flux	60
9.2	Results	61
9.2.1	Electric potential distribution	61
9.2.2	Species concentration	62
10	Conclusion and outlook	64
10.1	Outlook	65
10.1.1	Steric effects	65
10.1.2	Multi-relaxation time-LBM	66
10.1.3	Parallel computing	66
	Bibliography	69
A	Results for $\Phi_s = [-0.75, -0.85, -0.9]$ V	70
A.1	Surface potential $\Phi_s = -0.9$ V	70
A.2	For surface potential $\Phi_s = -0.85$ V	71
A.3	For surface potential $\Phi_s = -0.75$ V	71
B	Spatially varying Boundary condition	73
B.1	Potential distribution	73
B.2	H ₂ concentration density	73
B.2.1	H ₂ O concentration density	74
B.3	OH ⁻ concentration density	74
B.4	k ⁺ concentration density	74

List of Figures

1.1	Brands of H ₂	1
1.2	Green H ₂ Production, conversion and end-use	3
1.3	operating principle of (a)AWE (b)PEM (c)SOEC	3
1.4	Effect of current density on the hydrogen production rate (V_{H_2}) and the cost (C_{H_2})	5
1.5	Modeling approach based on the required resolution of physics	6
2.1	AWE resistance analogous to electrical resistance	8
2.2	Plot relating the current density and surface over-potential at 25°C	10
2.3	electric double layer (EDL) near cathode	12
3.1	Lattice configurations for 1-D lattice	16
3.2	Lattice configurations for 2-D lattice	17
3.3	Lattice configurations for 3-D lattice	17
3.4	distribution function evolution	19
3.5	Sketch of stable regime	19
4.1	Periodic boundary condition for D2Q4 and D2Q5 lattice.	24
4.2	Diffusion Problem LBM simulation flowchart.	24
4.3	Domain for one-dimensional diffusion problem.	25
4.4	Dimensionless concentration distribution from FDM, D1Q2 and D1Q3 LBM at time $t = 200$ lu.	25
4.5	Domain description and FDM simulation result at $t = 1000$ lu	26
4.6	Two-dimensional BGK-LBM simulation result at $t = 1000$ lu.	26
5.1	Pseudo-transient BGK-LBM simulation of poisson solver.	29
5.2	Flow chart and data exchange architecture for electro-diffusive model.	35
5.3	Data exchange between the Poisson-Nernst-Planck and reaction kinetics solver.	37
5.4	Flow chart for migration-diffusion problem with reaction.	37
6.1	Grid independence study.	39
6.2	Domain to validate LBM with Debye-Hückel theory.	40
6.3	Comparison of analytical and LBM results for ion concentration.	40
6.4	Comparison of analytical and LBM results for electric potential and charge density on logarithmic scale.	40
6.5	Comparison of analytical and LBM results for ion concentration on the logarithmic scale.	41
7.1	The solubility limit of H ₂ depending on the molarity of the KOH solution at T=298,353 K	42
7.2	Domain for simulating species transport phenomena in hydrogen half-cell.	43
7.3	(a) Electric potential with electric field quivers, (b) Electric field contour at $t=2$ μ s for $\Phi_o=-30$ mV, $ J =1000$ A/m ²	44
7.4	(a) Electric potential and charge density evolution, (b) Electric field evolution for $\Phi_o=-30$ mV, $ J =1000$ A/m ²	44
7.5	Concentration density distribution of neutral and ionic species and vector plot representing net flux at $t=2$ μ s for $\Phi_o=-30$ mV, $ J =1000$ A/m ²	45
7.6	Species concentration evolution for $\Phi_o=-30$ mV, $ J =1000$ A/m ²	46
7.7	Ionic species flux evolution for $\Phi_o=-30$ mV, $ J =1000$ A/m ²	46

7.8	(a) Φ_o ramping with time (b) Electric potential evolution, (c) Electric field evolution for $\Phi_o = -0.1$ V, $ J = 1000$ A/m ²	47
7.9	Species concentration evolution for $\Phi_o = -0.1$ V, $ J = 1000$ A/m ²	48
7.10	Migrating and diffusive flux evolution of ionic species for $\Phi_o = -0.1$ V, $ J = 1000$ A/m ²	49
7.11	Total flux evolution for OH ⁻	49
8.1	Evolution of the over and Nernst potential, current density and species reaction flux at reacting boundary for $\Phi_s = -0.8$ V and $\Phi_{\text{OHP}} = -50$ mV	51
8.2	Electric potential and electric field evolution for $\Phi_s = -0.8$ V and $\Phi_{\text{OHP}} = -50$ mV.	51
8.3	Species concentration evolution for $\Phi_s = -0.8$ V and $\Phi_{\text{OHP}} = -50$ mV.	52
8.4	Migrating and diffusive flux evolution of ionic species for $\Phi_s = -0.8$ V and $\Phi_{\text{OHP}} = -50$ mV.	52
8.5	H ₂ statistics for different overpotential (η)	53
8.6	OH ⁻ statistics for different overpotential (η)	53
8.7	sinusoidal spatial variation imposed on the potentials at reacting site and the resulting current density distribution from the kinetics solver at $t = 0.1$ μ s.	54
8.8	Electric potential distribution between the OHP and the right boundary (bulk) and the vector plot for electric field distribution at $t = 0.01$ and 0.1 μ s	54
8.9	Local concentration density of H ₂ and the vector plot for flux at $t = 0.01$ and 0.1 μ s	55
8.10	Local concentration density of H ₂ O and the vector plot for flux at $t = 0.01, 0.1$ μ s	55
8.11	Local concentration density of OH ⁻ and the vector plot for flux at $t = 0.01$ and 0.1 μ s	56
8.12	Local concentration density of K ⁺ and the vector plot for flux at $t = 0.01$ and 0.1 μ s	57
9.1	Schematic view of the porous electrode, the magnified porous structure, and simplified geometry of a catalyst particle.	58
9.2	Setup of geometry and boundary condition for hydrogen evolution heterogeneous reaction around a catalyst particle.	59
9.3	(a) Labeling of nodes to distinguish the nodes representing the electrode, electrolyte, and the electrode-electrolyte interface. (b) schematic of electrode-electrolyte boundary for bounce-back treatment of distribution functions.	59
9.4	(a) Normal species flux to the electrode-electrolyte interface and its x and y-component. (b) Choice of the distribution function to model the species flux at different radial positions on the electrode-electrolyte interface.	60
9.5	Electric potential distribution around the electrode catalyst particle at $t = 0.05, 0.1$ μ s.	61
9.6	(a) Electric potential evolution. (b) H ₂ concentration evolution for the electrode surface potential of $\Phi_s = -0.85$ V.	61
9.7	H ₂ concentration distribution around the electrode catalyst particle at $t = 0.05, 0.1$ μ s.	62
9.8	OH ⁻ concentration distribution around the electrode catalyst particle at $t = 0.05, 0.1$ μ s.	62
9.9	K ⁺ concentration distribution around the electrode catalyst particle at $t = 0.05, 0.1$ μ s.	63
9.10	(a) OH ⁻ concentration. (b) K ⁺ concentration evolution for the electrode surface potential of $\Phi_s = -0.85$ V.	63
A.1	Species concentration evolution for $\Phi_s = -0.9$ V and $\Phi_{\text{OHP}} = -50$ mV.	70
A.2	Evolution of the over and Nernst potential, current density and species reaction flux at reacting boundary, flux evolution of OH ⁻ for $\Phi_s = -0.9$ V and $\Phi_{\text{OHP}} = -50$ mV	70
A.3	Species concentration evolution for $\Phi_s = -0.85$ V and $\Phi_{\text{OHP}} = -50$ mV.	71
A.4	Evolution of the over and Nernst potential, current density and species reaction flux at reacting boundary, flux evolution of OH ⁻ for $\Phi_s = -0.85$ V and $\Phi_{\text{OHP}} = -50$ mV	71
A.5	Species concentration evolution for $\Phi_s = -0.75$ V and $\Phi_{\text{OHP}} = -50$ mV.	71
A.6	Evolution of the over and Nernst potential, current density and species reaction flux at reacting boundary, flux evolution of OH ⁻ for $\Phi_s = -0.75$ V and $\Phi_{\text{OHP}} = -50$ mV	72
B.1	Electric potential distribution between the inner diffuse layer and the right boundary (bulk) and the vector plot for electric field distribution at $t = 0.01, 0.1$ μ s	73
B.2	Local concentration density of H ₂ and the vector plot for flux at $t = 0.01, 0.1$ μ s	73
B.3	Local concentration density of H ₂ O and the vector plot for flux at $t = 0.02, 0.05, 0.07$ μ s	74
B.4	Local concentration density of OH ⁻ and the vector plot for flux at $t = 0.02, 0.05, 0.07$ μ s	74
B.5	Local concentration density of K ⁺ and the vector plot for flux at $t = 0.02, 0.05, 0.07$ μ s	74

List of Tables

2.1	Kinetics Properties for AWE.	11
2.2	AWE transport properties for Dilute electrolyte theory @ 80°C.	14
6.1	Physical parameters and the corresponding lattice values for Debye-Hückel validation . . .	39
7.1	Species properties involved in hydrogen half-cell transport phenomena.	43
8.1	Boundary condition definition at the left boundary for Poisson-Nernst-Planck model with reaction kinetics.	50

Nomenclature

Abbreviations

AWE	Alkaline Water Electrolysis
BC	Boundary Condition
BGK	Bhatnagar, Gross, and Krook
CCS	Carbon Capture and Storage
CFD	Computational Fluid Dynamics
DEM	Discrete Element Method
DPD	Dissipative particle Dynamics
EDL	Electric Double Layer
FDM	Finite Difference Method
GHG	Green House Gas
HER	Hydrogen Evolution Reaction
IHP	Inner Helmholtz Plane
LB	Lattice Boltzmann
LBE	Lattice Boltzmann Equation
LBM	Lattice Boltzmann Method
MD	Molecular Dynamics
MRT	Multi Relaxation Time
MSR	Methane Steam Reforming
OER	Oxygen Evolution Reaction
OHP	Outer Helmholtz Plane
PDE	Partial Differential Equation
PEM	Polymer Electrolyte Member
SMPNP	Size Modified Poisson Nernst Planck
SOEC	Solid Oxide Electrolyzer Cell

SPH	Smoothed Particle Hydrodynamics
SRT	Single Relaxation Time
TRT	Two Relaxation Time

Chemicals

CH ₄	Methane
CO	Carbon monoxide
CO ₂	Carbon dioxide
e ⁻	Electron
H ₂	Hydrogen
H ₂ O	Water
K ⁺	Potassium ion
O ₂	Oxygen
OH ⁻	Hydroxide ion
Y ₄ O ₃	Yttrium (III) oxide
ZrO ₂	Zirconia

Symbols

α	Transfer coefficient (-)
ϵ	Permittivity of electrolyte (C ² s ² /kg m ³)
η	Over-potential (V)
λ	Debye length (m)
E	Electric field (V/m)
e	Streaming velocity in lattice space (lu)
J	Current density (A/m ²)
u_ϕ	Migration velocity of ion (m/s)
\mathcal{C}	Reference Concentration density of species (mol/m ³)
\mathcal{L}	Reference length scale (m)
\mathcal{T}	Reference time scale (s)
\mathfrak{D}_{ij}	Binary diffusive coefficient between species i and j (m ² /s)
μ	Electrochemical potential (kJ/mol)
Ω	Collision operator (lu)
Φ	Electric Potential (V)

$\Phi_{e,a}$	Equilibrium potential of anodic half-cell (V)
$\Phi_{e,c}$	Equilibrium potential of cathodic half-cell (V)
σ_e	Surface charge density (C/m ²)
τ	Relaxation time factor (lu)
ΔG	Gibbs free energy (kJ/mol)
C	Concentration density of a species (mol/m ³)
C_T	Total concentration density (mol/m ³)
C_∞	Bulk concentration density of species (mol/m ³)
D	Diffusive coefficient of a species (m ² /s)
e_s	Pseudo sound speed (lu)
f	Distribution function for species concentration (lu)
f^{eq}	Equilibrium distribution function for species concentration (lu)
h	Distribution function for electric potential (lu)
h^{eq}	Equilibrium distribution function for electric potential (lu)
N	Total flux of a species (mol/m ² s)
n	Number of electrons (-)
T	Temperature (K)
t	time (s)
V_o	Thermodynamic equilibrium cell potential (V)
w	Distribution function weight factor (lu)
Z	Valency (-)
S	Stoichiometric coefficient (m ² /s)

constants

F	Faraday constant (C/mol)
k_B	Boltzmann constant (J/K)
N_A	Avogadro number (-)
q	electron charge (C)
R	Universal gas constant (J/mol K)

Chapter 1

General introduction

Hydrogen and energy have a long shared history- powering the first internal combustion engines over 200 years ago to becoming an integral part of the modern refining industry. It is light, storable, energy-dense, and produces no direct emissions of pollutants or greenhouse gases. But for hydrogen to make a significant contribution to clean energy transitions, it needs to be adopted in sectors where it is almost entirely absent, such as transport, buildings, and power generation. Supplying hydrogen to industrial users is now a major business around the world. Demand for hydrogen, which has grown more than threefold since 1975, continues to rise—almost entirely supplied from fossil fuels, with 6% of global natural gas and 2% of global coal going to hydrogen production.[1].

Hydrogen is branded with colors such as white, green, blue, and grey depending on the production method. Green Hydrogen has been hailed as the clean energy source of the future. Hydrogen can be produced from a range of resources including fossil fuels, nuclear energy, biomass, and renewable energy sources. The resulting gas can be burned or used as a carrier to provide power. And, if generated using renewable, it can be a clean alternative to burning fossil fuels.





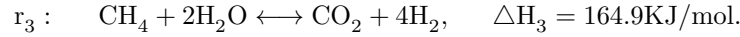
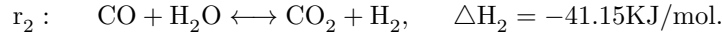
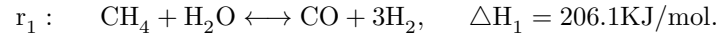
Color	GREY HYDROGEN	BLUE HYDROGEN	TURQUOISE HYDROGEN*	GREEN HYDROGEN
Process	SMR or gasification	SMR or gasification with carbon capture (85-95%)	Pyrolysis	Electrolysis
Source	Methane or coal 	Methane or coal 	Methane 	Renewable electricity 

Figure 1.1: Brands of H₂ [2].

Special attention has been paid to the development of economical hydrogen production methods by chemically converting hydrocarbons or alcohols to a hydrogen-rich synthesis gas stream. This process generically called reforming, requires oxidizing agents. With steam as the oxidant and Methanol/methane as the hydrocarbon, the process is called Methanol/methane steam reforming (MSR), and hydrogen thus produced falls under the **Grey Hydrogen** category. It is effectively an endothermic reaction with a large heat effect; hence, multi-tubular packed bed reactors can be used for carrying out this reaction. Industrial multi-tubular packed bed reactors consist of a large number of parallel reactor tubes placed inside the heating or cooling jacket. Gaseous reactants flow through these tubes which contain a packed bed of catalyst particles. Either heat exchangers or furnaces can supply the heat transfer for performing the reaction. MSR is an endothermic reaction that takes place on the catalyst surface. The heat source is supplied to the reactor tubes by means of a fire burner as the operating temperature of the gaseous

fluid is in the order of 1000K. The three main reactions that are involved in this process with Methane as the hydrocarbon are



The reaction r_1 is the reforming reaction which is exothermic in nature and r_2 is the Gas water shift which is an exothermic reaction. The augmented reaction is represented in r_3 which indicates that the overall reaction is endothermic. At the outlet of the steam reformer the stream mixture called "Syn-gas" consists of H_2 , CO , CO_2 , and unreacted CH_4 . The concentration of H_2 and CO_2 at the reformer outlet increases with decreased reactant flow rate and increased inlet temperature.

Blue hydrogen can be produced by appending the above MSR process with the carbon capture and storage system (CCS). Retrofitting with CCS would allow the existing systems to continue producing hydrogen while achieving reduced Green House Gas (GHG) emissions. This is an option is to produce hydrogen with lower GHG emissions while reducing pressure on the renewable energy capacity installation rate to produce green hydrogen. Notably, industrial processes like steel production may require a continuous flow of hydrogen; blue hydrogen could be an initial solution while green hydrogen ramps up production and storage capacity to meet the continuous flow requirement. Besides this, blue hydrogen also faces social acceptance issues, as it is associated with additional costs for CO_2 transport and storage. The efficiency of CCS systems is expected to reach 85-95% [3] at best which means that 5-15% of CO_2 will still be emitted.

Among the different shades of hydrogen, **Green Hydrogen**, which is produced from renewable sources of energy is most suitable for the fully sustainable energy transition to net-zero. The well-established technology option for this purpose is water electrolysis fueled by electricity from renewable sources. There exist other methods for green hydrogen production such as biomass gasification and pyrolysis, thermochemical water splitting, photo-catalysis, supercritical water gasification of biomass, combined dark fermentation, and anaerobic digestion. However, except for MSR and water electrolysis, other processes are not mature technologies at commercial scales to be accepted by industries [2]. Green hydrogen production through electrolysis is consistent with the net-zero route, allowing the exploitation of synergies from sector coupling, thus decreasing technology costs and providing flexibility to the power system.

Though water electrolysis technology has existed for a couple of centuries, it account for only 5% of the world's hydrogen production due to the high cost relative to producing hydrogen from reforming [2]. However, these stats are changing due to the increased devotion toward sustainable energy production. Dynamic coupling of the renewable energy to the electrolysis technology yields GHG-free hydrogen production while providing a solution to the intermittency problem associated with renewable energy sources. The hydrogen can be synthesized into ammonia to be used as a fuel for internal combustion engines in maritime industries. Hydrogen can also be used as fuel in combustion and fuel cells with applications in transport, heating, power generation, and industries. The life of green hydrogen is shown in Figure 1.2), below

1.1 Water electrolysis

Water electrolysis is dictated by the science of electrochemistry which studies the phenomena that occurs when electrical energy induces chemical reactions to occur. On a microscopic resolution, electrochemistry studies the reactions in which the ions cross the interface between the solid electrode and the electrolyte. Alkaline water electrolysis (AWE), solid oxide electrolyzer cell (SOEC), and Polymer electrolyte membrane (PEM) water electrolysis are the three main electrolysis technologies applied to water electrolysis. The operating principle and methods of these electrolysis methods are illustrated in Figure (1.3).

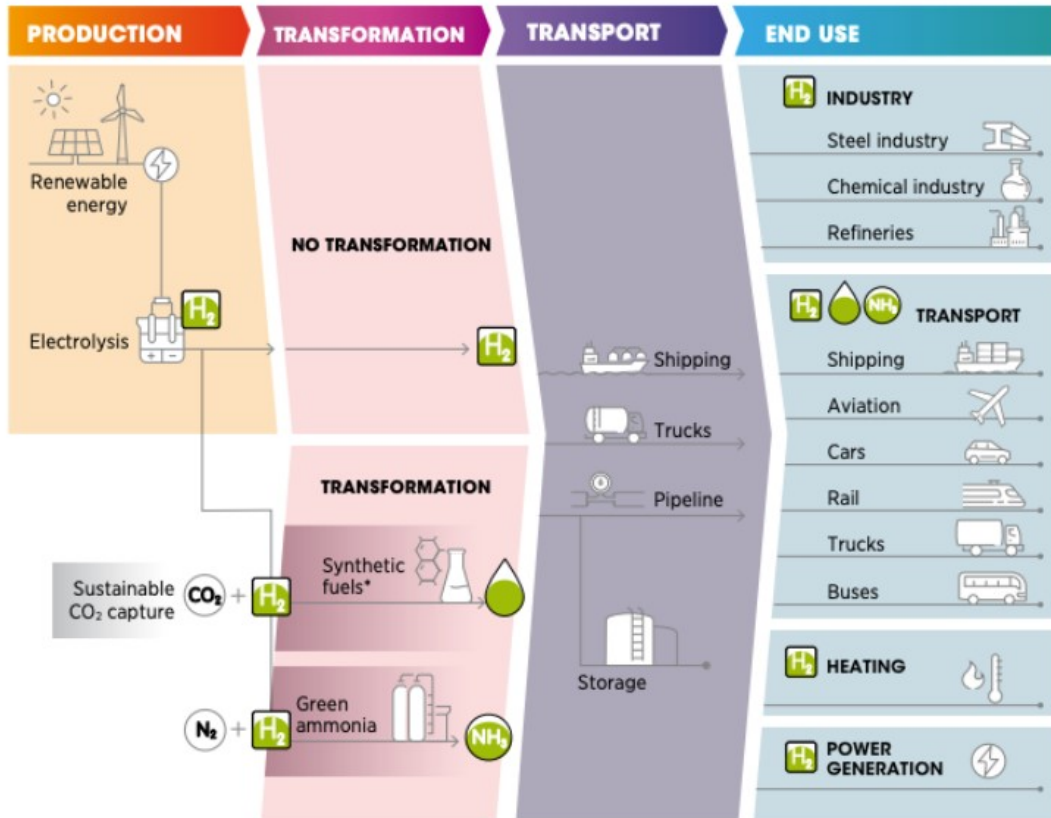


Figure 1.2: Green H₂ Production, conversion and end-use [2].

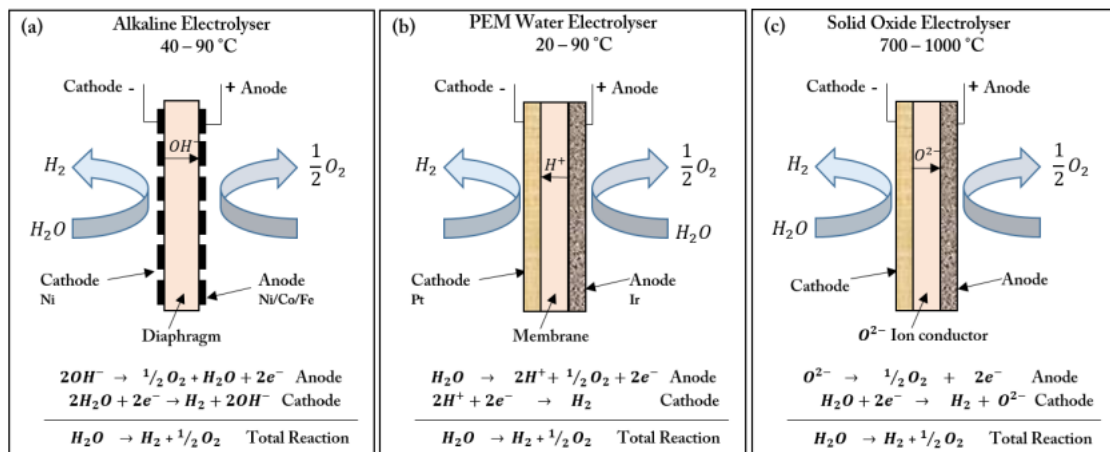


Figure 1.3: operating principle of (a) AWE (b) PEM (c) SOEC [4].

1.1.1 Solid oxide electrolyzer cell (SOEC)

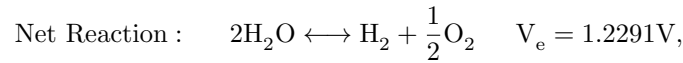
The SOEC that operates at high temperature commonly uses zirconia (ZrO₂) doped with yttrium (III) oxide (Y₂O₃) due to high oxygen ion conductivity and also maintains the chemical and thermal stability at such high temperature [5]. The high operating temperature favorably reduces the electricity demand, overpotentials, and power losses. Since the electric energy cost covers 30% of the total electrolytic hydrogen cost, this technology is relatively cost-effective [4]. The main drawback of this technology is material degradation and limited long-term stability which are the consequences of the high operating temperature.

1.1.2 Polymer electrolyte membrane (PEM) water electrolysis

In PEM, a thin solid proton-conducting membrane is used as the electrolyte instead of an electrolytic solution. The thin membranes reduce the ohmic losses and the produced hydrogen is relatively pure due to the low gas crossover property of the membrane. Further, the PEM has a broad operating power band due to the high proton conductivity through the membrane which is an essential aspect when electrolyzers operate at fluctuating conditions such as the renewable sources [6]. The polymer membrane not only serves as the ionically conductive medium but also provides structural support for the electrodes. The electrodes used here are noble metals/metal oxides like Platinum which are expensive.

1.1.3 Alkaline water electrolysis (AWE)

Water is a poor ionic conductor and needs a conductive electrolyte to achieve a considerable hydrogen production rate. Thus an acidic or alkaline aqueous solution is used as the electrolyte to enhance ionic conductivity. Among those, an alkaline solution is preferred to avoid the corrosion of the electrodes [7]. The electrolytic reaction is given by,

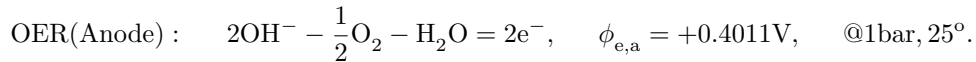
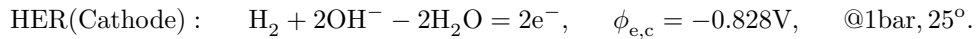


where V_e indicates the thermodynamic equilibrium cell potential. This net reaction can be decomposed into anodic and cathodic half-cell reactions. oxygen gas is generated at the anode-electrolyte interface and hence the anodic half-cell reaction is also known as the oxygen evolution reaction (OER). The cathodic half-cell reaction is also known as the hydrogen evolution reaction (HER) because the hydrogen gas is produced at the cathode-electrolyte interface.

Expressing the half cell reactions in the electrochemically conventional form of eq. (1.1) gives,

$$\sum_i S_i M_i^{z_i} = ne^-, \quad (1.1)$$

where S_i and M_i are the stoichiometric coefficients and symbol of the chemical formula of species i , and z_i is the charge number of species i .



where $\phi_{e,c}$ and $\phi_{e,a}$ are the equilibrium potential of the cathode and anode half-cell reactions.

Typical AWE uses aqueous KOH solution (20-30 wt.%). The electrodes (nickel-based) are porous to enable more interfacial surface area in turn increasing the reaction sites. The operating voltage is typically between $V=1.7-1.9$ V and the current density is 1 kA/m^2 with the production rate of $0.211 \text{ m}^3/\text{s}$ [4].

The use of non-noble metal electrodes and the system's long-term stability make AWE a commercially preferable solution over the other existing electrolyzer technologies. The operating power band of the AWE is narrow compared to that of the PEM, thus AWE is ineffective under dynamic conditions. Thus further advancements to reduce costs and increase efficiency are required to enable the widespread use of AWEs.

Problems with AWE

Though AWE is a mature technology with low specific cost there exist several disadvantages that require focus. Due to its narrow operating power band, the fluctuation in the power supply from renewable resources can result in explosive mixtures, corrosion of materials, temperature and pressure drop, etc. [8]. The low current density limit of AWE has an undesirable effect on the cost of hydrogen production. The cost per kg of hydrogen and electricity increases as the current density increases. But, the hydrogen cost is more sensitive for low current densities which is the case for AWE. This is clearly inferred from the plot in Figure (1.4) below.

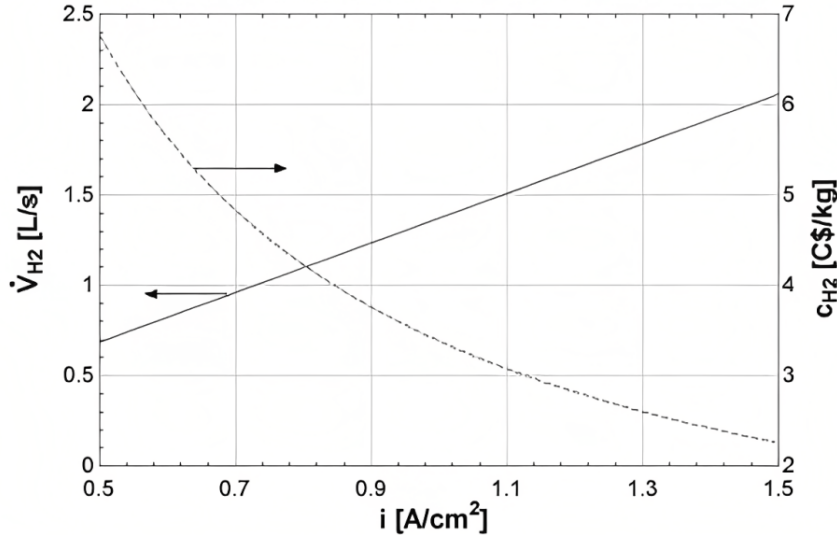


Figure 1.4: Effect of current density on the hydrogen production rate (\dot{V}_{H_2}) and the cost (C_{H_2}) [9].

The evolution of hydrogen and oxygen bubbles is one of the reasons for the low efficiency and low ionic conductivity. The bubble evolution is discretized into 3 stages namely nucleation, growth, and detachment [10]. They create both electrochemical resistance and mass transfer barrier to electrode reactions [11, 12]. The nucleating, growing bubbles block the electrode surface, reducing the active reaction sites and subsequently affecting the production. Few research activities study the electrolytic bubble phenomena with the aim of improving the efficiency of AWE [13]. The effect of gas bubbles under the influence of ultrasonic field [14], magnetic field [15], intensified gravity field [16], micro-gravity environment [17, 18] are studied to improve the bubble removal rate.

1.2 Thesis scope

To address the aforementioned issues a strong understanding of the electrochemical phenomena, underlying multi-physical interactions, and operational conditions are essential to optimize the electrochemical systems. The complex micro-structures and multi-physics of electrochemical devices can be well captured using computational modeling due to its ability to resolve the detailed physics which is difficult to be observed in the experimental study. Besides, computational tools are faster and more cost-effective and expedite the transition to net zero. Most of the critical physics that happens in the electrochemical systems occur within the porous media and at the electrode-electrolyte interface [19]. Further, bubble nucleation is known to usually occur at the cracks, and crevices on the electrode surface which result in the formation of a gas molecule cluster from solution supersaturated with gas molecules [10]. These phenomena are characterized as mesoscale phenomena with length scales ranging between microns and millimeters. The majority of the electrochemical reactions and transport phenomena occur around the electrode-electrolyte interface, which makes the mesoscale phenomena critical for the design and innovation in electrochemical systems [19]. Thus an efficient and high-fidelity numerical simulation tool is essential for both fundamental research and industrial research and development.

Conventional computational fluid dynamics (CFD) models are not suitable for modeling the mesoscale effects such as the heterogeneous reactions that occur at the pore scales with a large number of species involved in the transport (multi-component systems). The several modeling approaches suitable for this are illustrated in Figure 1.5. Among these molecular dynamics (MD) is the most fundamental yet expensive. There are several mesoscale models that can be used to resolve the chemical-physical processes that occur in electrochemical systems. One such method is the lattice Boltzmann method (LBM) which has shown fast development in recent years. Several works of literature indicate that LBM is a suitable tool for studying electrochemical phenomena because of its ability to model multi-component, multi-phase physics. Moreover, because of the kinetic nature of LBM, the electrode kinetics can be modeled at microscopic or mesoscopic scales [20].

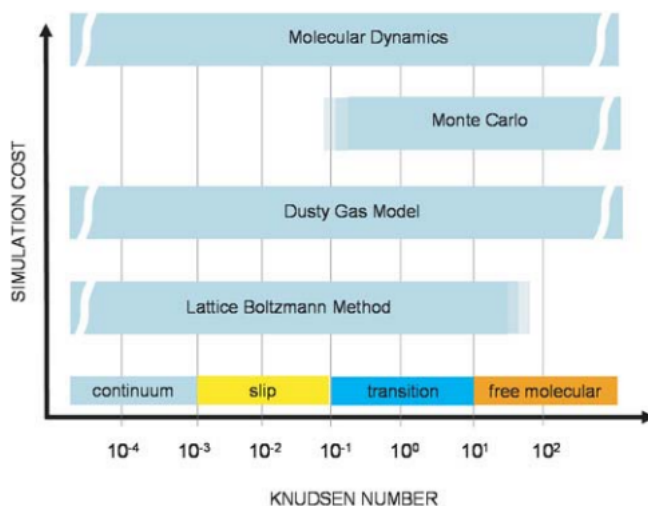


Figure 1.5: Modeling approach based on the required resolution of physics [21].

1.2.1 Thesis vision

Modeling the electrochemical reaction and the mass transfer of the ion/neutral species are essential to understand the bubble nucleation process. Resolving the double layer and understanding the evolution behavior of the physical parameters using the mesoscale modelling approach will be the agenda of this thesis. The mass transport phenomena based on the dilute solution theory will be modeled using the LBM for AWE. To model the heterogeneous HER occurring at the cathode surface of the hydrogen half-cell, the Butler-Volmer kinetics equation will be used. The list of thesis objectives that will be executed in this work are listed below.

- The methodology to solve the migration-diffusion problem with heterogeneous reaction using the LBM will be formulated. The Poisson-Nernst-Planck model coupled with the Butler-Volmer kinetics model is chosen for this purpose.
- With the appropriate geometric and dynamic similitude analysis and properly modeling the boundary condition from physical space to the lattice space, the Lattice Boltzmann simulation will be performed using a code built in MATLAB.
- To validate the methodology, the system adhering to the Debye-Hückel theory will be solved and compared to the analytical expressions for species concentration and electric potential.
- The evolution of the physical parameters in the hydrogen-half cell will be studied by resolving the physics in the electric double layer. The effect of reaction rate on the species distribution will be studied by comparing the results for different electrode surface potential.
- Further some complex simulations will be performed to check the robustness of the code. The effect of fluxes in the primary and secondary directions on the species' transportation will be studied by implementing a spatially varying boundary condition. Finally, the methodology is extended to solve the migration-diffusion problem with heterogeneous reactions occurring on the surface of a deformed boundary.

1.2.2 Structure of the report

After providing a general introduction and gradually getting into the purpose and vision of the project in **chapter 1**, the fundamental knowledge regarding the electrochemistry relevant to this project is discussed in **chapter 2**. The governing equations for the transport model, electric potential, and reaction kinetics are discussed.

In **Chapter 3** fundamentals of the LBM and the lattice configurations are explained. The model for collision operator and the general boundary conditions used in this study are explained. **Chapter 4**,

the methodology to solve diffusion problems using LBM is explained and extended to solve one and two-dimensional problems. The results from LBM simulations are compared with those from FDM simulations.

The methodology to solve the migration-diffusion problem along with the coupling of the heterogeneous HER reaction is explained in **chapter 5**. The steady-state Poisson's equation for electric potential can be solved using the 'FDM in lattice space' or pseudo-transient LBM. Both these methodologies are elaborated in this chapter. Then, the LBM approach to solving the Nernst-Planck model for species concentration is explained. Further, the coupling of the Poisson, Nernst-Planck, and reaction kinetics solver and the exchange data structure and the solver algorithm is explained.

Chapter 6 explains the Debye-Hückel theory and uses it as a benchmark case to validate the developed methodology. The grid independence study based on the double-layer resolution is studied. The steady-state results from LBM are compared to those based on the Debye-Hückel theory.

The transport phenomena and the evolution behavior of potential and species concentration in hydrogen half-cell for a constant reacting flux at the cathode is dealt with in **chapter 7**. The simulation technique for high cathode potential is explained and then the issues from the classical Poisson-Nernst-Planck model which neglects the steric effects are addressed.

Chapter 8 deals with the transport phenomena and evolution behavior of electric potential and species concentration in the hydrogen half-cell with the reaction kinetics dictated by the Butler-Volmer equation. A complex simulation with spatially varying boundary conditions is performed to understand the influence of the secondary fluxes on the potential and species concentration distributions. The methodology to simulate the species behavior around the catalyst particle of the electrode and the simulation case is discussed in **Chapter 9**.

Chapter 10 concludes the work where the accomplished work is briefly explained. Then, further work to perfect the model to enhance its robustness and performance are briefly discussed.

Chapter 2

Electrochemistry

On a microscopic scale, the science of electrochemistry studies the reaction in which the ions cross the electrode-electrolyte interface. These reactions are influenced by the potential difference between the electrode and the electrolytic solution which are thermodynamically and kinetically controlled. Thus the mass transport phenomena, thermodynamics, and reaction kinetics are interrelated, and an extensive study of these verticals is essential to build a reliable and robust multi-component simulation model.

2.1 Thermodynamics and potential

The most useful thermodynamic function for the evaluation of electrochemical systems, as well as most other reactions, is free energy. Free energy provides a criterion for predicting the direction of chemical or electrochemical reactions and the composition of the system at equilibrium. A thermodynamic property of the species called the electrochemical potential μ_i is related to the Gibbs free energy as,

$$\Delta G = \left(\sum_i s_i \mu_i \right)_{\text{anode}} - \left(\sum_i s_i \mu_i \right)_{\text{cathode}} . \quad (2.1)$$

The Gibbs free energy is related to the equilibrium or open-circuit potential V_e (the potential at which no current flows) by,

$$\Delta G = nFV_e, \quad (2.2)$$

where n denotes the stoichiometric coefficient or number of moles of transferred electrons, F is the Faraday's constant given by $F = 96.4853 \text{ kCmol}^{-1}$.

For AWE, free energy for the anode, cathode, and the total cell at 1 bar and 25°C is by,

$$\Delta G_{\text{anode}} = 77.4 \text{ kJ/mol}, \quad \Delta G_{\text{cathode}} = -159.8 \text{ kJ/mol}, \quad \Delta G_{\text{cell}} = 237.2 \text{ kJ/mol}. \quad (2.3)$$

Thus, $\Delta G_{\text{cell}} = 237.2 \text{ kJ/mol}$ is the minimum amount of energy required to produce the hydrogen. At this threshold potential V_o , the electrode reaction is inherently slower and then an over-potential (η) which is above the equilibrium cell potential is essential. The over-potential enables to start off the reaction due to the activation energy barrier, increasing the reaction rate [22]. In an electrochemical system, there are electrical, electrochemical, and transport-related barriers; hence, a sufficient electrical energy supply is needed to overcome these resistances. The transport-related resistances which are due to the gas bubbles in the solution, electrolyte itself, ion transfer in the electrolyte, and membrane separator lead to loss of energy known as the ohmic losses [13]. Thus the over-potential is essential for the system to overcome the above-mentioned barriers.

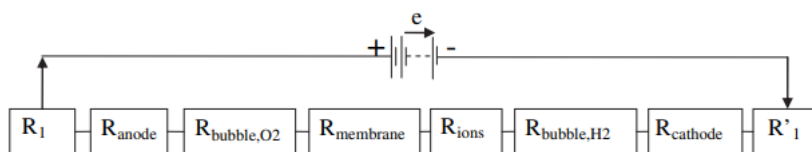


Figure 2.1: AWE resistance analogous to electrical resistance[13].

Fig. (2.1) illustrates the resistances in AWE analogous to the electrical system. R_1 and R'_1 are the resistances from the wiring of cables.

2.2 Ion transport mechanisms

There are three transfer mechanisms that are responsible for the movement of the ions in the electrolytic solution. They are migration, diffusion, and convection. Migration is the transport of ionic species due to an electric potential gradient. Diffusion is the transfer of ions/neutral species due to a concentration gradient. Convection is the transfer of ions/neutral species due to the bulk flow of the electrolyte. Pertaining to this project, the influence of the convection mechanism is very low compared to the other two and hence it is neglected.

2.2.1 Migration

The gradient in electric potential which induces an electric field creates a driving force for moving the ions. The electric field drives the cations toward the cathode (along the electric field direction) and the anions toward the anode (against the electric field direction). The velocity of the ions in response to the electric field is given by

$$\mathbf{u}_{i,\text{migration}} = -z_i \nu_i F \nabla \phi, \quad (2.4)$$

where ν_i (mol s/kg) is the ionic mobility (the factor that describes the sensitivity of an ion in an electric field) of ionic species i . The Nernst-Einstein equation that relates the diffusion coefficient (D_i) and the ionic mobility of a species is given by

$$D_i = RT \nu_i, \quad (2.5)$$

where R and T denotes the universal gas constant and system temperature respectively. Generally, the flux density is defined as the product of the species' velocity and the concentration density, given by eq. (2.6).

$$\mathbf{N}_i = C_i \mathbf{u}_i. \quad (2.6)$$

Thus, the flux density of the ions due to migration is given by eq. (2.7),

$$\mathbf{N}_{i,\text{migration}} = \frac{-z_i D_i C_i F \nabla \phi}{RT}. \quad (2.7)$$

2.2.2 Diffusion

The driving force for the motion of ion/neutral species by diffusion is the concentration gradient of the species (Fick's equation for dilute solution). The corresponding flux density is given by

$$\mathbf{N}_{i,\text{diffusion}} = -D_i \nabla C_i, \quad (2.8)$$

where D_i is the diffusion coefficient of species i .

2.2.3 Convection

The species velocity due to convection is the same as the bulk velocity (\mathbf{u}_b) of the electrolytic solution. Thus, the flux density of the species due to convection is given by eq. (2.9),

$$\mathbf{N}_{i,\text{convection}} = C_i \mathbf{u}_b. \quad (2.9)$$

Convection can be split into driving forces due to natural convection and forced convection. In an electrically neutral solution, the bulk flow-induced convection of species doesn't contribute to the net current density. Yet it could have an indirect influence on the net current because the bulk convection can alter the local concentration of the species in turn creating a concentration gradient to drive diffusive species transport [23].

The total flux density of a species is derived by summing eq. (2.7), (2.8) and (2.9),

$$\mathbf{N}_i = \frac{-z_i D_i C_i F \nabla \phi}{RT} - D_i \nabla C_i + C_i \mathbf{u}_b \quad (2.10)$$

Eqn (2.10) is referred to as the Nernst-Planck equation which will be used to model the flux density in the material balance equation. It is explained in detail in section (2.4).

2.3 Electrode kinetics, reaction rate

The rate of the electrode reaction, characterized by the current density, depends on the nature and previous treatment of the electrode surface [13, 23]. The reaction rate also depends on the composition of the electrolyte adjacent to the electrode, just outside the electric double layer. The composition of the electrolyte adjacent to the electrode is different from that at the bulk of the solution because of the limited mass transfer rate discussed in section (2.4). The theory of the double layer is a microscopic phenomenon rather than a macroscopic one. The effect of double layer on electrode kinetics is dealt with in section (2.3.2). The electrode potential characterized by the over-potential (η) also governs the rate of the reaction. For a general electrode reaction expressed in the form of eq. (1.1), the surface over-potential (η_s) expresses the deviation from the equilibrium potential given by

$$F\eta_i = F(\Phi_{\text{electrode}} - \Phi_{\text{solution}}) = -\mu_e + \sum_i \frac{s_i}{n} \mu_i. \quad (2.11)$$

2.3.1 Butler-Volmer equation

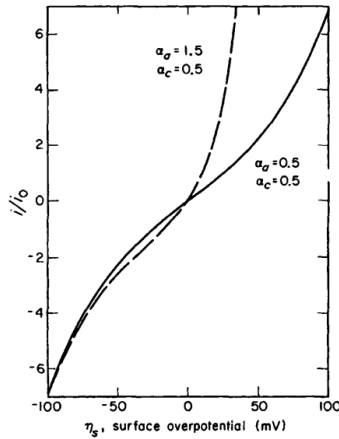
The current density is a function of the surface over-potential, the concentration of the solution adjacent to the electrode surface, i.e.,

$$j = f(\eta, C_i). \quad (2.12)$$

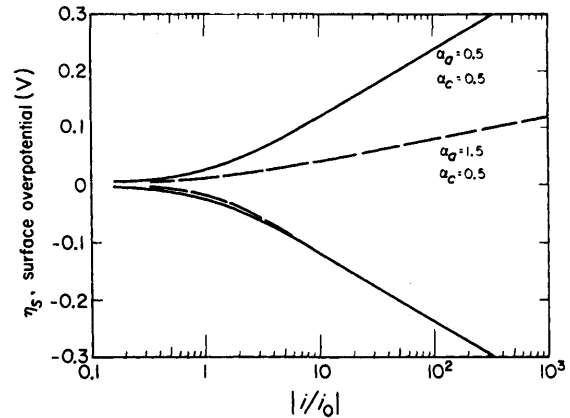
In general, the current density is used to quantify the rate of the reaction occurring at the electrode surface. The Butler-Volmer model for the current density is given by

$$j_n = j_o \left[\exp\left(\frac{\alpha_a F \eta}{RT}\right) - \exp\left(\frac{-\alpha_c F \eta}{RT}\right) \right], \quad (2.13)$$

where j_o is the exchange current density, α_a , and α_c are the apparent transfer coefficient ($\alpha_a, \alpha_c \in (0.2, 2)$), that relates how an applied potential favors one direction of reaction over the other [23].



(a) Butler-Volmer plot at 25°C.



(b) Tafel plot at 25°C.

Figure 2.2: Plot relating the current density and surface over-potential at 25°C [23].

case I: for large η (Tafel approximation)

In 1905, Tafel made an observation that at large values of η one of the terms from eq. (2.13) can be neglected [24] and the overall reaction rate is given by

$$J_n = j_o \exp\left(\frac{\alpha_a F \eta}{RT}\right), \quad \alpha_a F \eta \gg RT, \quad (2.14)$$

$$j_n = -j_o \exp\left(\frac{\alpha_c F \eta}{RT}\right), \quad \alpha_c F \eta \gg RT. \quad (2.15)$$

case II: for small η (linearization)

From Fig. (2.2a), for the low value of η , the current density looks to be linear. By expanding the exponential terms in eq. (2.13) with a Taylor series and neglecting the higher-order terms gives,

$$j_n = j_o \frac{(\alpha_a + \alpha_c) F \eta}{RT}, \quad \eta \ll RT. \quad (2.16)$$

The Butler-Volmer equation implicitly indicates that the exchange current density depends on the concentration of the reactants and products [25]. So, Bernardi and Verbrugge made a correction to express this concentration dependence explicitly [25, 26, 27, 28], given by

$$j_n = j_{o,m} \left(\frac{C_{s,m}}{C_{r,m}}\right)^{\gamma_m} \left[\exp\left(\frac{\alpha_a F \eta}{RT}\right) - \exp\left(\frac{-\alpha_c F \eta}{RT}\right) \right], \quad (2.17)$$

where index m denotes either the anode or cathode side. $j_{o,m}$ is the corresponding exchange current density at reference concentration, $C_{r,m}$ is the reference concentration of the reactant, $C_{s,m}$ is the actual reactant concentration at the electrode-electrolyte interface.

Electrode kinetics for AWE

Extending the above-mentioned kinetics concept to the AWE reaction, the current density for the anode side (OER) and cathode side (HER) are derived in [27], given by eq. (2.18), (2.20) below.

For HER on the cathode side:

$$j_n = j_{o,c}^{\text{ref}} \left[\left(\frac{C_{\text{OH}^-}}{C_{\text{OH}^-}^{\text{ref}}}\right)^2 \left(\frac{C_{\text{H}_2}}{C_{\text{H}_2}^{\text{ref}}}\right) \exp\left(\frac{\alpha_i F \eta_i}{RT}\right) - \left(\frac{C_{\text{H}_2\text{O}}}{C_{\text{H}_2\text{O}}^{\text{ref}}}\right)^2 \exp\left(\frac{-\alpha_c F \eta_c}{RT}\right) \right]. \quad (2.18)$$

The over-potential for the HER which is the cathodic half-cell reaction (η_c) is given by

$$\eta_c = \phi_s - \left(\phi_{o,c} + \frac{2.303RT}{nF} (14 + \log_{10}([\text{OH}^-]^2)) \right), \quad (2.19)$$

where $\phi_{o,c}$ denotes the equilibrium potential at 1 bar and 298.13 K under neutral pH. The Nernst equation for electrolytic potential is used to correct the equilibrium potential based on the pH and temperature of the system. The logarithmic term in the above equation denotes the pOH of the electrolytic solution and $[\text{OH}^-]$ denotes the concentration mol/L).

For OER on the anode side:

$$j_n = j_{o,a}^{\text{ref}} \left[\left(\frac{C_{\text{OH}^-}}{C_{\text{OH}^-}^{\text{ref}}}\right)^2 \exp\left(\frac{\alpha_a F \eta_a}{RT}\right) - \left(\frac{C_{\text{O}_2}}{C_{\text{O}_2}^{\text{ref}}}\right)^{1/2} \left(\frac{C_{\text{H}_2\text{O}}}{C_{\text{H}_2\text{O}}^{\text{ref}}}\right) \exp\left(\frac{-\alpha_c F \eta_a}{RT}\right) \right]. \quad (2.20)$$

The description of the variables and corresponding values for AWE is given in the Table (2.1) below extracted from [27, 29, 30, 31, 32].

Symbol	Description	Value	Unit
a_c/a_a	Active surface area to volume of electrode	$4.6 \times 10^4 / 3.7 \times 10^4$	m^{-1}
$I_{o,c}^{\text{ref}}$	Ref. exchange current density at cathode	4.3	Am^{-2}
$I_{o,a}^{\text{ref}}$	Ref. exchange current density at anode	3.7	Am^{-2}
α_a / α_c	Transfer coefficient for HER	1.534 / 0.466	-
α_a / α_c	Transfer coefficient for OER	0.818 / 1.182	-
$C_{\text{H}_2\text{O}}^{\text{ref}}$	Ref. H ₂ O concentration	42710	mol m^{-3}
$C_{\text{OH}^-}^{\text{ref}}$	Ref. OH ⁻ concentration	6851.19	mol m^{-3}
$C_{\text{H}_2}^{\text{ref}}$	Ref. H ₂ concentration	10	mol m^{-3}
$C_{\text{O}_2}^{\text{ref}}$	Ref. O ₂ concentration	10	mol m^{-3}

Table 2.1: Kinetics Properties for AWE.

2.3.2 Effect of double layer on kinetics

Structure of double layer

The electrolytic reaction is fundamentally a heterogeneous reaction, which means that the reaction takes place at the boundary (electrode-electrolyte interface). The EDL, which arises due to charge separation at the electrode-electrolyte interface is localized over a molecular dimension [33, 34].

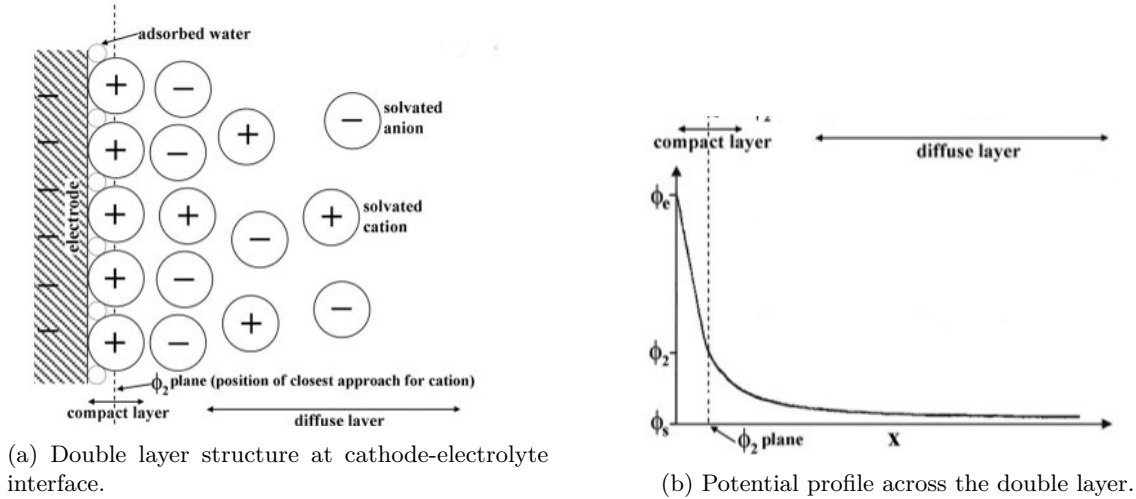


Figure 2.3: electric double layer (EDL) near cathode [33].

The compact layer in Fig. (2.3) encompasses multiple layers, separated by conceptual planes. The inner Helmholtz plane (IHP) is the plane that passes through the center of the ions/molecules adsorbed to the electrolyte. The outer Helmholtz plane (OHP) passes through the center of the ions that are at the closest approachable distance from the electrode surface. The electric potential in this compact layer is a linear function with respect to the normal direction of the surface. The diffuse layer is next to the compact layer and exhibits an exponential potential profile [33]. The thickness of the diffuse part of the double layer is generally in the order of nano-meters ($\mathcal{O}(10^{-9})$) [23] and is given by the Debye length in eq. (2.21).

$$\lambda = \sqrt{\frac{\epsilon_o \epsilon_r k_B T}{q^2 \sum_i z_i^2 C_{i,\infty} N_A}}, \quad (2.21)$$

where ϵ_r is the relative permittivity of the electrolyte and $\epsilon_r = 80$ for aqueous electrolytes. $\epsilon_o = 8.85 \times 10^{-12}$ F/m is the permittivity of vacuum. $k_B = 1.38 \times 10^{-23}$ J/K is the Boltzmann constant and $q = 1.6 \times 10^{-19}$ C is the charge of the electron. $C_{i,\infty}$ (mol/m³) is the concentration of ion i at the bulk region, and Avogadro number $N_A = 6.023 \times 10^{23}$ is used to represent ion concentration in the number of ions per cubic meter. For example, with the concentration of ions given in the Table (2.1), the Debye length was calculated to be 0.1178 nm. The ionic concentrations in Table (2.1) are very high which yields a lower Debye length (λ) which is smaller compared to the molecular size of water.

The existence of a double layer significantly affects the difference in potential between the electrode and the electrolyte due to the adsorption of the species to the electrode surface. The exponential decay of the potential over the molecular distance range gives rise to an intense electric field (potential gradient). Such a high and localized driving force might lead to the activation of energetically difficult processes to be carried out electrochemically [33]. Since the EDL behaves like a capacitor, it imposes problems in kinetic studies, particularly at high surface area industrial applications due to the existence of charging current [23]. The current density j for an electrode of constant surface area, with the consideration of the EDL effects, is represented by eq. (2.22).

$$j = f(\eta, C_i) + C_{EDL} \frac{d\eta}{dt}, \quad (2.22)$$

Where C_{EDL} is the charge capacity of the double layer, the function $f(\eta, C_i)$ is the current for driving the reaction (example: Butler-Volmer equation). Thus, the EDL behaves like a capacitor in parallel with

the electrode reaction, so that the supplied current passing through the electrode to the solution can either drive the reaction at the interface or be used to charge the EDL capacitor. This effect is significant when an alternating current is used [23]. Thus, in order to model the effect of the diffuse layer of EDL, one should solve the flux equation (that will be discussed in the next section) of all ions in combination with the Poisson equation for electric potential [35].

2.4 Transport phenomena

Mass transfer in electrolytic solution demands a description of motions of ionic species, material balance, current flow, electro-neutrality, and fluid motion. The domain for the study consists of ionic, neutral components. The main challenge with modeling the transport phenomena is the lack of data for transport properties particularly for concentrated electrolytes [23]. Though the transport process involves migration, convection, and diffusion, this project deals with the transport phenomena as a diffusion-migration problem. The transport phenomena are split into two main verticals, namely the dilute electrolyte theory, and concentrated electrolyte theory, based on the concentration level of the electrolyte.

2.4.1 Dilute solution theory

In dilute solution theory, the species flux density will be governed by the Nernst-plank equation given by eq. (2.10). In AWE the reaction takes place only at the electrode-electrolyte interface (boundary) and not at the bulk of the electrolyte. Then the material balance equation to model heterogeneous reactions is given by,

$$\frac{\partial C_i}{\partial t} = -\nabla \cdot \mathbf{N}_i. \quad (2.23)$$

The boundary condition at the electrode-electrolyte interface for the reacting/produced species (sink/source) is given by

$$\mathbf{N}_i|_{\text{electrode-electrolyte}} = \frac{S_i j}{z_i F}, \quad \forall \text{ reacting/produced species}, \quad (2.24)$$

where S_i is the stoichiometric coefficient of the species, j is given by the Butler-Volmer equation. The boundary condition for the non-reacting species is a zero-flux BC given by

$$\mathbf{N}_i|_{\text{electrode-electrolyte}} = 0, \quad \forall \text{ non-reacting species}, \quad (2.25)$$

The local electroneutrality condition given by eq. (2.26) is not suitable under all local conditions, i.e., it is not valid at the double layer and at the boundaries [36]. Its validity holds only in the bulk of the electrolyte. Hence a generalized Poisson equation for electric potential [35] will be solved given by eq. (2.27).

$$\sum_i z_i C_i = 0. \quad (2.26)$$

$$\nabla^2 \Phi = -\frac{F}{\epsilon} \sum_i z_i C_i, \quad (2.27)$$

where ϵ is the permittivity of the electrolyte. The other approach to finding the electric potential can be inferred from the Nernst-Planck eq. (2.10) and is used in [20, 25, 27, 35] given by

$$\nabla \cdot (k \nabla \Phi) + F \nabla \cdot \sum_i z_i D_i \nabla C_i = \nabla \cdot \mathbf{i}, \quad (2.28)$$

where \mathbf{i} denotes the ionic current density, k is the ionic conductivity. If local electroneutrality is assumed then $\nabla \cdot \mathbf{i} = 0$, and if local electroneutrality is not valid then $\nabla \cdot \mathbf{i} = j$, which is at the electrode-electrolyte boundary. Adhering to this approach, [32] has formulated the elliptic Poisson solver considering non-electroneutrality given by

$$\nabla \cdot \left(\frac{z_{\text{OH}^-}^2 F^2 D_{\text{OH}^-} C_{\text{OH}^-} \nabla \Phi}{RT} \right) + \nabla \cdot (z_{\text{OH}^-} F D_{\text{OH}^-} \nabla C_{\text{OH}^-}) + j = 0. \quad (2.29)$$

It is recommended to correct the diffusive coefficients to consider the porous medium using the Bruggeman correlation [27]. For the Poisson potential equation given by eq. (2.27) or eq. (2.28), the boundary

condition at the electrode-electrolyte interface is given by a Neumann type BC [20] denoted by eq. (2.30).

$$-k \frac{\partial \Phi}{\partial y} \Big|_{\text{electrode-electrolyte}} = j, \quad (2.30)$$

where y is the coordinate direction normal to the electrode-electrolyte interface. The current density j is derived from the Butler-Volmer equation for the electrode (cathode or anode).

The transport properties in an infinitely dilute electrolyte are mobilities u_i and self-diffusive coefficients D_i , which means that the concentration distribution of other species does not influence the diffusion of species i . The transport properties for AWE species are given in Table (2.2) below [27, 37, 38, 39].

Symbol	Description	Value	Unit
$D_{\text{H}_2\text{O}}$	Diffusivity of water	2.2952×10^{-9}	m^2s^{-1}
D_{OH^-}	Diffusivity of hydroxide ion	5.27×10^{-9}	m^2s^{-1}
D_{O_2}	Diffusivity of oxygen	3.6×10^{-9}	m^2s^{-1}
D_{H_2}	Diffusivity of hydrogen	10×10^{-9}	m^2s^{-1}
u_{OH^-}	Mobility of hydroxide ion	2.05×10^{-3}	m^{-1}
u_{k^+}	Mobility of potassium ion	7.619×10^{-4}	m^{-1}

Table 2.2: AWE transport properties for Dilute electrolyte theory @ 80°C.

Chapter 3

Lattice Boltzmann method

Electrochemical systems are inherently multi-physics systems, their performance is driven by numerous physical phenomena occurring at the interface characterized by mesoscopic scales and also involves the coupling of different physics. These phenomena include the transport of ion/neutral species and electrochemical reactions. Hence, computation models need to accurately capture these physics and predict the performance and operation of the electrochemical system. There are two broad categories of computational techniques that could be used to simulate the electrochemical phenomena namely the particle-based simulation or mesh-based computational fluid dynamics. There are various particle-based simulation techniques such as dissipative particle dynamics (DPD), smoothed particle hydrodynamics (SPH), discrete element methods (DEM), lattice Boltzmann method (LBM) [19]. Among them, the DPD, SPH, and DEM are off-lattice methods and their domain is represented by the Lagrangian particles. But LBM represents the domain as a collection of pseudo-particles, which interact via propagation/streaming and collision on a discrete lattice domain structure. Since LBM is inherently a scale-bridging numerical scheme, which incorporates simplified kinetic models to capture the microscopic behavior, it is used as the simulation tool for this project.

3.1 Lattice-Boltzmann equation

In LBM the statistical description of the system is given by the distribution functions $f(r, e, t)$ giving the number of molecules at time t positioned between r and $r + dr$ that have velocities between e and $e + de$. The evolution of the distribution function due to the application of the external force is given by,

$$\frac{df}{dt} = \Omega(f), \quad (3.1)$$

Where Ω is the collision operator. The collision operator can be determined using the BGK approximation given by eqn (3.2),

$$\Omega = w(f^{eq} - f) = \frac{1}{\tau}(f^{eq} - f). \quad (3.2)$$

Where w is known as the collision frequency and τ is the relaxation factor. The local equilibrium distribution function (f^{eq}) is determined from the Maxwell distribution function. Expressing eqn (3.1) in the partial differential equation form gives,

$$\frac{\partial f}{\partial t} + \mathbf{e} \cdot \nabla f = \frac{1}{\tau}(f^{eq} - f). \quad (3.3)$$

The above equation can be discretized in space and time and then split into collision and streaming steps.

The collision step is given by

$$f^*(\mathbf{x}, t) = f(\mathbf{x}, t)[1 - \Delta t/\tau] + \Delta t/\tau f^{eq}(\mathbf{x}, t), \quad (3.4)$$

where f^* denotes the post-collision distribution function. Then the streaming step is given by eqn (3.5),

$$f(\mathbf{x} + \mathbf{e}\Delta t, t + \Delta t) = f^*(\mathbf{x}, t). \quad (3.5)$$

Equilibrium distribution function

The procedure for solving different physics equations is the same. The difference is mainly in the equilibrium distribution function and the collision operator. For the particles moving in a medium with the macroscopic velocity \mathbf{u} , the equilibrium distribution function can be determined from the Maxwell distribution function given by eqn (3.6),

$$f^{\text{eq}} = \frac{\rho}{(2\pi RT)^{D/2}} \exp\left(-\frac{(\mathbf{e} - \mathbf{u})^2}{2RT}\right). \quad (3.6)$$

On expanding the exponential term and truncating the higher order terms give eqn (3.7),

$$f^{\text{eq}} = \rho\omega \left[1 + \frac{2\mathbf{e}\cdot\mathbf{u} - \mathbf{u}\cdot\mathbf{u}}{2e_s^2} + \frac{(\mathbf{e}\cdot\mathbf{u})^2}{2e_s^4}\right]. \quad (3.7)$$

$$f^{\text{eq}} = \rho\omega, \quad \forall \text{ stationary medium, i.e., } \mathbf{u} = 0, \quad (3.8)$$

where ω is the weigh factor for the distribution function, \mathbf{u} is the macroscopic velocity or the bulk velocity. e_s denotes the pseudo sound speed which depends on the lattice configuration.

3.2 Lattice configurations

In general, the lattice configuration is given by DnQm where n denotes the dimension of the problem and m denotes the number of streaming functions/directions per lattice.

3.2.1 One dimensional lattice

The general lattice configurations for the 1-D problem are D1Q2, D1Q3, and D1Q5, and the lattice structure is given in Fig. (3.1). Each node has a distinct distribution function and velocity vectors. For example, in D1Q3, the velocity vectors are e_0 , e_1 and e_2 and the distribution functions are f_0 , f_1 and f_2 . In the LBM domain, it is advisable to discretize the spatial and temporal domain with equal stepping values, i.e., $\Delta x = \Delta t$. Both in D1Q3 and D1Q5, the central node (0th) is static with zero velocity and hence their distribution function can't be involved in the streaming process.

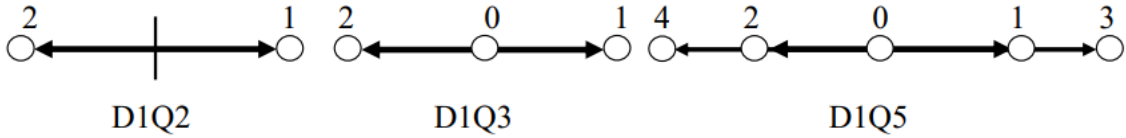


Figure 3.1: Lattice configurations for 1-D lattice[40].

The velocity vector and weight distribution are given in the matrix form below.

$$\text{For D1Q2: } [\mathbf{e}] = \begin{bmatrix} e_1 \\ e_2 \end{bmatrix} = \begin{bmatrix} 1 \\ -1 \end{bmatrix}, \quad [\omega] = \begin{bmatrix} \omega_1 \\ \omega_2 \end{bmatrix} = \begin{bmatrix} 1/2 \\ 1/2 \end{bmatrix}, \quad e_s^2 = 1/2 \quad (3.9)$$

$$\text{For D1Q3: } [\mathbf{e}] = \begin{bmatrix} e_0 \\ e_1 \\ e_2 \end{bmatrix} = \begin{bmatrix} 0 \\ 1 \\ -1 \end{bmatrix}, \quad [\omega] = \begin{bmatrix} \omega_0 \\ \omega_1 \\ \omega_2 \end{bmatrix} = \begin{bmatrix} 4/6 \\ 1/6 \\ 1/6 \end{bmatrix}, \quad e_s^2 = 1/3 \quad (3.10)$$

3.2.2 Two dimensional lattice

The general lattice configurations in case of a two-dimensional problem are D2Q4, D2Q5, and D2Q9, their respective configurations are shown in Fig. (3.2).

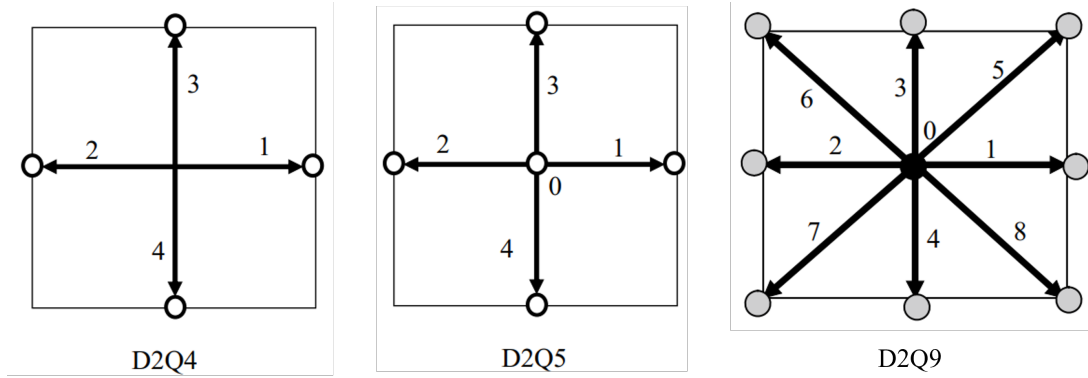


Figure 3.2: Lattice configurations for 2-D lattice[40].

The configurations D2Q5 and D2Q9 have a central static node and hence aren't involved in the streaming process. For simulating the system with the fluid flow the D2Q4 and D2Q5 configurations are not suitable [40]. More distribution functions in the lattice configuration ensure Galilean invariance. For solving the energy and species conservation-based problems it is recommended to use D2Q9 over D2Q4 for stability issues. The velocity vector and weight factor for different 2-D configurations are given below.

$$\text{For D2Q4: } [\mathbf{e}] = \begin{bmatrix} 1 & 0 \\ -1 & 0 \\ 0 & 1 \\ 0 & -1 \end{bmatrix}, \quad [\omega] = \begin{bmatrix} 1/4 \\ 1/4 \\ 1/4 \\ 1/4 \end{bmatrix}, \quad e_s^2 = 1/2. \quad (3.11)$$

$$\text{For D2Q5: } [\mathbf{e}] = \begin{bmatrix} 0 & 0 \\ 1 & 0 \\ -1 & 0 \\ 0 & 1 \\ 0 & -1 \end{bmatrix}, \quad [\omega] = \begin{bmatrix} 2/6 \\ 1/6 \\ 1/6 \\ 1/6 \\ 1/6 \end{bmatrix}, \quad e_s^2 = 1/3. \quad (3.12)$$

$$\text{For D2Q9: } [\mathbf{e}] = \begin{bmatrix} 0 & 0 \\ 1 & 0 \\ -1 & 0 \\ 0 & 1 \\ 0 & -1 \\ 1 & 1 \\ -1 & 1 \\ -1 & -1 \\ 1 & -1 \end{bmatrix}, \quad [\omega] = \begin{bmatrix} 4/9 \\ 1/9 \\ 1/9 \\ 1/9 \\ 1/9 \\ 1/36 \\ 1/36 \\ 1/36 \\ 1/36 \end{bmatrix}, \quad e_s^2 = 1/3. \quad (3.13)$$

3.2.3 Three dimensional lattice

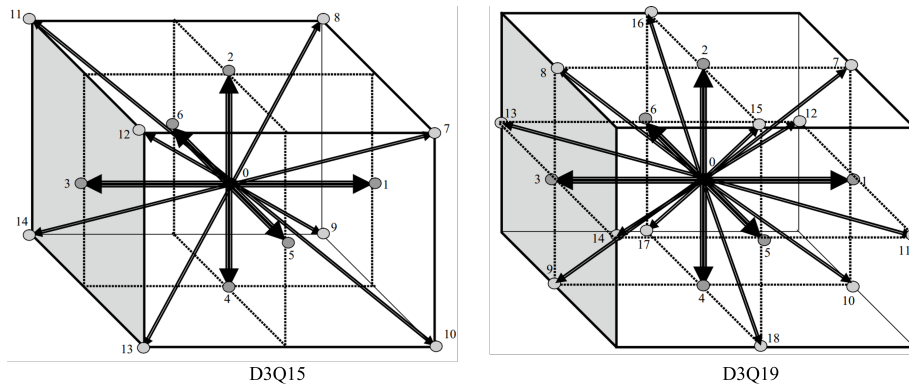


Figure 3.3: Lattice configurations for 3-D lattice [40].

The three-dimensional lattice configurations that are generally used, namely D3Q15 and D3Q19, are shown in Fig. (3.3). Though there exist some lower configurations such as D3Q7 and D3Q6, it is advised to use at least D3Q15 to maintain the system isotropy.

$$\text{For D3Q15: } [\mathbf{e}] = \begin{bmatrix} 0 & 0 & 0 \\ 1 & 0 & 0 \\ -0 & 1 & 0 \\ -1 & 0 & 0 \\ 0 & -1 & 0 \\ 0 & 0 & 1 \\ 0 & 0 & -1 \\ 1 & 1 & 1 \\ 1 & 1 & -1 \\ 1 & -1 & -1 \\ 1 & -1 & 1 \\ -1 & 1 & -1 \\ -1 & 1 & 1 \\ -1 & -1 & 1 \\ -1 & -1 & -1 \end{bmatrix}, \quad [\omega] = \begin{bmatrix} 16/72 \\ 16/72 \\ 16/72 \\ 16/72 \\ 16/72 \\ 16/72 \\ 16/72 \\ 1/72 \\ 1/72 \\ 1/72 \\ 1/72 \\ 1/72 \\ 1/72 \\ 1/72 \\ 1/72 \\ 1/72 \end{bmatrix}, \quad e_s^2 = 1/3 \quad (3.14)$$

$$\text{For D3Q19: } [\mathbf{e}] = \begin{bmatrix} 0 & 0 & 0 \\ 1 & 0 & 0 \\ -0 & 1 & 0 \\ -1 & 0 & 0 \\ 0 & -1 & 0 \\ 0 & 0 & 1 \\ 0 & 0 & -1 \\ 1 & 1 & 0 \\ -1 & 1 & 0 \\ -1 & -1 & 0 \\ 1 & -1 & 0 \\ 1 & 0 & 1 \\ 1 & 0 & -1 \\ -1 & 0 & -1 \\ -1 & 0 & 1 \\ 0 & 1 & 1 \\ 0 & 1 & -1 \\ 0 & -1 & -1 \\ 0 & -1 & 1 \end{bmatrix}, \quad [\omega] = \begin{bmatrix} 12/36 \\ 2/36 \\ 2/36 \\ 2/36 \\ 2/36 \\ 2/36 \\ 2/36 \\ 1/36 \\ 1/36 \\ 1/36 \\ 1/36 \\ 1/36 \\ 1/36 \\ 1/36 \\ 1/36 \\ 1/36 \\ 1/36 \\ 1/36 \\ 1/36 \end{bmatrix}, \quad e_s^2 = 1/3 \quad (3.15)$$

3.3 BGK Stability

The stability of the lattice Boltzmann equation with the BGK collision factor depends on the magnitude of the relaxation factor. It dictates the evolution of the distribution function (f) towards the equilibrium distribution function (f^{eq}). Depending on the value of $\tau/\Delta t$, f can relax in one of the three ways: under-relaxation, over-relaxation, and full-relaxation.

- **Under-relaxation:** For $\tau/\Delta t > 1$, the distribution function f decays exponentially towards the equilibrium distribution function f^{eq} .
- **Full-relaxation:** For $\tau/\Delta t = 1$, the distribution function f decays directly to the equilibrium distribution function f^{eq} .
- **Over-relaxation:** For $\tau/\Delta t < 1$, the distribution function f oscillates around f^{eq} with an exponential decay in the amplitude of oscillation.
- **Unstable:** In case of $\tau/\Delta t < 0.5$, the distribution function f oscillates around the equilibrium distribution function f^{eq} with an exponential increase in the amplitude of oscillation.

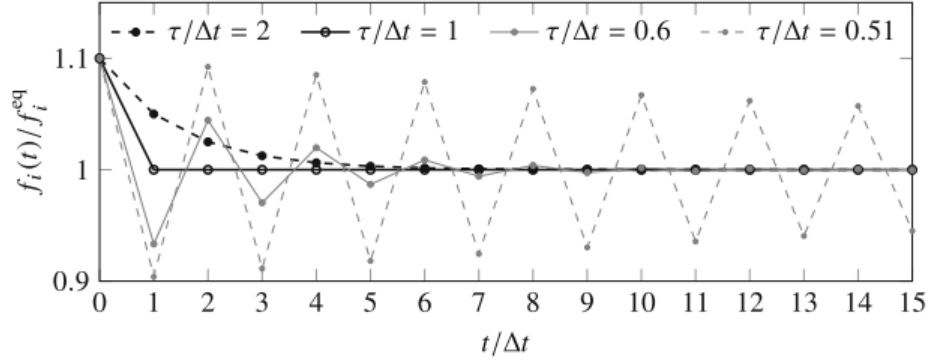


Figure 3.4: Evolution of the distribution function (f) for various relaxation factors [40].

The evolution pattern of the f for different relaxation factors is illustrated in Fig. 3.4. The non-negativity of all equilibrium distribution functions holds for all $\tau/\Delta t > 1/2$ and eventually, the simulation will be stable. The equilibrium functions are also a complicated function of velocity component as illustrated in eqn (3.7). For a BGK lattice Boltzmann equation with the collision operator of the form in eqn (3.7), the resultant velocity magnitude for a non-negative equilibrium distribution function for different lattice configurations is given by eqn (3.16) below.

$$|\mathbf{u}_{\max}| < \begin{cases} \sqrt{\frac{2}{3}} \frac{\Delta x}{\Delta t} \approx 0.816 \frac{\Delta x}{\Delta t} & : \text{D1Q3,} \\ \sqrt{\frac{1}{3}} \frac{\Delta x}{\Delta t} \approx 0.577 \frac{\Delta x}{\Delta t} & : \text{D2Q9, D3Q15, D3Q19, D3Q27.} \end{cases} \quad (3.16)$$

It is important to notice that the above limitation on velocity magnitude is derived for the bulk lattice Boltzmann equation and in simulations with the boundaries these conditions may be altered. The stability condition deteriorates with decreasing relaxation time i.e. $|\mathbf{u}_{\max}| \rightarrow 0$ as $\tau/\Delta t \rightarrow 1/2$ as shown for example in the Fig. 3.5 as investigated by Niu et al [41].

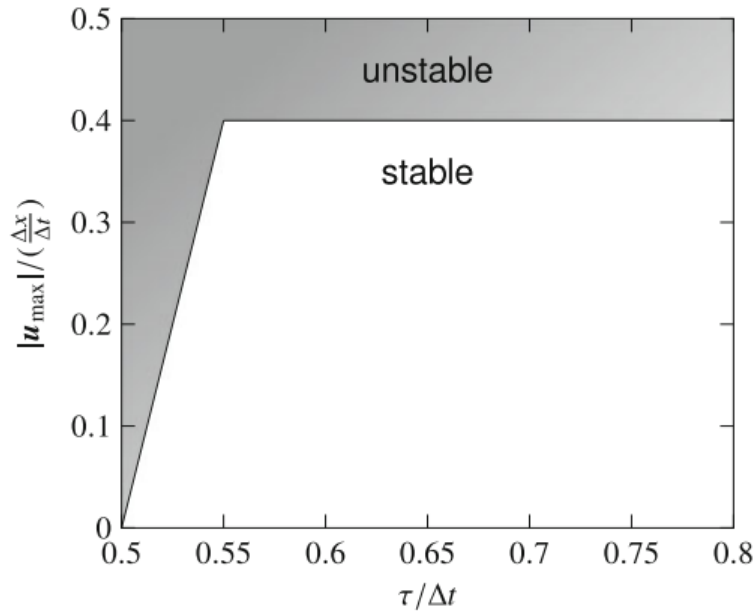


Figure 3.5: The linear stability sketch for 2D and 3D LBM simulations [42].

3.4 Similitude

Creating a link between the lattice and physical domains is essential to yield a sensible result. This link between the domains is accomplished using the non-dimensionalized terms (geometric and dynamic

similitude) from the governing equation. The lattice units are used in the LBM simulation, instead of the physical units. For example, in a 2-D simulation, the geometric similitude implies that $L/H = N/M$, where L and H are the physical x and y dimensions respectively, N and M , are the number of lattices in x and y direction. In the case of a diffusion problem the temporal linkage between the physical and lattice domains should also be considered. This can be accomplished with the non-dimensionalised diffusion coefficient, $\frac{tD}{H^2}|_{\text{physical}} = \frac{tD}{M^2}|_{\text{lattice}}$.

3.5 Boundary conditions

In CFD, the boundary conditions are explicitly known and hence can be directly applied. The boundary conditions from the physical domain have to be transformed to that applicable in the lattice domain. The distribution functions streaming away from the domain at the boundary are known from the streaming process and hence don't need modeling. The distribution functions that stream towards the domain at the boundary need to be calculated using the boundary condition. The general form of the boundary conditions is Dirichlet BC (value of the function is known at the boundary), Neumann BC (the derivative of the function is known at the boundary), Robin or mixed BC (Combination of both Neumann and Dirichlet BCs).

Dirichlet boundary condition

Let Γ be a known scalar value at the left boundary. For a 1-D problem using $D1Q2$ or $D1Q3$, then the only unknown will be f_1 and hence,

$$\Gamma = f_1 + f_2, \quad f_1 = \Gamma - f_2. \quad (3.17)$$

An altered approach could be using the equilibrium distribution functions,

$$f_1 = \omega_1 \Gamma + \omega_2 \Gamma - f_2. \quad (3.18)$$

For a 2-D situation with $D2Q4$ or $D2Q5$, the distribution functions streaming toward the domain can be given by,

$$f_1 = \omega_1 \Gamma + \omega_2 \Gamma - f_2. \quad (3.19)$$

In case of $D2Q9$ lattice configuration,

$$f_1 = f_1^{\text{eq}} + f_2^{\text{eq}} - f_2, \quad (3.20)$$

$$f_5 = f_5^{\text{eq}} + f_7^{\text{eq}} - f_7, \quad (3.21)$$

$$f_8 = f_8^{\text{eq}} + f_9^{\text{eq}} - f_6. \quad (3.22)$$

Mixed/Robin boundary condition

The generic form of the boundary condition is,

$$\frac{\partial \Gamma}{\partial x} = a\Gamma + b. \quad (3.23)$$

The flux in any direction can be written as the difference in the streaming function in that direction. If the flux is positive in the x-direction, then for the $D1Q2$ case we have,

$$f_1 - f_2 = a(f_1 + f_2) + b, \quad f_1 = \frac{f_2(1+a) + b}{1-a}, a \neq 1. \quad (3.24)$$

Thus, to perform a BGK-LBM simulation of a problem, the dimensions from the physical space have to be converted to that in the lattice space. Then the equilibrium distribution functions and relaxation factor are to be modelled from the macroscopic equation. The Chapman-Enskog analysis can be used to derive the relation between the relaxation factor, time step in lattice space, and the macroscopic transport properties. Thus, the next chapter deals with the aforementioned extension to solve the electrochemical transport phenomena followed by modelling the different boundary conditions in the form of distribution functions from the macroscopic equations.

Chapter 4

Diffusion

The implementation of LBM to solve the diffusion problem involves appropriate modelling of the equilibrium distribution function and the relaxation time. The BGK-LBM modelling of a diffusion problem is discussed in this chapter which involves non-dimensionalization, similitude analysis, and Chapman-Enskog analysis to determine the relationship between the diffusivity of species, evolution time step, and relaxation time, and the boundary condition.

4.1 Scaling

The unsteady homogeneous and heterogeneous diffusion problem in physical space is respectively described by

$$\frac{\partial C}{\partial t} = D\nabla^2 C + S, \quad (4.1)$$

and

$$\frac{\partial C}{\partial t} = D\nabla^2 C, \quad (4.2)$$

where D is the diffusivity of the species and S is a homogeneous source term. It is important to create a link between the physical domain and the lattice domain using the dynamic and geometric similarities existing in the problem. This is accomplished by nondimensionalizing the governing equation using appropriate length and time scales. Let \mathcal{L} , \mathcal{T} , \mathcal{C} denote the reference length, time, and concentration respectively, then the terms in the above diffusion equation can be non-dimensionalized as shown in eq. (4.3).

$$t^* = t/\mathcal{T}, \quad C^* = C/\mathcal{C}, \quad \nabla^{*2} = \nabla^2 \mathcal{L}^2, \quad (4.3)$$

where t^* , C^* , ∇^{*2} are the dimensionless parameters, and replacing them in the governing equation from the physical domain yields the non-dimensionalized governing equation for the diffusion problem.

$$\frac{\partial C^*}{\partial t^*} = \frac{D\mathcal{T}}{\mathcal{L}^2} \nabla^{*2} C^* + \frac{S\mathcal{T}}{\mathcal{C}\mathcal{L}^2} = D^* \nabla^{*2} C^* + S^*, \quad (4.4)$$

and

$$\frac{\partial C^*}{\partial t^*} = \frac{D\mathcal{T}}{\mathcal{L}^2} \nabla^{*2} C^* = D^* \nabla^{*2} C^*. \quad (4.5)$$

The heterogeneous unsteady governing equation for the diffusion problem will be considered for the BGK-LBM simulation. Similar to the Finite Difference Method (FDM), the LBM also involves the discretization of the lattice domain into lattice nodes and this is done through geometric similitude given by

$$t_{|\text{phy}}^* = t_{|\text{LBM}}^*, \quad l_{|\text{phy}}^* = l_{|\text{LBM}}^*. \quad (4.6)$$

Then, the dimensionless diffusivity also known as the Fourier number between the physical and lattice domains should be equal to meet the dynamic similitude given by

$$D_{|\text{phy}}^* = D_{|\text{LBM}}^*. \quad (4.7)$$

4.2 BGK-LBM scheme for diffusion problem

The lattice Boltzmann (LB) evolution equation for the heterogeneous diffusion equation of the form in eq. (4.5) is given by [40]

$$f_i(\mathbf{x} + \mathbf{e}_i \Delta t, t + \Delta t) - f_i(\mathbf{x}, t) = -\frac{1}{\tau} [f_i(\mathbf{x}, t) - f_i^{\text{eq}}(c^*)]. \quad (4.8)$$

Since the bulk velocity is zero, the equilibrium distribution function for a diffusion problem without advection becomes

$$f_i^{\text{eq}} = w_i C^*. \quad (4.9)$$

The distribution function is related to the macroscopic variable C^* by,

$$C^* = \sum_i f_i. \quad (4.10)$$

The link between the BGK-LBE and the diffusion equation can be determined using the Chapman-Enskog analysis. Through this, we can show that the results in macroscopic scale according to the diffusion equation with the diffusivity is related to the relaxation time τ as,

$$D_{\text{LBM}} = e_s^2 \left(\tau - \frac{\Delta t}{2} \right). \quad (4.11)$$

4.3 Initialization

Initialization of the distribution function f_i based on the macroscopic initial condition is essential to capture the transient evolution of the concentration. The simplest approach to initialization is to set the distribution functions equal to the equilibrium distribution function f_i^{eq} , i.e.

$$f_i(\mathbf{x}, t = 0) = f_i^{\text{eq}}(\mathbf{x}, t = 0) = w_i C^*(\mathbf{x}, t = 0). \quad (4.12)$$

4.4 Collision \rightarrow Streaming

As discussed in chapter 3, the LB evolution equation can be decomposed into two distinct parts that are performed in succession:

- **Collision or relaxation:**

$$f_i^*(\mathbf{x}, t) = f_i(\mathbf{x}, t) - \frac{\Delta t}{\tau} (f_i(\mathbf{x}, t) - f_i^{\text{eq}}(\mathbf{x}, t)), \quad (4.13)$$

where f_i^* denotes the distribution function after the collision. The above equation can be rearranged in a more convenient form as,

$$f_i^*(\mathbf{x}, t) = f_i(\mathbf{x}, t) \left(1 - \frac{\Delta t}{\tau} \right) + \frac{\Delta t}{\tau} (f_i^{\text{eq}}(\mathbf{x}, t)). \quad (4.14)$$

- **Streaming or propagation:**

After the collision operation, the resulting distribution functions f_i^* are streamed to the neighboring lattice nodes depending on the associated direction of the distribution function. The general form of the streaming operation is given by

$$f_i(\mathbf{x} + \mathbf{e}_i \Delta t, t + \Delta t) = f_i^*(\mathbf{x}, t). \quad (4.15)$$

The order of collision and streaming takes the analogy of the chicken or egg. To capture the transient evolution, the simulation has to start with a proper initialization followed by collision. This is due to the explicit discretization of the continuous Boltzmann equation. This indicates that the distribution function that is used to perform the collision operation is calculated from the known macroscopic variable. If the simulation is initialized with the correct equilibrium populations, and the propagation step is performed before collision, a new non-equilibrium will appear due to the spatial inhomogeneity of the flow field. This new non-equilibrium would be inconsistent with the previous non-relaxed flow field.

Thus to maintain the consistency between the macroscopic field variable C^* and the distribution function f_i , the collision operation needs to be performed first, followed by streaming, and then the computation of the moments. This sequence ensures that the simulation accurately captures the transient behavior of the field variable.

4.5 Boundary Conditions

Dirichlet, Newmann type flux, and periodic boundary conditions are the general boundary conditions used for the diffusion problem. Since this is a scalar transport model, the lattice configurations with fewer distribution functions are sufficient, namely D1Q3, D2Q4, D2Q5, D3Q7, and D3Q9. Further more, the boundary condition derivation to relate the distribution function towards the domain and the macroscopic value is derived for the left-side boundary.

Dirichlet boundary condition

For the one-dimensional simulation with D1Q3 lattice configuration as shown in Fig. (3.1), the distribution function towards the domain from the left boundary is f_1 . Then, the distribution function can be modelled to behave like a Dirichlet boundary condition using

$$f_1 = C^* - \sum_{i \neq 1} f_i. \quad (4.16)$$

For the two-dimensional simulation with D2Q5 lattice configuration as shown in Fig. (3.2), the distribution function f_1 , that is streaming towards the domain from the boundary is given by

$$f_1 = (w_1 + w_2)C^* - f_2. \quad (4.17)$$

The approach used in eq. (4.17) can be extended to model the functions streaming towards the domain in three-dimensional simulation.

Newmann flux boundary condition

The flux boundary conditions are generally of the form

$$\frac{\partial C^*}{\partial x^*} = -\Gamma. \quad (4.18)$$

In LBM, the gradients can be calculated locally by taking the first moment of the distribution functions given by

$$\frac{\partial C^*}{\partial x} = -\frac{1}{\tau e_s^2 \Delta x} \sum_i f_i \mathbf{e}_i \cdot \mathbf{e}_x. \quad (4.19)$$

And in the case of the D1Q3 lattice, the distribution function f_1 is given by

$$\frac{1}{e_s^2 \tau \Delta x} (f_1 - f_2) = \Gamma \implies f_1 = \tau e_s^2 \Delta x \Gamma + f_2. \quad (4.20)$$

For the two-dimensional case with the D2Q5 or D2Q4 lattice configuration, the distribution functions with the non-zero streaming velocity component ($\mathbf{e}_i \cdot \mathbf{e}_x \neq 0$) are f_1 and f_2 with f_1 streaming towards the domain from the left boundary. Thus, f_1 is given by

$$f_1 = \tau e_s^2 \Delta x \Gamma + f_2. \quad (4.21)$$

The approach used in eq. (4.20) can be extended to model the functions streaming towards the domain in three-dimensional simulation.

Periodic boundary condition

Periodic boundary conditions apply only to situations where the solution is periodic, and they state that the species leaving the domain on one side will, instantaneously, re-enter on the opposite side. Consequently, periodic boundary conditions conserve mass and momentum at all times. The implementation of the periodic boundary condition between the cyclic boundaries is illustrated in Fig. (4.1).

Thus, considering the left and right boundaries are periodic in solution, then the distribution function streaming into the domain from the left boundary is given by

$$f_1(\mathbf{x} = 0, \mathbf{y}) = f_1(\mathbf{x} = x_N, \mathbf{y}). \tag{4.22}$$

Similarly, the distribution function streaming into the domain from the right boundary is f_2 , and is defined by

$$f_2(\mathbf{x} = x_N, \mathbf{y}) = f_2(\mathbf{x} = 0, \mathbf{y}). \tag{4.23}$$

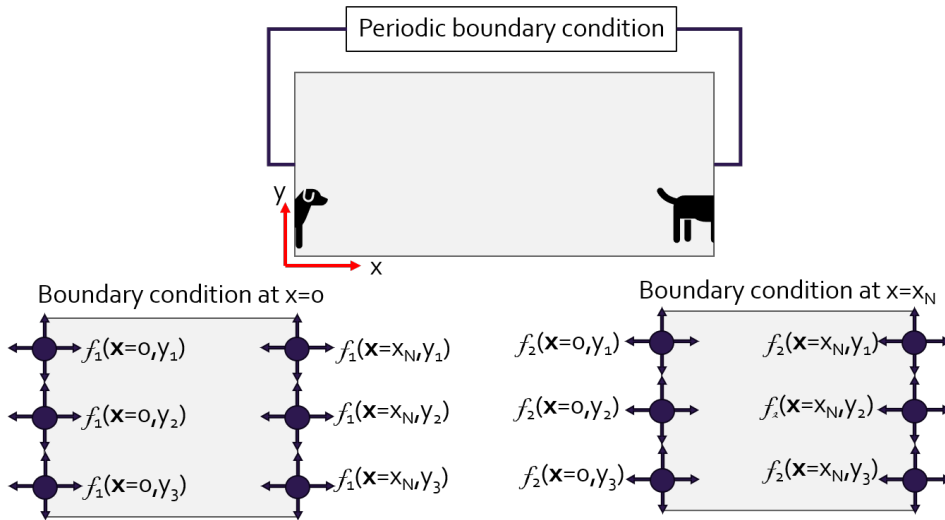


Figure 4.1: Periodic boundary condition for D2Q4 and D2Q5 lattice configuration.

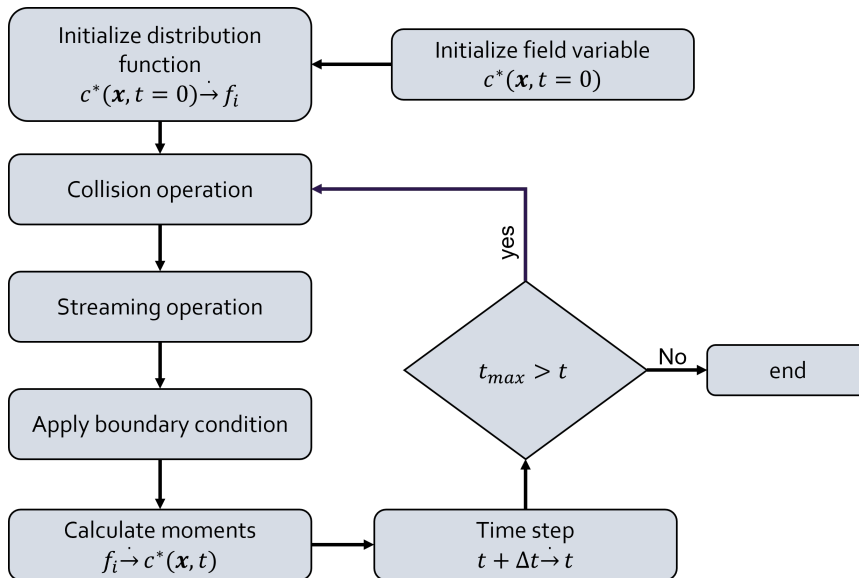


Figure 4.2: Flowchart for LBM simulation of unsteady diffusion problem.

In a nutshell, the LBM simulation of the unsteady diffusion problem should be approached by starting with the non-dimensionalization of the governing equation using the appropriate scales. After the correct

initialization of the distribution functions, the collision, streaming, boundary condition implementation and the recalculation of the field variable are orderly executed in a time loop as illustrated in Fig. (4.2). The methodology and the BGK-LBM algorithm for the diffusion problem are tested out and the results are discussed in the next section.

4.6 Implementation and validation

The methodology to simulate the diffusion of single species using the BGK-LBM was discussed in the previous sections. The one-dimensional diffusion problem is simulated using BGK-LBM with D1Q2 and D1Q3 lattice configurations. The D2Q5 and D2Q9 lattice configurations are implemented to execute the LB simulation of diffusion problem in a two-dimensional domain. The LBM results are compared to those solved using the FDM approach in the same lattice domain.

4.6.1 One-dimensional diffusion problem

The scaled domain considered for the one-dimensional diffusion problem is illustrated in the figure below.



Figure 4.3: Domain for one-dimensional diffusion problem.

The lattice domain length is $l = 100$ lu and the total simulation time in lattice units is 200. The diffusion coefficient in lattice units was arbitrarily taken to be 0.025. The lattice space step size is $\Delta x^* = 1$ lu and the time step size is $\Delta t^* = 1$. The domain is initialized with $C^*(t = 0) = 0$. For the BGK-LBM, both the D1Q3 and D1Q2 lattice configurations were implemented. Forward-Euler time discretization and central difference spatial discretization were used to perform the FDM in lattice space. To maintain the stability of the forward-Euler time discretization scheme, the relation between, the spatial, time step, and the transport variable is given by

$$\Delta t_{\text{FDM}}^* \leq \frac{0.5 \Delta x^{*2}}{D_{\text{LBM}}}, \quad \mathbf{1D}. \quad (4.24)$$

The time step for FDM simulation is computed by maintaining a common spatial step size value and transport variable with BGK-LBM simulation. The normalized concentration profile from the different simulation techniques pertaining to one-dimensional case are compared at time instance $t = 200$ lu in Fig. (4.4).

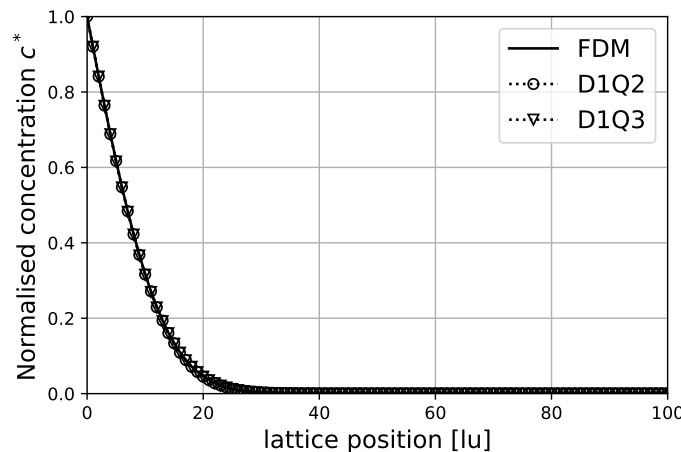


Figure 4.4: Dimensionless concentration distribution from FDM, D1Q2 and D1Q3 LBM at $t = 200$ lu.

4.6.2 Two-dimensional diffusion problem

The lattice domain of size 100×100 lu is used for the simulation of the diffusion problem represented in Fig. (4.5a). The total simulation time is 1000 lu and the diffusivity was taken to be 0.025 lu. The spatial steps in the lattice domain are set to unity ($\Delta x^* = \Delta y^* = 1$). For BGK-LBM simulation with D2Q5 and D2Q9 lattice configuration, the time step in lattice units is $\Delta t^* = 1$. The time step criteria for the stability of FDM simulation is given by

$$\Delta t_{\text{FDM}}^* \leq \frac{0.25 \Delta x^{*2}}{D_{\text{LBM}}}, \quad \mathbf{2D}. \quad (4.25)$$

The simulation results from different methods are illustrated in Fig. (4.5) and Fig. (4.6). The relative deviation between FDM and D2Q5 was estimated as 1.24%. The FDM and D2Q9 configuration simulation showed a relative deviation of 0.006%. The D2Q9 shows less deviation from the FDM result over the D2Q5 lattice configuration. The potential reason is, the D2Q9 is a higher order lattice with more distribution functions compared to the D2Q5 lattice configuration.

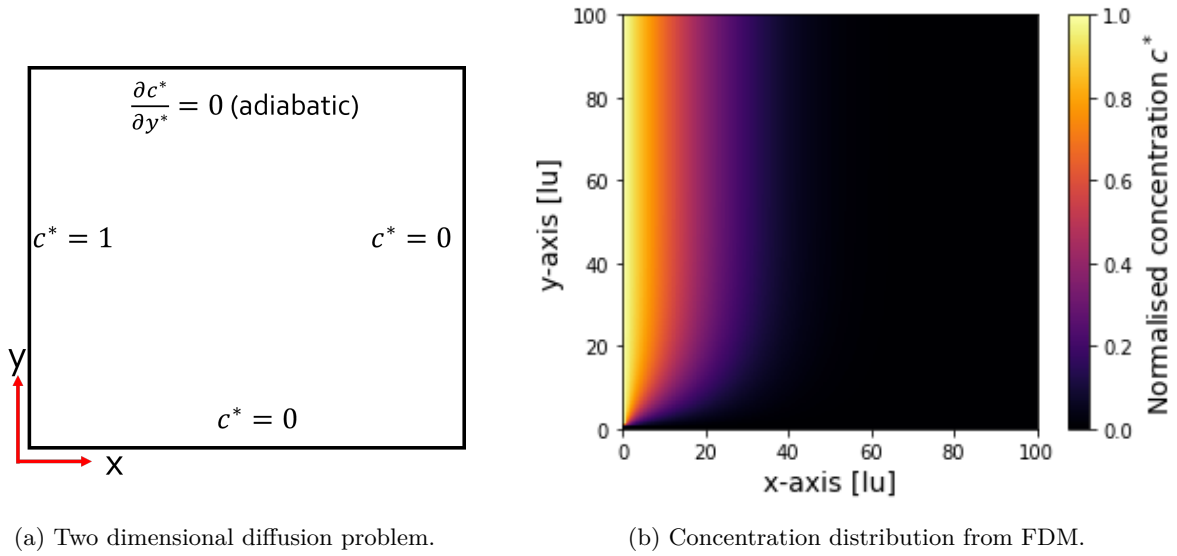


Figure 4.5: Domain description and FDM simulation result at $t = 1000$ lu.

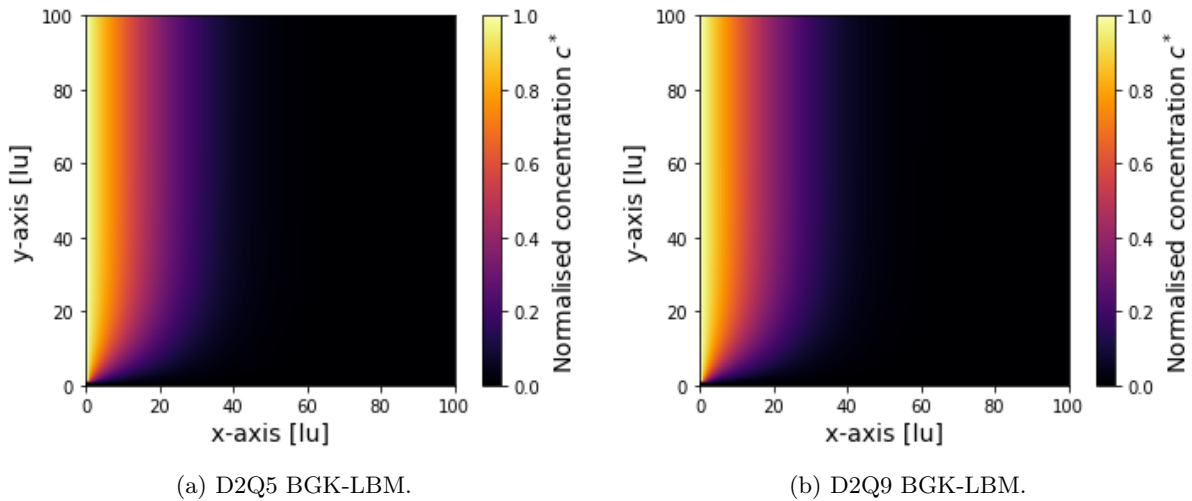


Figure 4.6: Two-dimensional BGK-LBM simulation result at $t = 1000$ lu.

Thus, the methodology to simulate the diffusion of a single species is implemented and the results are compared. The BGK-LBM simulation for the diffusion problem is validated against the results from the FDM simulation in lattice space and there exists a good agreement between them.

Chapter 5

Multi-species migration-diffusion

The migration-diffusion problem is a multi-physics system where the transport of the ionic species is dictated by the electric field that induces migration and the concentration gradient that induces diffusion. A detailed description of the migration-diffusion problem was discussed in Chapter 2. This system involves two governing equations: the ion transport equation and the electric potential distribution equation. The ion transport is governed by the heterogeneous material balance equation dictated by the Nernst-Planck transport model. The Poisson's equation governs the distribution of the electric potential. The methodology to simulate the multi-species migration-diffusion problem is discussed in this section.

5.1 Poisson's equation solver

The electric potential distribution across the electrolytic solution is governed by the Poisson's equation with a non-electroneutral source function. The Poisson's equation was discussed in detail in chapter 2, eq. (2.27). Since this is a steady-state equation, the LBM cannot be directly implemented to solve it because of its transient nature. To overcome this discrepancy, a pseudo-transient lattice Boltzmann simulation of the Poisson's equation can be executed. The other approach would be to solve the Poisson's equation using Finite Difference Method (FDM) in the lattice domain. The methodology to perform pseudo-transient simulation and FDM in lattice space is discussed in detail below.

5.1.1 Pseudo-transient BGK-LBM approach

To perform pseudo-transient simulation, an artificial time-dependent term (temporal derivative) is added to the actual Poisson's equation resulting in eq. (5.1). Then the LBM simulation is executed to solve for a steady-state solution of

$$\frac{\partial \Phi}{\partial t} = \nabla^2 \Phi + \frac{F}{\epsilon} \sum_{sp} z_{sp} c_{sp}. \quad (5.1)$$

Since it is a multi-species problem, the subscript 'sp' will be used to identify the species. The term $F \sum_{sp} z_{sp} c_{sp}$ represents the net charge density due to non-electroneutrality and is represented as ρ_e (C/m^3). The LB evolution equation for this transient Poisson's equation with a source term due to non-electroneutrality is given by

$$h_i(\mathbf{x} + \mathbf{e}_i \Delta t, t + \Delta t) - h_i(\mathbf{x}, t) = -\frac{1}{\tau_{\Phi}} [h_i(\mathbf{x}, t) - h_i^{eq}(\mathbf{x}, t)] + w_i \frac{\rho_e}{\epsilon}, \quad (5.2)$$

where h_i denotes the distribution function streaming in the i^{th} direction and τ_{Φ} represents the relaxation time for the Poisson's equation. The time t in the LB Poisson's equation is different from the physical time involved in the species transport equation that will be discussed in the following sections. Since the steady-state solution of the transient Poisson's equation is of interest, the time factor in eq. (5.2) has no physical meaning and so the time step Δt is set to one which results in

$$h_i(\mathbf{x} + \mathbf{e}_i \Delta x, t + 1) - h_i(\mathbf{x}, t) = -\frac{1}{\tau_{\Phi}} [h_i(\mathbf{x}, t) - h_i^{eq}(\mathbf{x}, t)] + w_i \frac{\rho_e}{\epsilon}. \quad (5.3)$$

The relaxation time (τ_Φ) can be estimated for the Poisson's equation using the Chapman-Enskog analysis [40] given by

$$\tau_\Phi = \frac{1}{2} + \frac{1}{e_s^2}. \quad (5.4)$$

The equilibrium distribution function h_i^{eq} can be calculated using

$$h_i^{\text{eq}} = w_i \Phi. \quad (5.5)$$

The distribution function is related to the macroscopic variable Φ as

$$\Phi = \sum_i h_i. \quad (5.6)$$

The initialization of the distribution function is similar to that discussed in the diffusion problem discussed in Chapter 4. The initial distribution function is given by

$$h_i(\mathbf{x}, t = 0) = h_i^{\text{eq}}(\mathbf{x}, t = 0) = w_i \Phi(\mathbf{x}, t = 0). \quad (5.7)$$

The next step after initialization is to decompose the LB evolution equation for transient Poisson's eq. (5.3) into collision and streaming operations.

- **Collision:**

$$h_i^*(\mathbf{x}, t) = h_i(\mathbf{x}, t) - \frac{\Delta t}{\tau_\Phi} (h_i(\mathbf{x}, t) - h_i^{\text{eq}}(\mathbf{x}, t)) + w_i \frac{\rho_e}{\epsilon}, \quad (5.8)$$

where h_i^* denotes the distribution function after the collision process.

- **Streaming:**

$$h_i(\mathbf{x} + \mathbf{e}_i \Delta t, t + \Delta t) = h_i^*(\mathbf{x}, t). \quad (5.9)$$

For the boundary condition implementation for the distribution functions streaming towards the domain from the boundary nodes, fusing both the streaming step and the boundary condition is possible [43]. Thus after the collision process, the general streaming step (eq. (5.9)) is replaced by the equations given below based on the type of boundary condition.

For a Dirichlet boundary condition of $\Phi = \zeta$ which is imposed at a boundary, the general streaming step is replaced by

$$h_i(\mathbf{x} + \mathbf{e}_i \Delta t, t + \Delta t) = -h_i^*(\mathbf{x}, t) + e_s^2 \zeta, \quad (5.10)$$

where h_i^* denotes the post-collision distribution function streaming in the direction opposite to that of h_i . Considering a D1Q3 lattice configuration, then the distribution function streaming toward the domain from the left boundary is h_1 , and the corresponding streaming process is given by

$$h_1(\mathbf{x} + \mathbf{e}_1 \Delta t, t + \Delta t) = -h_2^*(\mathbf{x}, t) + e_s^2 \zeta. \quad (5.11)$$

For a Neumann boundary condition with surface charge density σ_e (C/m²), the macroscopic boundary condition is given by

$$\nabla \Phi \cdot \mathbf{n}_s = -\frac{\sigma_e}{\epsilon}. \quad (5.12)$$

The streaming step for the distribution functions with Neumann boundary condition is given by

$$h_i = h_i^* + \frac{\sigma_e}{\epsilon}. \quad (5.13)$$

Thus, after executing the modified streaming process for all the distribution functions, the electric potential is calculated again using eq. (5.6), and the entire process is repeated in a pseudo-time loop until the steady-state solution is reached based on the convergence criteria given by

$$\frac{|\langle \Phi(\mathbf{x}, t) \rangle - \langle \Phi(\mathbf{x}, t-1) \rangle|}{|\langle \Phi(\mathbf{x}, t) \rangle|} < \epsilon_{\text{error}}, \quad (5.14)$$

where, $\langle \dots \rangle$ represents the volumetric average operator and ϵ_{error} represents the allowable tolerance in convergence. The flow chart explaining the sequence of operations to perform pseudo-transient simulation using BGK-LBM is shown in Fig. (5.1).

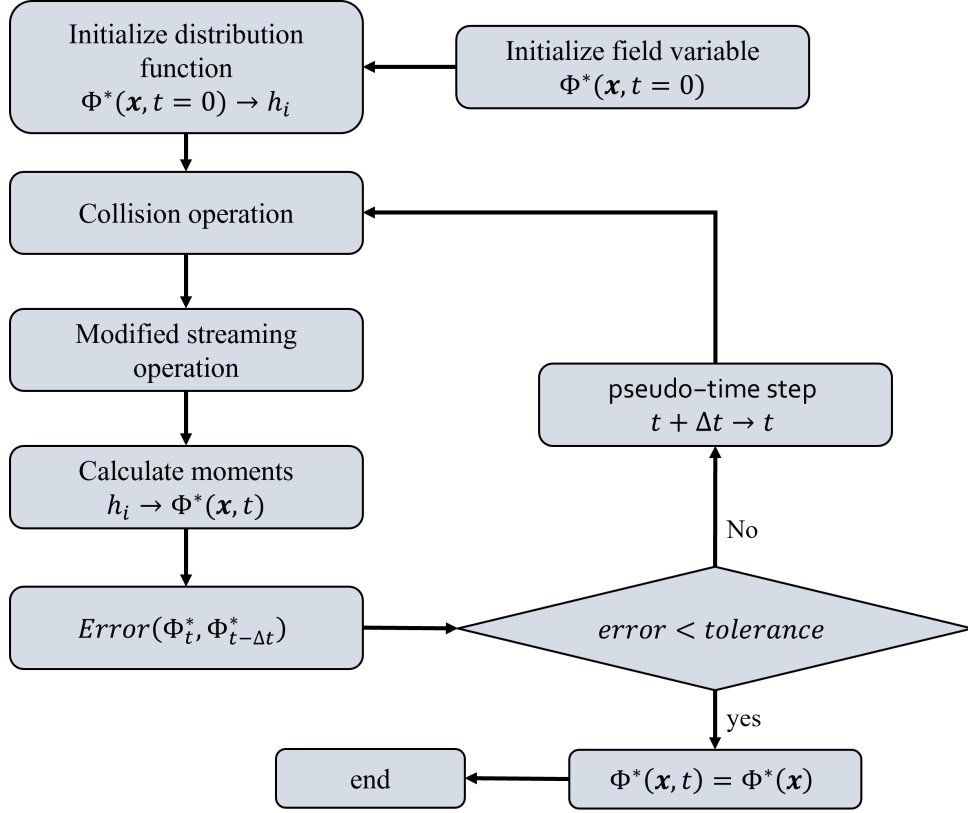


Figure 5.1: Flowchart for pseudo-transient LBM simulation of electric potential distribution.

5.1.2 FDM in lattice space

The other approach to solve the steady-state Poisson's equation for the migration-diffusion problem is to apply FDM in lattice space. FDM is a well-established numerical method that is relatively straightforward to implement, especially for simple geometries and boundary conditions. It involves discretizing the domain into a grid and solving partial differential equations (PDEs) using finite difference approximations. It is more memory-efficient than LBM, particularly when dealing with large and complex 3D domains. LBM often requires additional data structures to store distribution functions and track particle interactions, leading to higher memory consumption. The scaling of the Poisson's equation and the finite difference discretization technique is discussed below.

For the scaling of the Poisson's equation for potential let, \mathcal{L} , Φ_{ref} , C_{sp} denote the reference length, potential, and species concentration respectively. The reference potential is taken to be the thermal voltage given by eq. (5.15) and the bulk concentration is chosen as the reference concentration of the respective species. The dimensionless parameters in the Poisson's equation due to the reference scales are given by eq. (5.16).

$$\Phi_{\text{ref}} = \frac{RT}{F}. \quad (5.15)$$

$$\Phi^* = \frac{\Phi F}{RT}, \quad C_{\text{sp}}^* = \frac{C_{\text{sp}}}{C_{\text{sp}}}, \quad \nabla^2 = \frac{\nabla^{*2}}{\mathcal{L}^2}. \quad (5.16)$$

$$\nabla^{*2}\Phi^* = \frac{\mathcal{L}^2 F}{RT} \frac{F}{\epsilon} \sum_{\text{sp}} (z_{\text{sp}} C_{\text{sp}}^* C_{\text{sp}}). \quad (5.17)$$

The non-dimensionalized Poisson's equation given by eq. (5.17) will be discretized in lattice space using FDM. The central difference discretization scheme is used to discretize the second-order partial

5.2.1 Scaling

To create a link between the physical and the lattice domain, the above equation is scaled using reference parameters. Let \mathcal{L} , \mathcal{T} , C_{sp} , and Φ_{ref} denote the reference length, time, species concentration and potential. As aforementioned, the reference concentration and potential are bulk concentration and thermal voltage respectively. Scaling the parameters in the above equation with the reference values, results in the dimensionless Nernst-Planck equation given by

$$\frac{\partial C_{\text{sp}}^*}{\partial t^*} + \nabla^* \cdot \left[\left(-\frac{z_{\text{sp}} F D_{\text{sp}} \nabla^* \Phi^*}{RT} \right) C_{\text{sp}}^* \right] \frac{\mathcal{T} R T}{F \mathcal{L}^2} = D_{\text{sp}} \frac{\mathcal{T}}{\mathcal{L}^2} \nabla^{*2} C_{\text{sp}}^*. \quad (5.37)$$

The non-dimensionalized diffusivity is given by,

$$D_{\text{sp}}^* = \frac{D_{\text{sp}} \mathcal{T}}{\mathcal{L}^2}. \quad (5.38)$$

$$\frac{\partial C_{\text{sp}}^*}{\partial t^*} + \nabla^* \cdot [(-z_{\text{sp}} D_{\text{sp}}^* \nabla^* \Phi^*) C_{\text{sp}}^*] = D_{\text{sp}}^* \nabla^{*2} C_{\text{sp}}^*. \quad (5.39)$$

The migrating velocity of the ionic species ($\mathbf{u}_{\Phi, \text{sp}}^*$) is given by

$$\mathbf{u}_{\Phi, \text{sp}}^* = -z_{\text{sp}} D_{\text{sp}}^* \nabla^* \Phi^* = z_{\text{sp}} D_{\text{sp}}^* \mathbf{E}^*, \quad (5.40)$$

where \mathbf{E}^* denotes the dimensionless electric field vector. Thus, eq. (5.39) can be simplified as

$$\frac{\partial C_{\text{sp}}^*}{\partial t^*} + \nabla^* \cdot [\mathbf{u}_{\Phi, \text{sp}}^* C_{\text{sp}}^*] = D_{\text{sp}}^* \nabla^{*2} C_{\text{sp}}^*. \quad (5.41)$$

The negative gradient of electric potential or electric field in the eq. (5.40) is computed based on the choice of the Poisson solver approach. In the case of the LBM approach, the electric field can be computed locally using the first-moment of distribution functions for electric potential as,

$$\mathbf{E}^* \cdot \mathbf{n}_s = -\nabla^* \Phi^* \cdot \mathbf{n}_s = \frac{1}{\Delta x^* \tau_{\Phi} e_s^2} \sum_i h_i \mathbf{e}_i \cdot \mathbf{n}_s. \quad (5.42)$$

If the FDM in lattice space approach was used for electric potential calculation, then the electric field is computed using either first-order forward, backward, or central difference schemes depending on the location of the lattice node. The dimensionless diffusivity which is related to the Fourier number for neutral species or the inverse of the Peclet number for ions should be the same for both physical and lattice space, i.e.,

$$D_{\text{sp,phy}}^* = D_{\text{sp,LBM}}^*. \quad (5.43)$$

5.2.2 BGK-LBM scheme for Nernst-Planck Model

The LB evolution equation for the heterogeneous material balance equation with the Nernst-Planck model for flux, defined by eq. (5.41) is expressed as

$$f_{\text{sp},i}(\mathbf{x} + \mathbf{e}_i \Delta t, t + \Delta t) - f_{\text{sp},i}(\mathbf{x}, t) = -\frac{1}{\tau_{\text{sp}}} [f_{\text{sp},i}(\mathbf{x}, t) - f_{\text{sp},i}^{\text{eq}}], \quad (5.44)$$

where, $f_{\text{sp},i}$ denotes the distribution function of sp^{th} species streaming in the i^{th} direction and τ_{sp} denotes the relaxation time of species for Nernst-Planck equation. By convention, the temporal and spatial steps in lattice space are chosen to be unity. The corresponding equilibrium function is modeled by identifying the similarity between the normalized Nernst-Planck macroscopic equation and a generic advection-diffusion equation. The eqn(5.41) is analogous to the advection-diffusion problem with the difference that the advective velocity is replaced by the migrating velocity. Thus the equilibrium distribution function is given by [40, 42, 43]

$$f_{\text{sp},i}^{\text{eq}} = w_i C_{\text{sp}}^* \left(1 + \frac{\mathbf{e}_i \cdot \mathbf{u}_{\Phi, \text{sp}}^*}{e_s^2} \right). \quad (5.45)$$

The relation between the macroscopic variable (concentration) and the distribution functions pertinent to a species sp is given by

$$C_{\text{sp}}^* = \sum_i f_{\text{sp},i}. \quad (5.46)$$

The species relaxation time in BGK-LB evolution equation can be computed from the Chapman-Enskog derivation for Nernst-Planck electro-diffusion equation [42, 43] as,

$$\tau_{\text{sp}} = \frac{1}{2} + \frac{D_{\text{sp}}^*}{e_s^2}. \quad (5.47)$$

The pseudo-sound speed e_s depends on the lattice configuration chosen for simulation. Thus, the Chapman-Enskog analysis provides the link between the BGK-LBE and the Nernst-Planck electro-migration model.

5.2.3 Common vs different relaxation time for species

For a multi-species system, each species can have the same relaxation time which is set to unity results in different reference or evolution time for each species [43] determined by

$$\Delta t_{\text{sp}} = \frac{D_{\text{sp, LB}} \Delta x^2}{D_{\text{sp, LB}}}, \quad (5.48)$$

Then the number of internal LB time steps of a particular species depends on the time conversion factor of each species. The species with the maximum time conversion factor will have a single internal iteration and the corresponding time step will be set as the main evolution time step. For the other species, the number of internal iterations is an integer resulting from the ratio of the maximum time conversion factor to that of the species. For example, in a system of N species, if $\text{sp}=1$ has the maximum time conversion factor, then the number of temporal internal iterations of each species ($N_{\text{t,sp}}$) is given by

$$N_{\text{t,sp}} = \frac{\max\{\Delta t_{\text{sp}}\}}{\Delta t_{\text{sp}}}, \text{ where } N_{\text{t,sp}} \in \mathcal{Z}. \quad (5.49)$$

Since the number of internal time iterations need not be an integer, the final time instance of each species will be higher or lower than the set time instance, resulting in under or over-evolution of the species. This will generate discrepancies in the calculation of charge density at a particular time instance for the Poisson solver since we do not have all the ionic species distribution at that exact time instance. To overcome this issue, the time conversion factor for all the species is set to be equal and hence, the relaxation time is calculated to be different for each species. Thus, the internal iteration of all the species is set to one and the evolution behavior of the species will be dictated by the relaxation time (τ_{sp}) of the associated species. It must be noted that the chosen reference length and time scales should ensure the stability criteria for relaxation time ($\tau_{\text{sp}} \in (0.5, 2)$) [42].

5.2.4 Initialization

Before initializing the distribution functions for species concentration ($f_{\text{sp},i}$), the migrating velocity is calculated based on the initialized electric potential distribution. Then the distribution function of the species is initialized by equating it to the corresponding distribution function given by

$$f_{\text{sp},i}(\mathbf{x}, t = 0) = f_{\text{sp},i}^{\text{eq}}(C_{\text{sp}}^*, \mathbf{u}_{\Phi, \text{sp}}^*, t = 0) = w_i C_{\text{sp}}^*(\mathbf{x}, t = 0) \left[1 + \frac{\mathbf{e}_i \cdot \mathbf{u}_{\Phi, \text{sp}}^*(\mathbf{x}, t = 0)}{e_s^2} \right]. \quad (5.50)$$

5.2.5 Collision \rightarrow Streaming

After the initialization of the distribution functions, the collision and streaming operations resulting from the decomposition of the LB evolution eq. (5.44) are performed.

- **Collision:**

$$f_{\text{sp},i}^*(\mathbf{x}, t) = f_{\text{sp},i}(\mathbf{x}, t) - \frac{\Delta t}{\tau_{\text{sp}}} (f_{\text{sp},i}(\mathbf{x}, t) - f_{\text{sp},i}^{\text{eq}}(\mathbf{x}, t)) \quad (5.51)$$

Here, $f_{\text{sp},i}^*$ denotes the distribution function after the collision operator. The above equation can be rearranged in a more convenient form given below by

$$f_{\text{sp},i}^*(\mathbf{x}, t) = f_{\text{sp},i}(\mathbf{x}, t) \left(1 - \frac{\Delta t}{\tau_{\text{sp}}} \right) + \frac{\Delta t}{\tau_{\text{sp}}} (f_{\text{sp},i}^{\text{eq}}(\mathbf{x}, t)). \quad (5.52)$$

- **Streaming:**

The post-collision distribution functions $f_{sp,i}^*$ are streamed to the neighboring lattice nodes depending on the propagating direction of the distribution function. The general streaming operation after the collision process is given by

$$f_{sp,i}(\mathbf{x} + \mathbf{e}_i \Delta t, t + \Delta t) = f_{sp,i}^*(\mathbf{x}, t). \quad (5.53)$$

5.2.6 Boundary condition

The boundary conditions for the distribution functions streaming towards the domain at the boundary are to be modeled after the streaming process. As discussed in Chapter 1, the different boundary conditions for concentration in the Nernst-Planck model are the Dirichlet and Newmann type zero, or non-zero flux boundary conditions. Modeling of the Dirichlet boundary condition is not discussed, since it is straightforward to implement and discussed in Chapter 3 and Chapter 4. The methodology to model the flux boundary in LBM is discussed below.

For a flux \mathbf{N}_{sp} [mol/m²s], defined on the left boundary whose normal is along the +x-direction, the electro-diffusive flux equation in physical space is given by

$$\left(\frac{z_{sp} F D_{sp} C_{sp} E_x}{RT} \right) - (D_{sp} \frac{\partial C_{sp}}{\partial x}) = N_{x,sp}. \quad (5.54)$$

Normalizing this flux with the reference scales yield,

$$\left(\frac{z_{sp} F D_{sp} C_{sp}^* E_x^*}{RT} \right) \left[\frac{C_{sp} RT}{F \mathcal{L}} \right] - \left(D_{sp} \frac{\partial C_{sp}^*}{\partial x^*} \right) \left[\frac{C_{sp}}{\mathcal{L}} \right] = N_{x,sp}, \quad (5.55)$$

$$z_{sp} C_{sp}^* E_x^* - \left(\frac{\partial C_{sp}^*}{\partial x^*} \right) = N_{x,sp} \left(\frac{\mathcal{L}}{C_{sp} D_{sp}} \right). \quad (5.56)$$

The units of \mathcal{L} , C_{sp} , and D_{sp} are m, mol/m³, and m²/s respectively. Thus, from the above derivation the non-dimensional flux of a species is given by,

$$N_{x,sp}^* = N_{x,sp} \left(\frac{\mathcal{L}}{C_{sp} D_{sp}} \right). \quad (5.57)$$

The next step after scaling the flux equation to the lattice domain is to derive an expression for the distribution function $f_{sp,1}$, which is the distribution function streaming towards the domain from the left boundary. This is achieved by expressing the macroscopic variables in eq. (5.56) using the corresponding distribution functions.

For D1Q3 lattice configuration,

$$z_{sp} E_x^* \sum_{i=0}^2 f_{sp,i} + \frac{1}{e_s^2 \tau_{sp}} \sum_{i=0}^2 f_{sp,i} \mathbf{e}_i \cdot \mathbf{e}_x = N_{x,sp}^*, \quad (5.58)$$

$$z_{sp} E_x^* (f_{sp,1} + f_{sp,2} + f_{sp,0}) + \frac{1}{e_s^2 \tau_{sp}} (f_{sp,1} - f_{sp,2}) = N_{x,sp}^*, \quad (5.59)$$

$$f_{sp,1} = \frac{N_{x,sp}^* + \left(\frac{f_{sp,2}}{e_s^2 \tau_{sp}} \right) - z_{sp} E_x^* (f_{sp,2} + f_{sp,0})}{z_{sp} E_x^* + \left(\frac{1}{e_s^2 \tau_{sp}} \right)}. \quad (5.60)$$

For the two-dimensional case with the D2Q5 lattice configuration, the distribution functions with the non-zero streaming velocity component ($\mathbf{e}_i \cdot \mathbf{e}_x \neq 0$) are $f_{sp,1}$ and $f_{sp,2}$ with $f_{sp,1}$ streaming towards the domain from the left boundary. Thus, $f_{sp,1}$ is given by,

$$z_{sp} E_x^* \sum_{i=0}^4 f_{sp,i} + \frac{1}{e_s^2 \tau_{sp}} \sum_{i=0}^4 f_{sp,i} \mathbf{e}_i \cdot \mathbf{e}_x = N_{i,sp}^*, \quad (5.61)$$

$$f_{sp,1} = \frac{N_{x,sp}^* + \left(\frac{f_{sp,2}}{e_s^2 \tau_{sp}} \right) - z_{sp} E_x^* \sum_{i \neq 1} f_{sp,i}}{z_{sp} E_x^* + \left(\frac{1}{e_s^2 \tau_{sp}} \right)}. \quad (5.62)$$

The above-followed approach can be replicated to derive the flux boundary condition in lattice space for a three-dimensional domain (D3Q7 configuration) and the other boundaries with different normal vectors. The implementation of periodic boundary conditions is identical to that discussed in the previous chapter and hence is not discussed here.

The overall procedure to model the electrokinetics of species due to migration and diffusion involves coupling the Poisson and the Nernst-Planck solver. During each main temporal iteration, the steady-state electric potential solution is transferred to the Nernst-Planck solver. The local charge density (ρ) which is calculated using the ionic species distribution from the Nernst-Planck solver is transferred to the Poisson solver. This exchange of information between the solvers at each time step is illustrated in Fig. (5.2a). The overall algorithm to simulate the electro-diffusion of species in electrolyte using the BGK-LBM is listed below.

- **Scaling:** The reference scales to normalize the Poisson and Nernst-Planck solver should be the same. In general, the reference scales should ensure stability while performing LBM simulation. Then the number of lattice nodes and time iterations is computed by setting $\Delta x = \Delta t = 1$ for simplicity of calculation.
- **Initialization:** The potential and species concentrations are initialized followed by the initialization of the migrating velocity which is a function of the electric potential and species concentration. Then the distribution functions for Poisson and Nernst-Planck models are computed using the initialized macroscopic variables.
- After the initialization of the distribution functions, transient simulation is performed by solving the LB evolution equation for the Poisson and Nernst-Planck model.
 1. The electric potential is solved using any of the techniques for the Poisson solver for a steady-state solution.
 2. Exchange of information between the Poisson-Nernst-Planck solver. The electric potential calculated from step(1), is used to solve the Nernst-Planck model for species distribution.
 3. Go back to step (1) and calculate the new electrical potential distribution according to the new local charge density calculated in step (2). This cycle is repeated for the preset number of time steps, i.e. t_{max} .

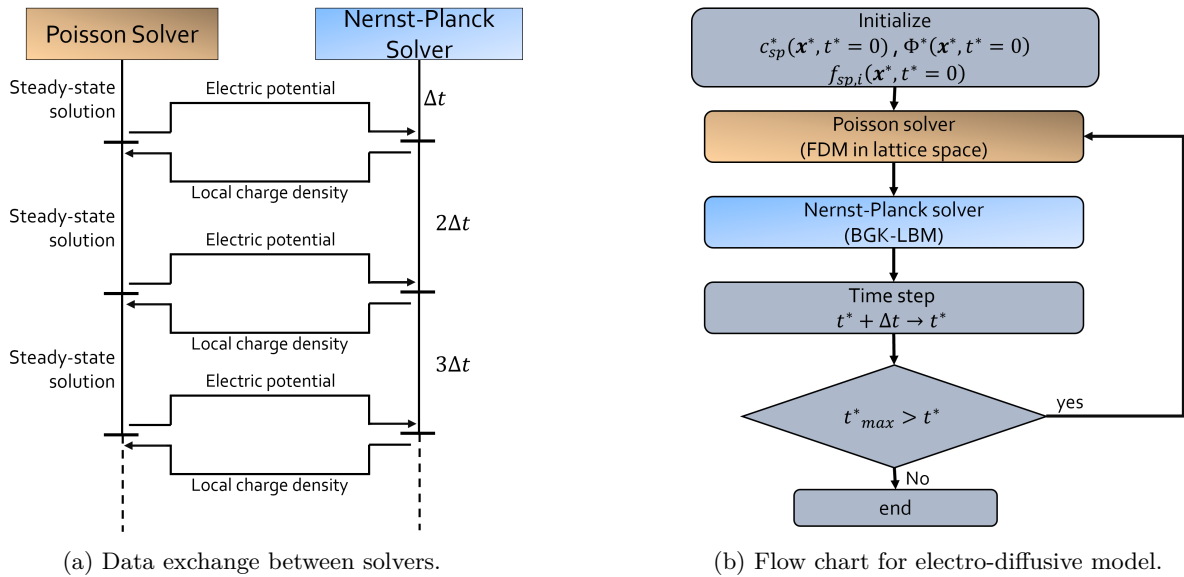


Figure 5.2: Flow chart and data exchange architecture for electro-diffusive model.

The ‘FDM in lattice space’ approach is used to solve the steady-state Poisson’s equation for electric potential distribution. This approach is chosen considering the simplicity of implementation and the low memory economy relative to the LBM. The flow chart to solve the migration-diffusion problem using the chosen numerical techniques is represented in Fig. (5.2b).

5.3 Migration-diffusion problem with reaction kinetics

The coupling of the reaction kinetics solver with the Poisson-Nernst-Planck solver to model the heterogeneous reactive migration-diffusion problem is discussed in this section. The reaction kinetics solver provides the rate of the reaction in the form of kinetic current density. In the case of hydrogen evolution reaction (HER), the kinetic current density is calculated using the Butler-Volmer equation given by eq. (2.18). Then the current density is used to calculate the species flux at the reacting site by scaling with the stoichiometric coefficient and Faraday’s constant given by eq. (2.24). The reaction kinetics solver is also solved at each time step as it is dependent on the local concentration of reacting and produced species. The over-potential which highly dictates the rate of the reaction is also dependent on the local concentration due to the Nernst potential correction and hence has to be calculated at each time step. For HER, the over-potential with the Nernst potential correction for cathodic equilibrium potential ($\phi_{e,c}$) is given by eq. (2.19).

After converting the kinetic current density [A/m^2] to species flux [mol/m^2s] at the reacting site, the LB distribution functions streaming towards the domain are modelled following the methodology discussed in section(5.2.6). It is important to note that the current density resulting from the kinetics solver holds the units from physical space and so the inputs to the kinetics solver have to be scaled from the lattice space to physical space using the appropriate reference values. Thus, the over-potential, local concentration of the reacting and produced species at the reaction boundary site should have physical units.

For a situation where the HER occurs at the left boundary where ($x = x^* = 0$), the equations solved by the kinetic solver using the local field variables are given below. First, the over-potential is computed as

$$\eta_c = \phi_s - \left(\phi_{e,c} + \frac{2.303RT}{nF} \left[14 + \log_{10} \left(\frac{C_{OH^-}(x=0)}{1000} \right)^2 \right] \right). \quad (5.63)$$

The hydroxide concentration in the above equation is scaled by 1000 to convert the concentration density from mol/m^3 to molarity. The over-potential thus calculated holds the unit of voltage (V). The Butler-Volmer kinetic current density equation for HER given by the eq. (5.64) gives current density in A/m^2 .

$$j_n = j_{o,c}^{ref} \left[\left(\frac{C_{OH^-}(x=0)}{C_{OH^-}^{ref}} \right)^2 \left(\frac{C_{H_2}(x=0)}{C_{H_2}^{ref}} \right) e^{\left(\frac{\alpha_a F \eta_c}{RT} \right)} - \left(\frac{C_{H_2O}(x=0)}{C_{H_2O}^{ref}} \right)^2 e^{\left(\frac{-\alpha_c F \eta_c}{RT} \right)} \right] \quad (5.64)$$

The species flux at the reacting boundary computed using the current density (A/m^2) is then normalized and the LB streaming functions towards the domain are computed for electro-diffusive flux type boundary condition. The simulation procedure for solving the heterogeneous migration-diffusion problem coupled with reaction kinetics is listed below.

After scaling and initialization,

1. The electric potential is solved using the FDM in the lattice space method.
2. Scale the appropriate field data from lattice to physical space and then compute the over-potential followed by kinetic current density in A/m^2 .
3. Exchange of information between the Poisson and Nernst-Planck solver. The exchange of information between the reaction kinetics and Nernst-Planck solver. The electric potential and current density computed from steps (1) and (2) respectively are used to solve the Nernst-Planck model for species distribution.

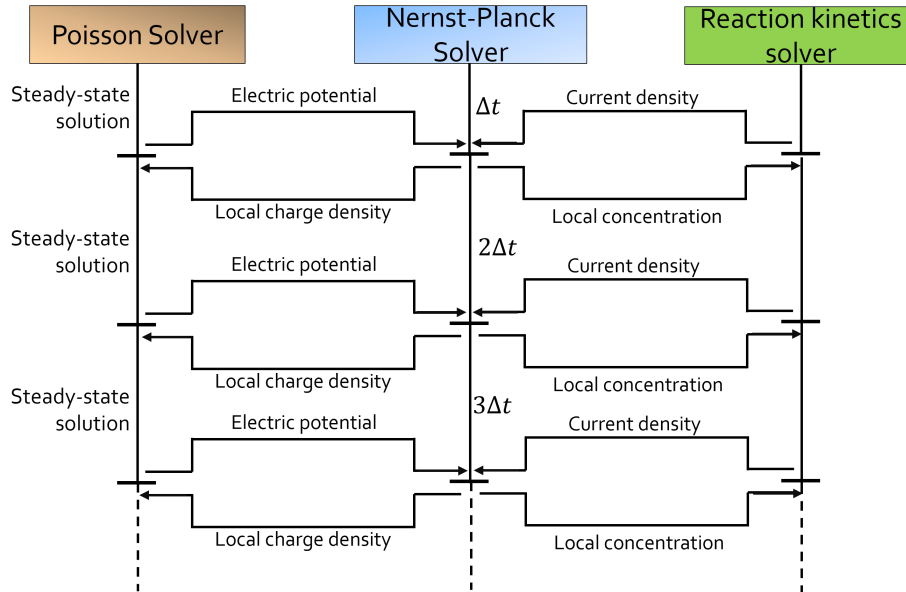


Figure 5.3: Data exchange between the Poisson-Nernst-Planck and reaction kinetics solver.

4. Go back to step (1) and calculate the new electric potential distribution according to the new local charge density distribution calculated from step (3). Then compute the new over-potential and current density using the local concentration density at the reacting boundary computed from step (3). This cycle is repeated for the preset number of time steps.

The information exchange architecture between the Poisson, Nernst-Planck, and the reaction kinetics solver is represented in Fig. (5.3). Fig. (5.4) represents the flow chart illustrating the sequence of the calculation for solving the migration-diffusion problem with the reaction BC. Thus, in the upcoming chapters, the methodology explained in this chapter will be validated and extended to simulate the transport phenomena occurring in the hydrogen half-cell.

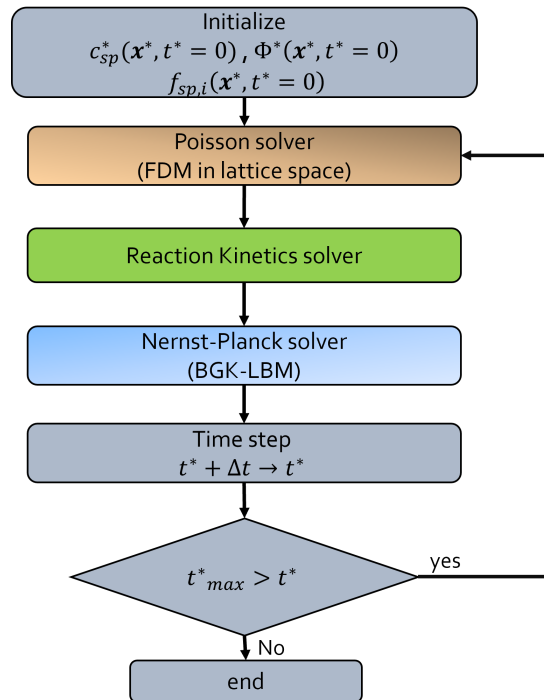


Figure 5.4: Flow chart for migration-diffusion problem with reaction.

Chapter 6

Validation: ion migration

The Nernst-Planck transport model derived in the previous chapter is a passive scalar transport equation because it dictates the transportation of scalar quantity (concentration density) by migration and diffusion. Thus, D1Q3 and D2Q5 lattice configurations are sufficient to simulate the migration-diffusion problem using BGK-LBM. The methodology discussed in the previous chapter is used to simulate the system that follows the Debye-Hückel theory for electric potential and ionic species concentration density distribution. Then the BGK-LBM results are compared to the Debye-Hückel expressions and FDM results to validate the methodology.

6.1 Debye-Hückel theory

For an electrolytic solution near a charged electrode, the local electrolytic potential drops to zero at a certain distance away from the charged wall. If the ion concentration density at this point is equal to the bulk concentration density, then the ion concentration density distribution will follow the Boltzmann distribution [44] given by

$$C_{\text{sp}}^* = \frac{C_{\text{sp}}}{C_{\text{sp},\infty}} = e^{\left(\frac{-z_{\text{sp}}F\phi}{RT}\right)}, \quad (6.1)$$

where $C_{\text{sp},\infty}$ denotes the bulk concentration density of the species. For a 1:1 symmetric electrolytic solution such as KOH ($C_{\text{K}^+,\infty} = C_{\text{OH}^-\infty} = C_{\text{sp},\infty}$), the electric potential distribution given by the Poisson equation (eq. (2.27)) transforms to a nonlinear Poisson Boltzmann equation. In a one-dimensional domain, the Poisson-Boltzmann equation [43] is given by

$$\frac{d^2\Phi}{dx^2} = \frac{2C_{\text{sp},\infty}F}{\epsilon} \sinh\left(\frac{F\Phi}{RT}\right). \quad (6.2)$$

The above equation cannot be solved analytically. If the magnitude of the argument of the hyperbolic sine function is very small, the Poisson-Boltzmann equation (eq. (6.2)) can be reduced to the Debye-Hückel expression given by

$$\frac{d^2\Phi}{dx^2} = \frac{2C_{\text{sp},\infty}F}{\epsilon} \left(\frac{F\Phi}{RT}\right) = \frac{1}{\lambda^2}\Phi, \quad \forall \left|\frac{F\Phi}{RT}\right| \ll 1, \quad (6.3)$$

where λ denotes the Debye length. For a system with $\Phi(x=0) = \Phi_o V$ and $\Phi(x=\infty) = 0 V$ as the boundary conditions, the solution to eqn(6.3) is given by

$$\Phi(x) = \Phi_o \exp\left(\frac{-x}{\lambda}\right). \quad (6.4)$$

The expression for the ion concentration given by eq. (6.1) can be expressed as,

$$C_{\text{sp}}(x) = C_{\text{sp},\infty} \exp\left(\frac{-z_{\text{sp}}F\phi(x)}{RT}\right). \quad (6.5)$$

Thus, the ion concentration density and electric potential profiles resulting from the LBM simulation will be validated against the Debye-Hückel expressions given by eq. (6.4,6.5).

6.2 Grid independence study

The lattice domain is divided into a number of lattice nodes for simulation. There can be deviations in results depending on the number of lattice nodes. Thus a grid independency study has to be performed to determine the optimal number of lattice nodes required for simulation. Since the spatial step size in LBM is set to unity, the number of lattice nodes is dependent on the reference length scale. To ensure that the simulation resolves the physics in the electric-double layer, the reference length scale has to be lower than the Debye length (λ). Thus, initially, the reference length scale is chosen such that the electric-double layer is resolved by two lattice nodes and then the reference length is reduced to increase the number of lattice nodes in the electric-double layer until the desired grid-independent result is achieved. The relaxation factor of the species are maintained the same for different grid sizes. Fig. (6.1), shows that there is no significant deviation in the distribution functions from $\mathcal{L} = \lambda/10$. Hence, the resolution pertaining to $\mathcal{L} = \lambda/10$, is used for the further studies.

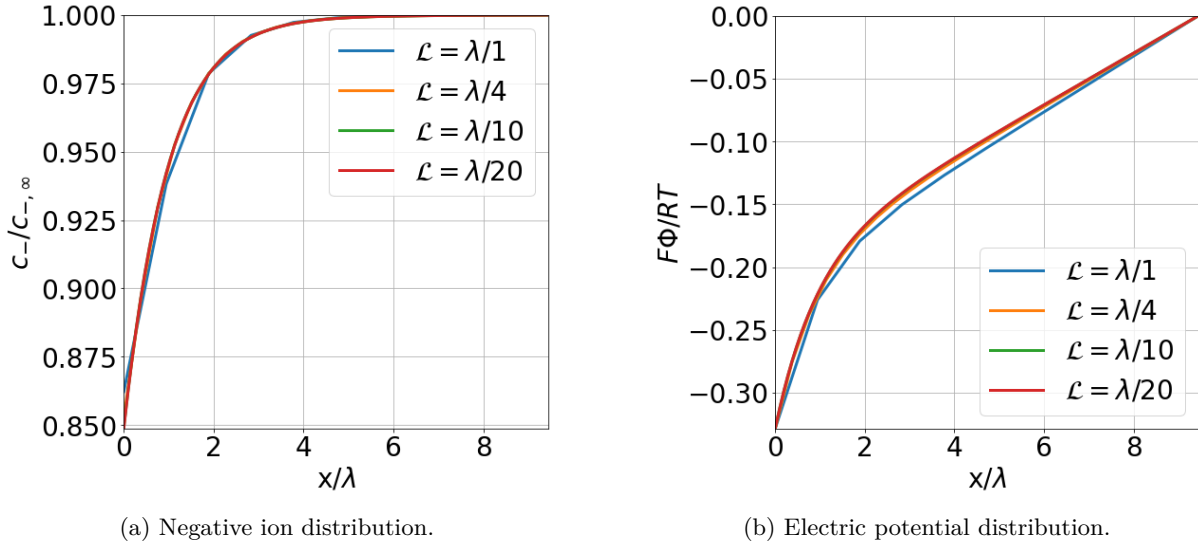


Figure 6.1: Grid independence study.

6.3 Ion migration

Parameter	Symbol	Physical value	Lattice value
Domain length	L	1 μm	100
Grid size	Δx	0.01 μm	1
Debye length	λ	0.10595 μm	10
Time step	Δt	1.28×10^{-10} s	1
Ion diffusivity	$D_+ = D_-$	5.27×10^{-9} m ² /s	0.0067
Bulk concentration	$C_{+, \infty} = C_{-, \infty}$	0.01 mol/m ³	1

Table 6.1: Physical parameters and the corresponding lattice values for Debye-Hückel validation

A one-dimensional domain with D1Q3 lattice configuration is chosen for the study and the corresponding boundary conditions in physical space are given in Fig. (6.2). A constant electric potential of $\Phi_o = -10$ mV is applied on the left boundary, while zero electric potential is applied on the right boundary. The no-flux condition and bulk concentration of 0.01 mol/m³ are set as the conditions for ionic species at the left and right boundary respectively. The simulation parameters in physical and lattice space are listed in the Table (6.1).



Figure 6.2: Domain to validate LBM with Debye-Hückel theory.

The simulation was performed until the electric potential and the ionic species reached a steady-state distribution. These results are validated with the distribution defined by the Debye-Hückel theory as shown in Fig. (6.5). The results show that there is a good agreement between the BGK-LBM simulation and the analytical results.

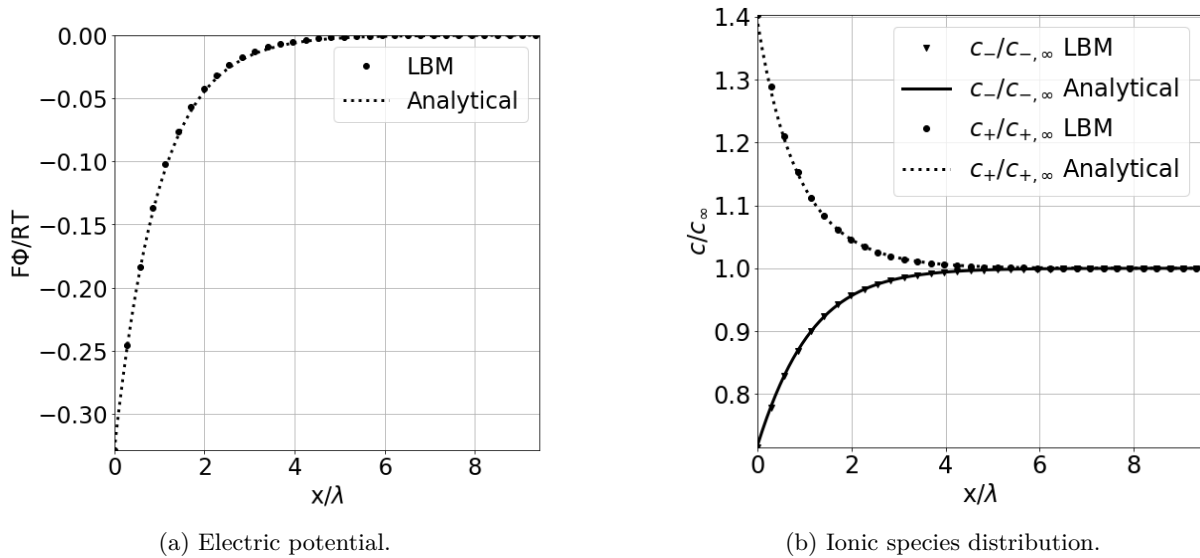


Figure 6.3: Comparison of analytical and LBM results for ion concentration.

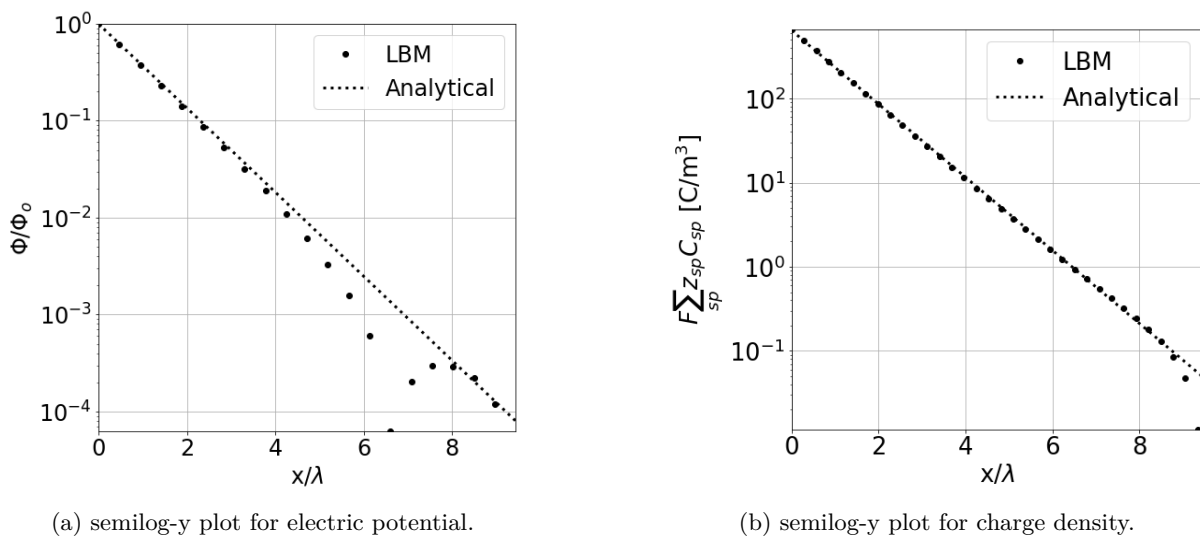


Figure 6.4: Comparison of analytical and LBM results for ion concentration on logarithmic scale.

To better study the agreement between the simulation and analytical results, the nature of the dis-

tributions are compared. The Debye-Hückel theory proposes that the distributions should follow an exponential decay. To validate that a similar trend is resulting from the simulation, a logarithmic plot is used to compare them. The exponential trend of the Debye-Hückel electric potential normalized by Φ_o is translated into a linear profile in the logarithmic plot. The normalized electric potential and charge density distribution are represented in Fig. (6.4a,6.4b). According to the Debye-Hückel theory, the difference between the local concentration and the bulk concentration follows an exponential nature. Replacing the electric potential in eq. (6.5) with eq. (6.4), gives,

$$C_{\text{sp}}(x) = C_{\text{sp},\infty} e^{\left(\frac{-z_{\text{sp}} F}{RT} \Phi_o e^{\left(\frac{-x}{\lambda} \right)} \right)}. \quad (6.6)$$

On expanding the outermost exponential operator in the above equation using Taylor's series and truncating the higher order terms (based on the Debye-Hückel approximation) gives

$$C_{\text{sp}}(x) = C_{\text{sp},\infty} \left[1 + \left(\frac{-z_{\text{sp}} F \Phi_o}{RT} \exp\left(\frac{-x}{\lambda} \right) \right) \right], \quad \forall \left| \frac{F \Phi}{RT} \right| \ll 1. \quad (6.7)$$

Rearranging the above equation,

$$\frac{C_{\text{sp}}(x) - C_{\text{sp},\infty}}{C_{\text{sp},\infty}} = \frac{-z_{\text{sp}} F \Phi_o}{RT} \exp\left(\frac{-x}{\lambda} \right). \quad (6.8)$$

The equation that is given by eq. (6.8) translated into a linear function on a logarithmic scale and the corresponding comparisons for positive and negative ionic species are shown in Fig. (6.5a,6.5b).

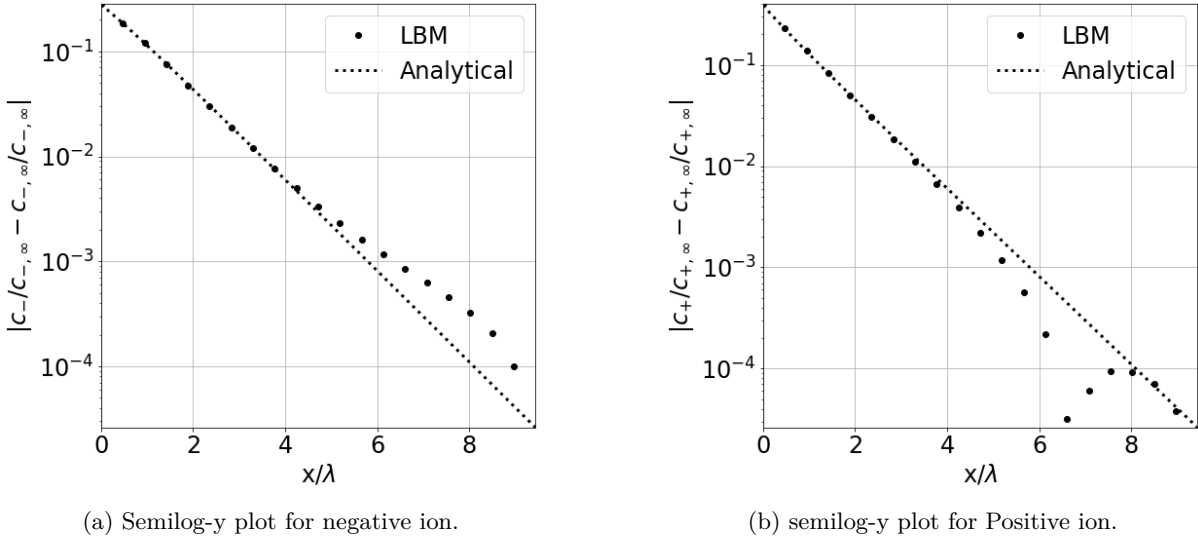


Figure 6.5: Comparison of analytical and LBM results for ion concentration on logarithmic scale.

From Fig. (6.5,6.4), there exists a good agreement in the nature of the distribution. Away from the electrode surface (approximately after 5λ), there is a deviation in the nature of the distribution. This is because the Debye-Hückel theory considers the domain to be infinitely long such that the concentration and potential profiles decay asymptotically towards their bulk value at an infinite distance. On the other hand, concentration and potential tend to the exact values at the bulk as they are forcefully imposed at the right boundary. Thus, the deviations far away from the left boundary are due to the finite size of the domain and the distribution is affected by the right boundary condition. The maximum relative error between the LBM and analytical results for electric potential, positive ion, and negative ion is 1.11%, 1.43%, and 0.45% respectively estimated using

$$RE_{\Phi} = \left| \frac{\Phi_{\text{LBM}} - \Phi_{\text{DH}}}{\Phi_o} \right| \times 100, \quad RE_{\pm} = \left| \frac{C_{\pm,\text{LBM}} - C_{\pm,\text{DH}}}{C_{\pm,\infty}} \right| \times 100. \quad (6.9)$$

Chapter 7

HER: Constant reaction rate

From the previous chapter, there exists a good agreement between the simulation and Debye-Hückel theory. So, the simulation methodology is extended to solve and understand the species transport phenomena in the hydrogen half-cell of the Alkaline water electrolyzer. Since this work considers a multi-component single-phase (aqueous) system and studies the species transport behavior along with the heterogeneous reaction, the local concentration of H_2 has been kept under solubility limit by using appropriate simulation conditions. The H_2 bubbles start to nucleate when the local H_2 concentration exceeds the solubility limit for the given electrolyte concentration, temperature, and pressure. The solubility limit of H_2 in KOH electrolyte at $T=298$ and 333 K and 1 bar pressure computed and validated against experimental data by Parsa [45] and is given in Fig. (7.1). Extrapolating the solubility for 0.001 mol/L KOH electrolyte and $T=353$ K from the solubility plot in figure (7.1), the maximum local concentration density of H_2 is approximately $C_{H_2,lt}=0.6 \times 10^{-3}$ mol/L= 0.6 mol/m³.

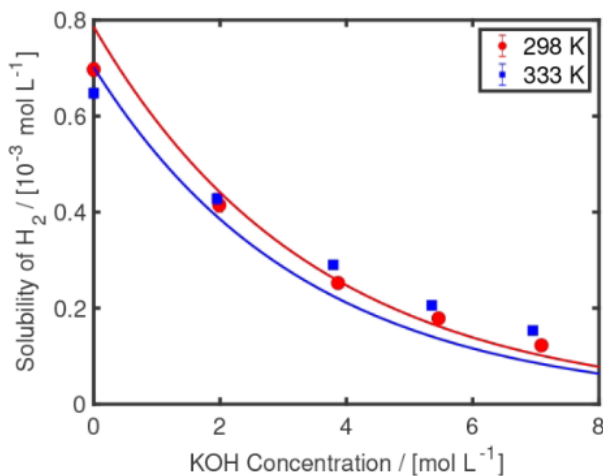


Figure 7.1: The solubility limit of H_2 depending on the molarity of the KOH solution at $T=298,353$ K [45].

In this chapter, the species flux based on a constant current density (fixed reaction rate) is used for the Nernst-Planck solver to understand the evolution of electric potential and species concentration density. Further more, the limitation of high electrode potential and the simulation procedure in that case are discussed. The species involved in the simulation are water (H_2O), hydrogen (H_2), hydroxide ion (OH^-) and potassium ion (K^+). The operating temperature is chosen to be 80 °C (353.15 K) and the corresponding transport properties are listed in the Table (2.2). A constant current density of magnitude 1000 A/m² (fixed reaction rate) is used to model the species flux at the electrode using the eq. (2.24) rather than determining the current density from the kinetics solver. The simulation with the reaction rate dictated by the kinetics solver is dealt with in the next chapter. One-molar potassium hydroxide solution is used as the electrolyte. The parameters of the species used for the simulation are listed in the Table (7.1) below. The species with negative, positive, and zero stoichiometric coefficients respectively denote the reacting, produced, and non-reacting species present in the hydrogen half-cell.

H ₂ O	H ₂	OH ⁻	K ⁺
Transport properties @ 80 °C [m ² /s]			
D _{H₂O}	D _{H₂}	D _{OH⁻}	D _{K⁺}
2.295 × 10 ⁻⁹	10 × 10 ⁻⁹	5.272 × 10 ⁻⁹	1.956 × 10 ⁻⁹
Stoichiometric coefficients			
S _{H₂O}	S _{H₂}	S _{OH⁻}	S _{K⁺}
-1	+1/2	+1	0
Valencies			
z _{H₂O}	z _{H₂}	z _{OH⁻}	z _{K⁺}
0	0	-1	+1
Bulk concentration [mol/m ³]			
C _{H₂O,∞}	C _{H₂,∞}	C _{OH⁻,∞}	C _{K⁺,∞}
55500	0.0001	1	1

Table 7.1: Species properties involved in hydrogen half-cell transport phenomena.

7.1 Low cathode potential

The thermal voltage ($\frac{RT}{F}$) is set as the magnitude of electric potential at the cathode and the simulation of species transport phenomena in the hydrogen half-cell is performed. The species flux at the cathode surface which is the heterogeneous source term for the Nernst-Planck solver is modeled using a constant current density of magnitude $|J|=1000$ A/m². The two-dimensional simulation representing a quasi one-dimensional case was performed using the D2Q5 lattice configuration and the results are discussed below. A domain of 0.1×0.05 μm in physical space is scaled to 100×50 lu in lattice space. The domain and the boundary conditions chosen for the simulation are given in Fig. (7.2). The simulation is initialized with the bulk concentration of the species and 0 V potential throughout the domain.

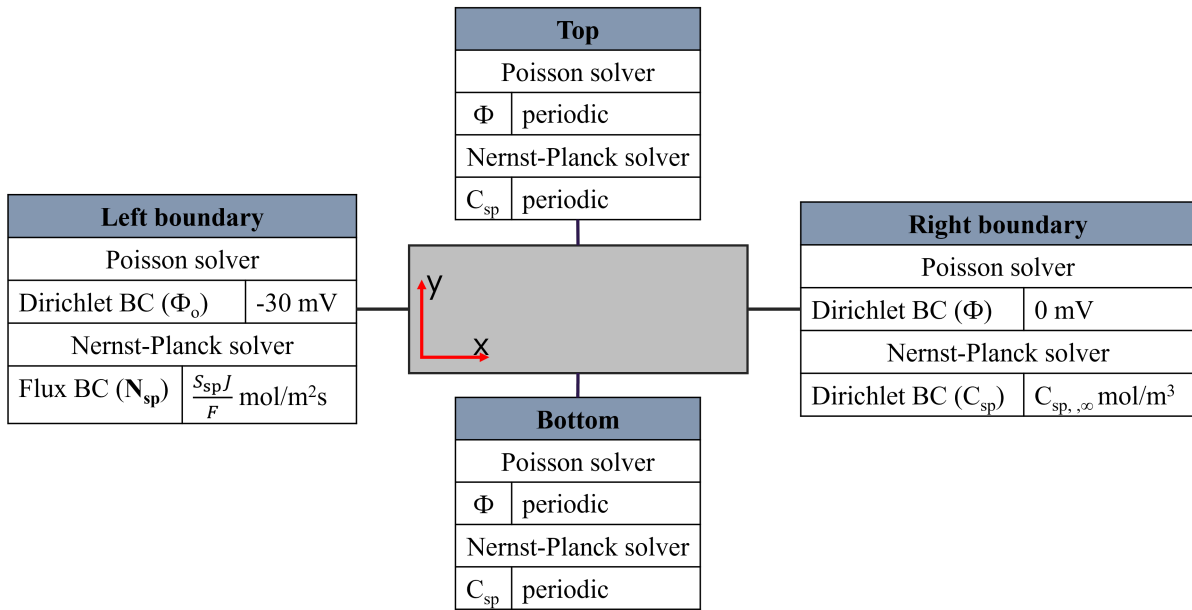


Figure 7.2: Domain for simulating species transport phenomena in hydrogen half-cell.

7.1.1 Electric field and potential

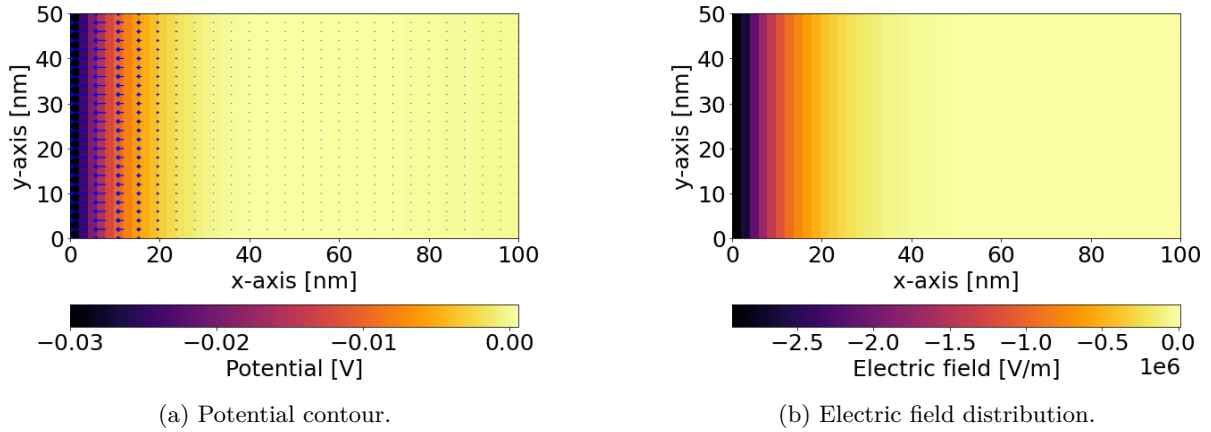


Figure 7.3: (a) Electric potential with electric field quivers, (b) Electric field at $t=2 \mu\text{s}$ for $\Phi_o=-30 \text{ mV}$, $|J|=1000 \text{ A/m}^2$.

The electric potential and electric field distribution in the domain at time instance $t=2.0 \mu\text{s}$ is shown in Fig. (7.3). To understand the evolution of the electric potential and field profiles, the distribution along the x-axis at different time instances are compared in Fig. (7.4). The slope of the electric potential in the electric double layer ($x/\lambda = 1$) increases with time. This evolution pattern is due to the increased accumulation of charge in the double layer. Far away from the EDL ($x/\lambda > 5$), the slope of electric potential decreases with time due to the relatively lower charge density away from the EDL. From the plot for the electric field, there is a massive drop in the magnitude within EDL and then the magnitude smoothens to a uniform value outside the EDL. At a higher evolution time of $t=2.0 \mu\text{s}$, the electric field far away from the EDL converges to zero.

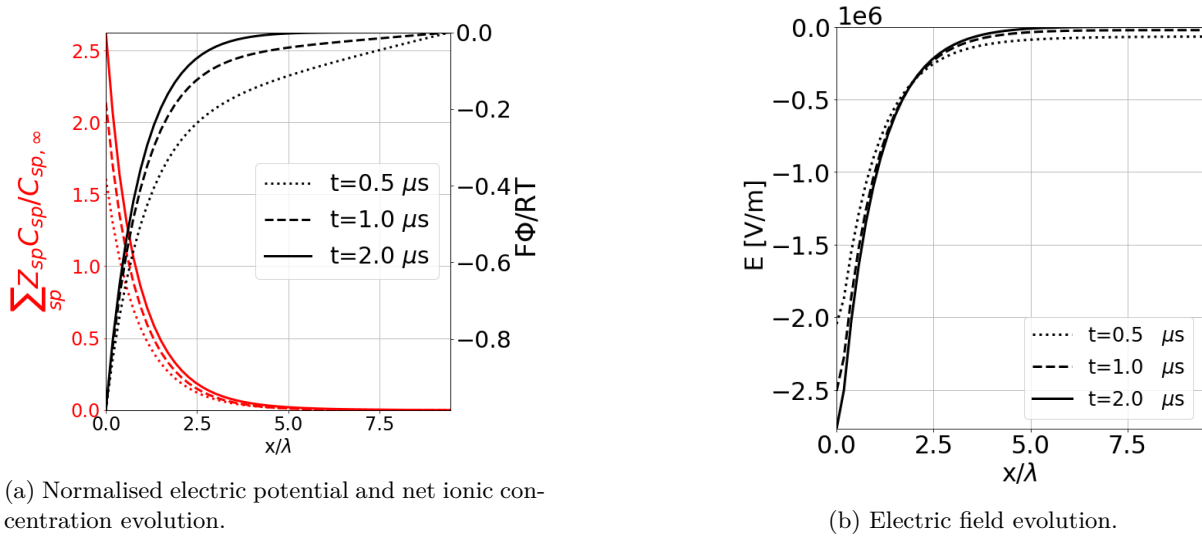


Figure 7.4: (a) Electric potential and charge density evolution, (b) Electric field evolution for $\Phi_o=-30 \text{ mV}$, $|J|=1000 \text{ A/m}^2$.

7.1.2 Species concentration

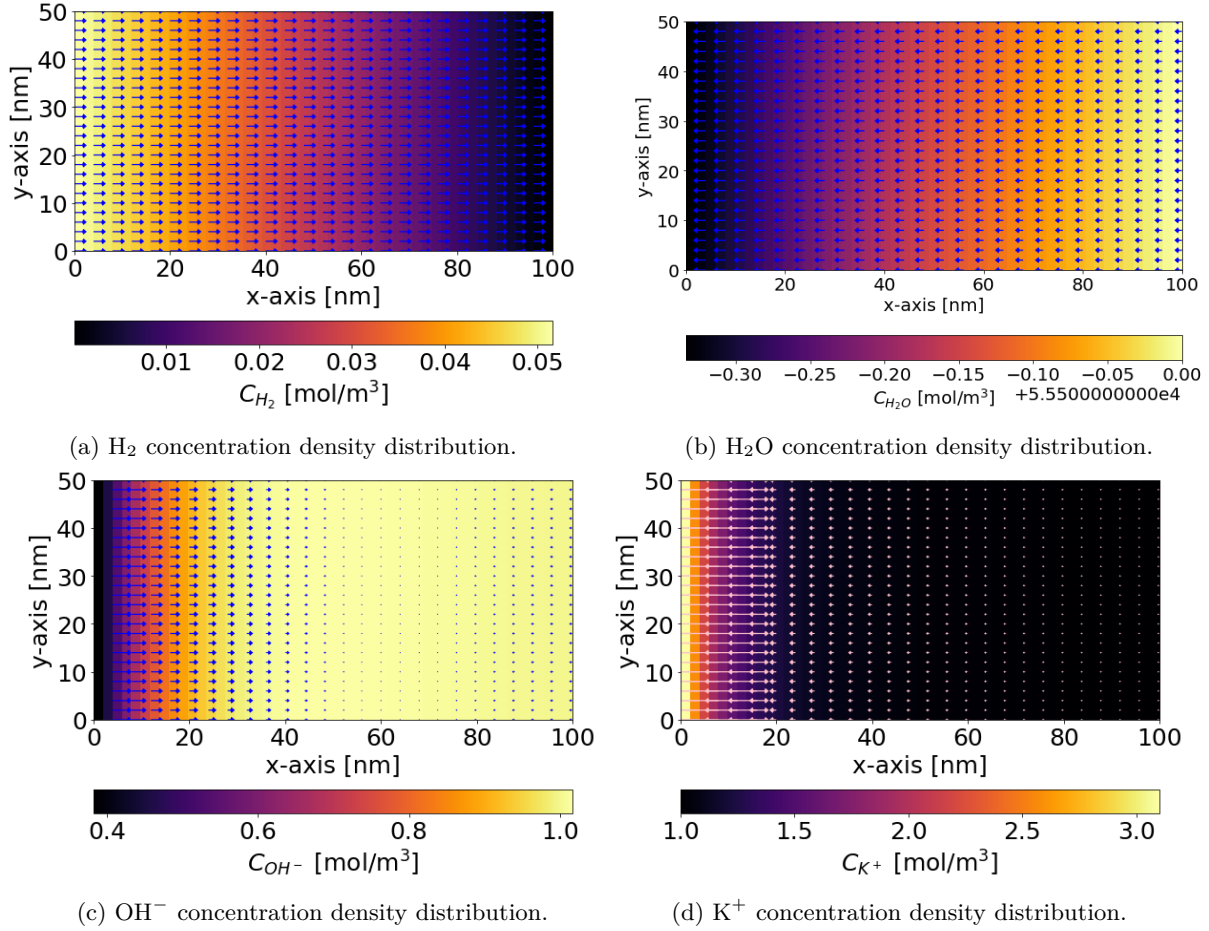
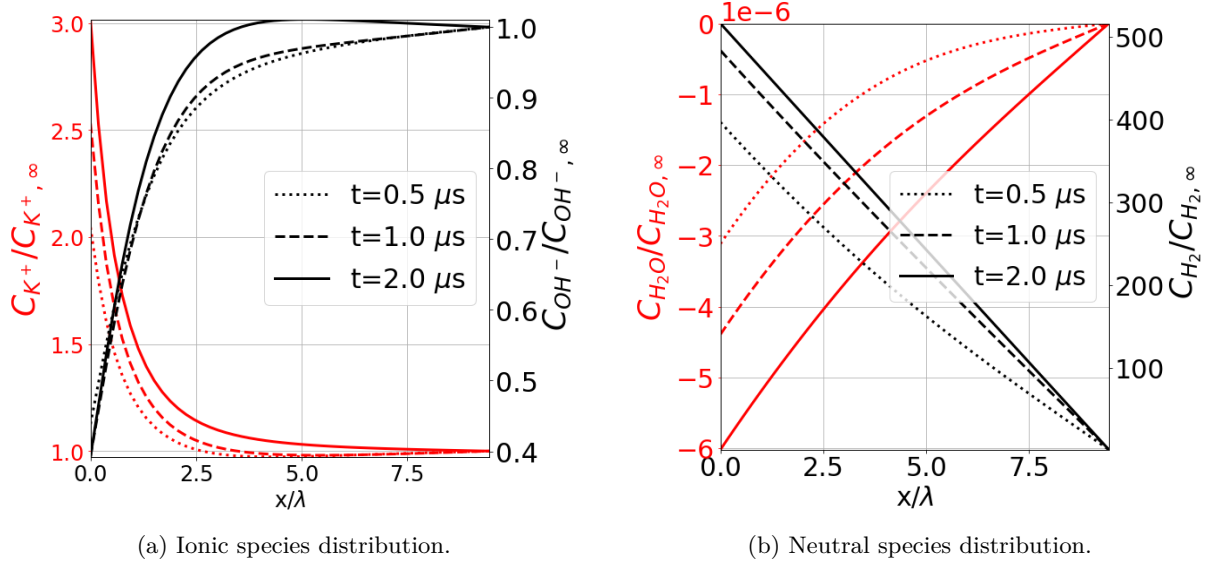
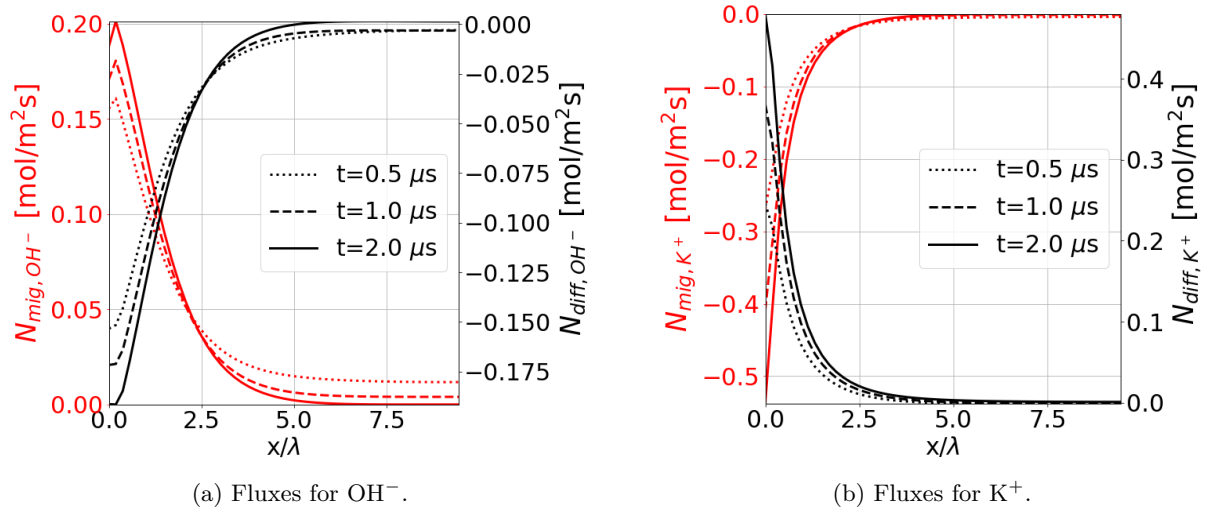


Figure 7.5: Concentration density of neutral and ionic species and vector plot representing net flux at $t=2 \mu\text{s}$ for $\Phi_o=-30 \text{ mV}$, $|J|=1000 \text{ A/m}^2$.

The concentration density distribution of all the species in the domain along with the quiver representation of their net flux at time instance $t=2 \mu\text{s}$ is represented in Fig. (7.5). The concentration density normalized using the respective bulk concentrations is plotted at different time instances in Fig. (7.6). For ionic species, the slope of the concentration in the EDL is higher compared to that outside the EDL. The evolution plot (Fig. (7.7a)) of K^+ indicates that the K^+ ions are attracted towards the cathode resulting in higher concentration near the cathode. This accumulation of K^+ ion screens the negative cathode potential from the bulk of the electrolyte leading to a higher electric field in the EDL. From the flux comparisons of ions in Fig. (7.7), there is a relatively large magnitude of the migrating flux in the EDL, and the diffusive flux of these ions tries to balance the migrating flux resulting in high concentration gradient in the EDL.

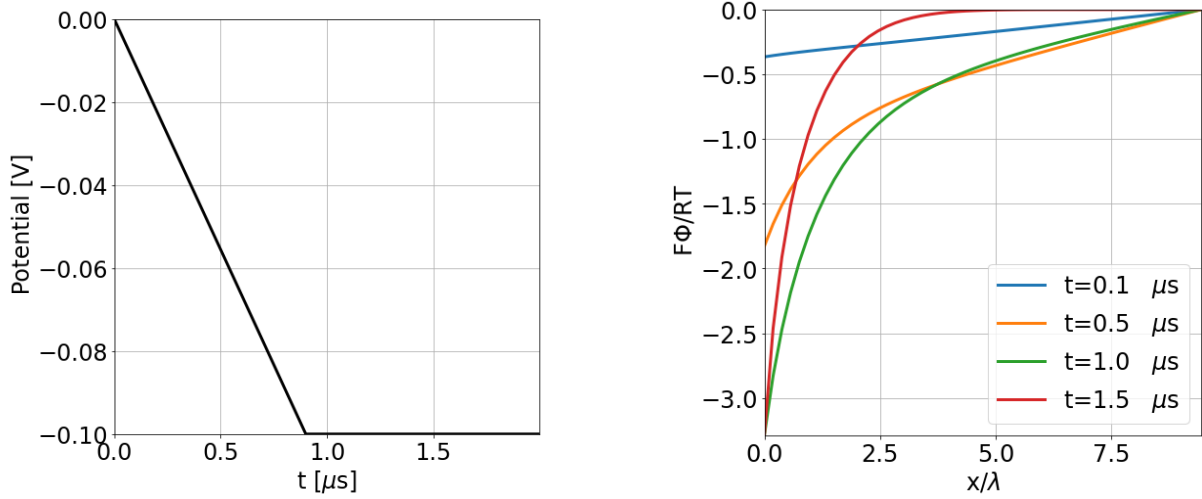

 Figure 7.6: Species concentration evolution for $\Phi_o = -30$ mV, $|J| = 1000$ A/m².

 Figure 7.7: Ionic species flux evolution for $\Phi_o = -30$ mV, $|J| = 1000$ A/m².

H₂ is produced at the boundary and diffuses into the bulk of the domain. On the other hand, H₂O is consumed at the cathode, resulting in diffusion of concentration density from the bulk towards the cathode.

7.2 High cathode potential

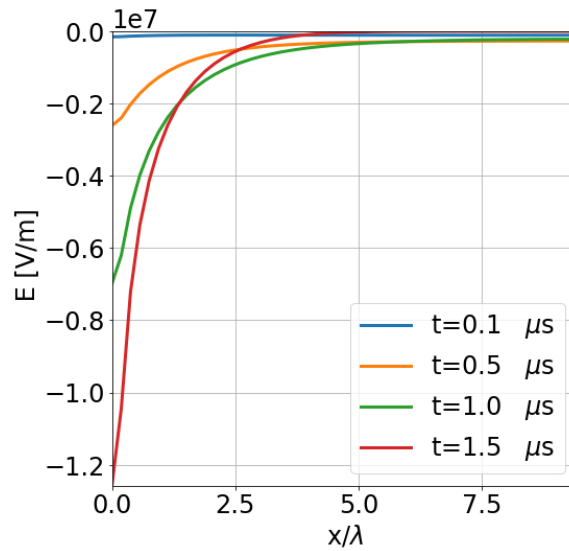
For simulations involving very high potential, the magnitude of the potential is ramped up with time. This procedure is adapted to avoid the instabilities and shock effects that result from directly applying a very high potential at the boundary. Without a gradual increase in potential, ions, and charges might experience shock effects, where they suddenly move very fast in response to the abrupt change in the electric field. In the scope of LBM, the stability of the system also depends on the magnitude of the migrating velocity in lattice space as discussed in Chapter 2. A rapid increase of potential will result in very high flux forcing the species to move with a migrating velocity larger than that required for stability. Besides, gradually ramping up the potential mimics the real-world process more accurately, where potential changes are often applied gradually. Neglecting this process reduces the physical realism of the simulation.

The domain chosen for the study is similar to that used for the low cathode potential simulation but with a cathode potential of $\Phi_o = -0.1$ V which is approximately three times the thermal potential. The cathode potential is ramped from 0 V to -0.1 V for 0.9 μ s, then the potential is set to be steady at -0.1 V for the rest of the simulation time. The cathode potential trend with respect to time is shown in Fig. (7.8a).



(a) Cathode potential ramp-up with time.

(b) Normalised electric potential evolution.



(c) Electric field evolution.

Figure 7.8: (a) Φ_o ramping with time (b) Electric potential evolution, (c) Electric field evolution for $\Phi_o = -0.1$ V, $|J| = 1000$ A/m².

The electric potential and electric field profiles at different time steps are given in Fig. (7.8). The slope of the electric potential in the EDL gradually increases due to the increasing accumulation of charge density towards the cathode along with the temporal ramping of the cathode potential. After 1.0 μ s, the rise in gradient is only due to the increasing charge density towards the cathode as the cathode potential is set to a steady value. From Fig. (7.8c), the magnitude of the electric field is uniform far away from the EDL and it evolves to zero with time in the bulk of the domain. Hence, there will be a temporal decrease in the influence of the electric field on the ionic species at the bulk region.

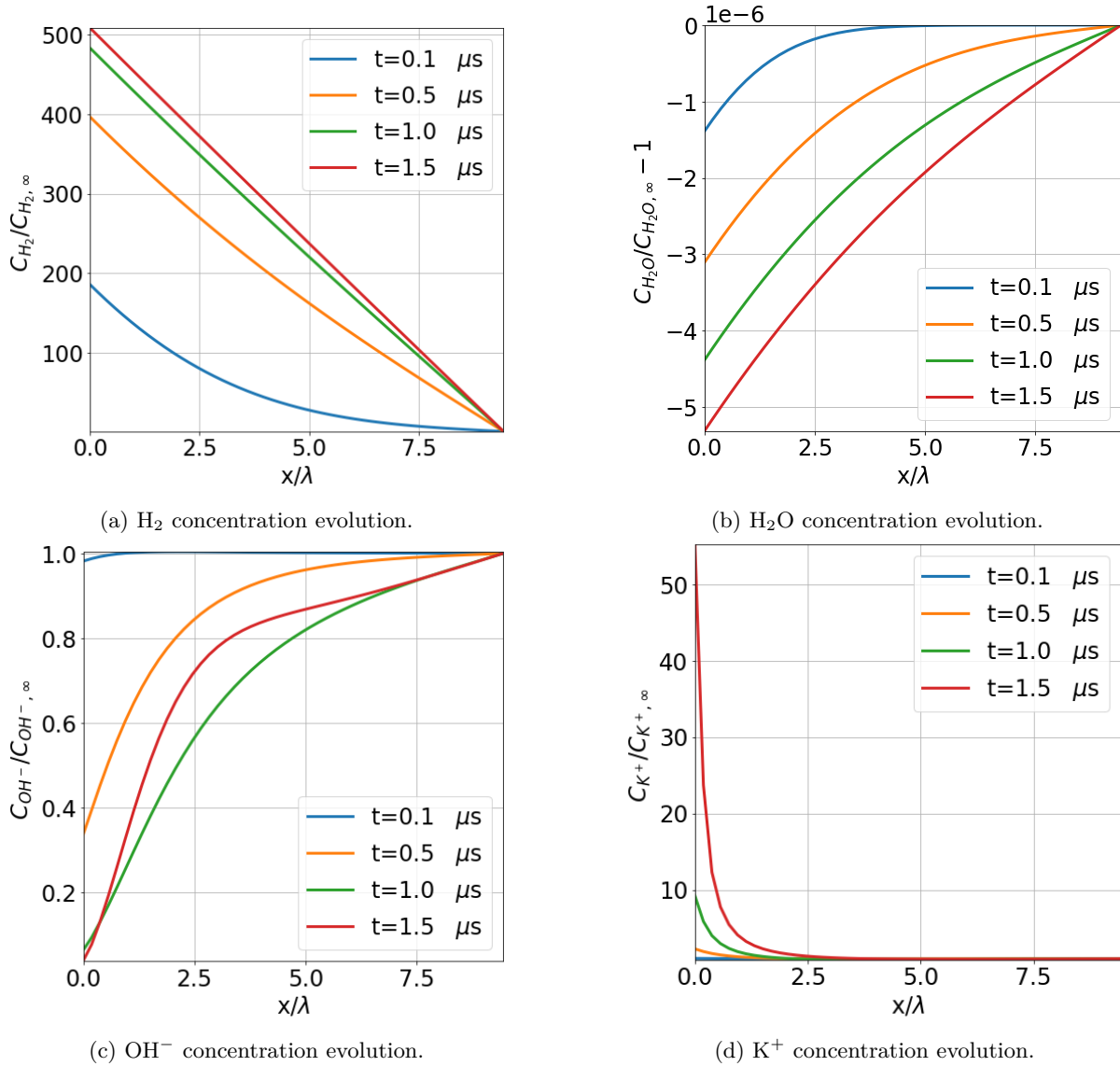


Figure 7.9: Species concentration evolution for $\Phi_o = -0.1$ V, $|J| = 1000$ A/m².

The concentration density of the neutral and ionic species are shown in Fig. (7.9). The neutral species distributions are identical to that from the low potential simulation as they are not influenced by the electric field considering the fixed reaction rate of $\mathbf{J} = 1000$ A/m². From the concentration density evolution of OH^- , the magnitude decreases at the cathode due to the migrating of these OH^- ions. At time instances $t = 0.1, 0.5, 1.0$ μs , the OH^- is influenced by the electric field both in the EDL and in the bulk region. This results in reduced concentration at the bulk as they are migrated to the right boundary. At $t = 1.5$ μs , the produced OH^- at the cathode boundary is moved away from the electrode across the EDL and stays at the diffusion region between the EDL and bulk. This is due to the electric field at the bulk evolving to a uniform 0 V/m resulting in no migrating flux of OH^- ions. At the same time, the electric field across the EDL increases resulting in enhanced migrating flux of OH^- transporting these negative ions out of the EDL. The flux plots of OH^- also indicate that migrating flux in the bulk decreases with time tending to zero at $t = 1.5$ μs . Comparing the concentration plots for K^+ and OH^- , the local charge density of the electrolyte is mainly dependent on the concentration density of K^+ at higher evolution times. This is valid at high cathode potential because the migrating flux of K^+ and OH^- (towards or away from the cathode) is higher in EDL resulting in a very high magnitude of K^+ concentration and a very low magnitude of OH^- concentration.

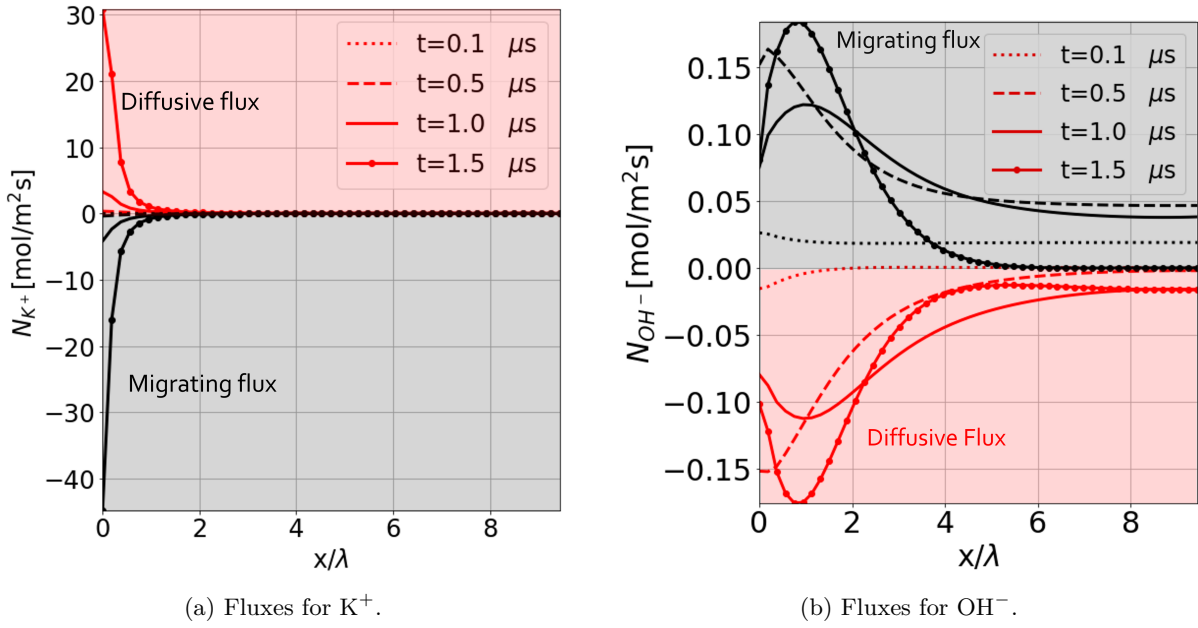


Figure 7.10: Migrating and diffusive flux evolution of ionic species for $\Phi_o = -0.1 \text{ V}$, $|J| = 1000 \text{ A/m}^2$.

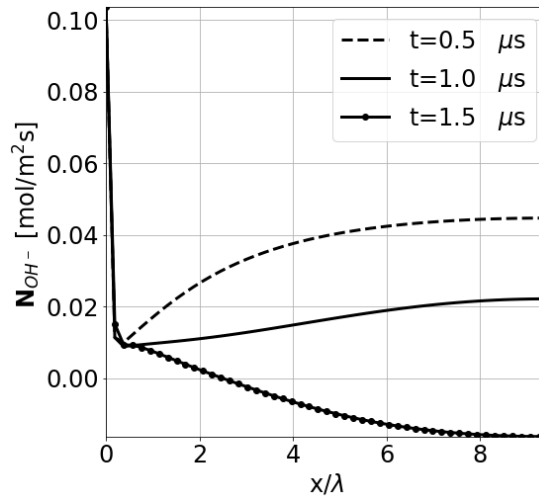


Figure 7.11: Total flux evolution for OH^-

In the classical Poisson Nernst-Planck model for the migration-diffusion problem, the steric effects due to the finite size of solution species, are usually neglected. As a result, unphysically high ionic concentrations are typically predicted in the EDL region for high electrode potentials. There are models such as the size-modified Poisson Nernst-Planck model that consider the finite size of the species thereby restricting the abnormal accumulation of species in the EDL [46]. This approach used to overcome this issue along with the added kinetics solver to dictate the rate of the reaction is dealt with in the next chapter.

Chapter 8

HER: species transport with kinetics

The Poisson Nernst-Planck model for migration-diffusion of species with the reaction rate dictated by the Butler-Volmer kinetics model is simulated for the hydrogen half-cell and the results are discussed in this chapter. For the HER, the magnitude of the cathode potential should be greater than the equilibrium potential for the given temperature and concentration. As a rough estimate, the magnitude of the cathode potential has to be greater than 0.828V. The default Poisson-Nernst-Planck with such high cathode potential can result in steric effects causing abnormal ionic species accumulating in the EDL.

To address this issue, it is assumed that the order of the electric potential at the OHP is in mV. The layer between the electrode surface and the OHP is not considered, and the diffuse layer of the EDL is considered to be next to the electrode surface. Thus the magnitude of the electric potential used as a boundary condition for the Poisson solver is taken at the OHP in EDL [47]. Yet to determine the overpotential, the actual electrode potential which is in the order of volts is used to induce the reaction at the reacting boundary. The electric potential at the OHP is denoted by Φ_{OHP} and that at the electrode surface is denoted by Φ_s . For simplicity, it is considered that the Φ_{OHP} is independent of Φ_s . This consideration is valid because the exponent scaling with H_2O in the Butler-Volmer equation is more dominant than the exponent scaling with the OH^- . The simulation with uniform and spatially varying electrode potential was performed and the results are discussed below.

The two-dimensional domain for the simulation is represented in Fig. (7.2). The current density to compute the species flux at the cathode based on the HER is evaluated by the reaction kinetics solver. The reference values for the kinetics solver are given in Table (2.1). The domain size of $0.2 \times 0.05 \mu m$ in physical space is chosen for this study and is scaled to 200×50 lu in the lattice space. The boundary condition definitions at the left boundary for each solver are given in the Table (8.1) below.

Left boundary		
Poisson solver	Reaction kinetics solver	Nernst-Planck solver
Dirichlet BC	Dirichlet BC	Newmann flux BC
OHP potential (Φ_{OHP})	-50 mV	Electrode surface potential (Φ_s)
	[-0.75,-0.8,-0.85,-0.9] V	Species flux $\frac{s_{sp}J}{F}$ mol/m ² s

Table 8.1: Boundary condition definition at the left boundary for Poisson-Nernst-Planck model with reaction kinetics.

8.1 Uniform electrode potential

A uniform electric potential is applied on the left boundary and simulated for different electrode potentials to vary the rate of the reaction. The temporal ramping is applied to both the electrode and OHP potential. The simulation results for the electrode potential of $\Phi_s = -0.8$ V are discussed in this section.

The evolution of the overpotential and Nernst potential that is dependent on the electrode potential (Φ_s), and the pH of the electrolyte is shown in the Fig. (A.6a). The resulting evolution of current density and species reaction flux (eq.(2.24)) is shown in Fig., (A.6b). In the time band between $t \in [0, 0.5] \mu s$,

there is no reaction occurring (the grey area in Fig. (A.6)) because the electrode potential has not ramped up enough to overcome the Nernst-corrected equilibrium potential for HER. The minimum energy requirement corresponding to the operating condition for HER is not supplied at the cathode end in this time window and hence there is no reaction happening. The overpotential and current density reached a steady value of magnitude $|\eta| = 0.2879$ V and $|\mathbf{J}| = 459.68$ A/m².

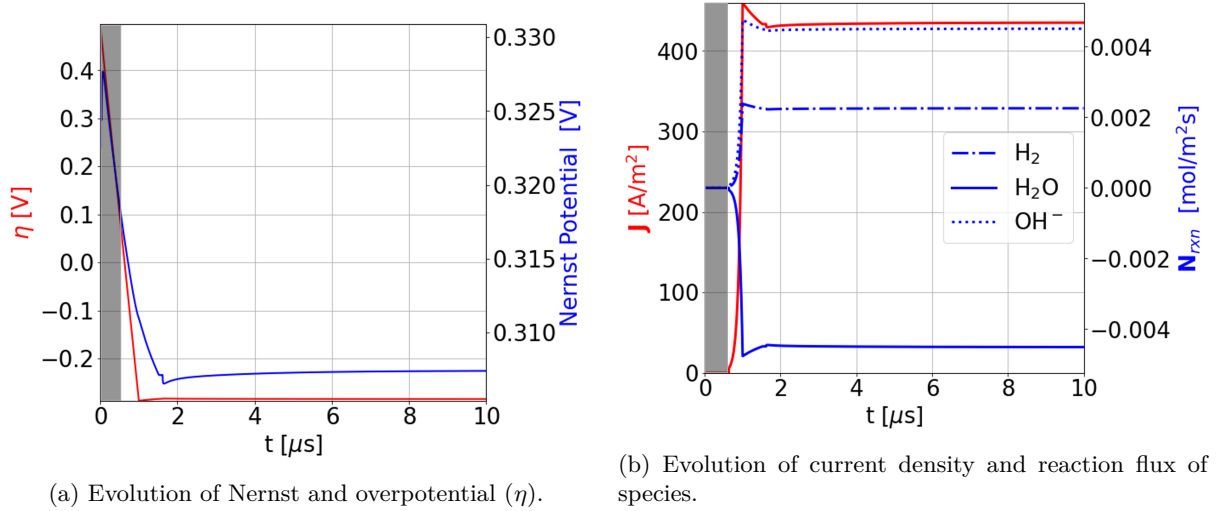


Figure 8.1: Evolution of the over and Nernst potential, current density and species reaction flux at reacting boundary for $\Phi_s = -0.8$ V and $\Phi_{\text{OHP}} = -50$ mV

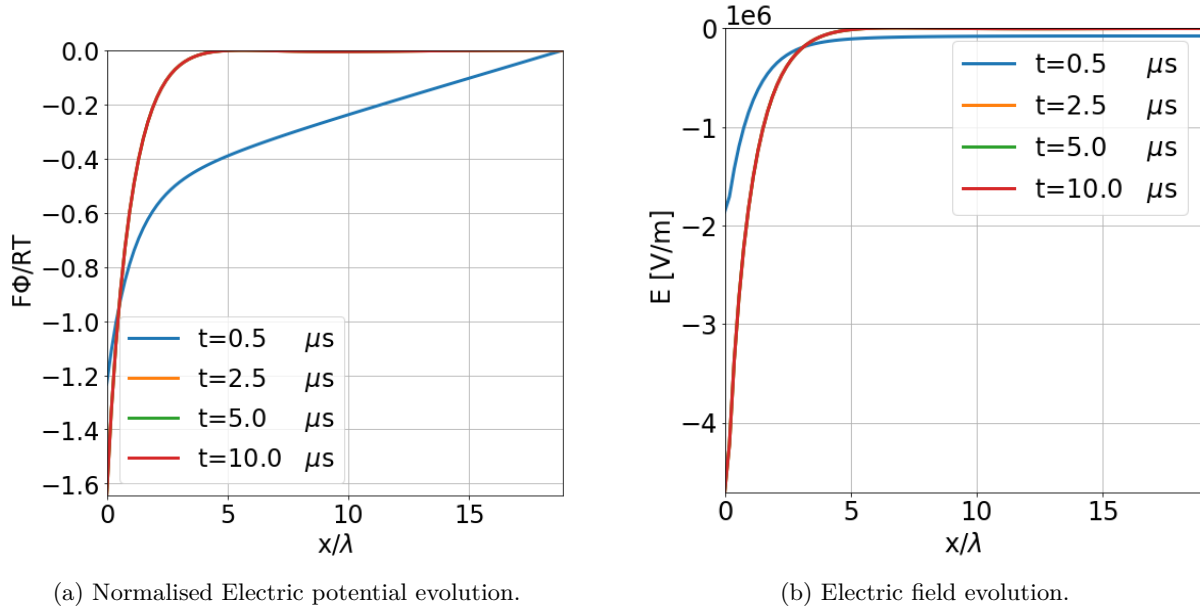


Figure 8.2: Electric potential and electric field evolution for $\Phi_s = -0.8$ V and $\Phi_{\text{OHP}} = -50$ mV.

The electric potential and electric field distribution and their evolution are shown in Fig. (8.2). The concentration density distribution of the species from the OHP for electrode potential of $\Phi_o = -0.8$ V and OHP potential of $\Phi_d = -50$ mV in the hydrogen half-cell with the HER occurring at the left boundary ($x=0$) are shown in Fig. (A.5). The neutral species show a flat profile in concentration density from $t=0$ μs to $t=0.5$ μs because the ramping up electrode potential did not overcome the minimum energy barrier in that time band. For ionic species, the profile evolves in the non-reaction time period due to the influence of the migrating fluxes. The migrating and diffusive flux profiles of the ionic species are given in Fig. (8.4). The evolution profiles for other electrode potentials are given in the Appendix A.

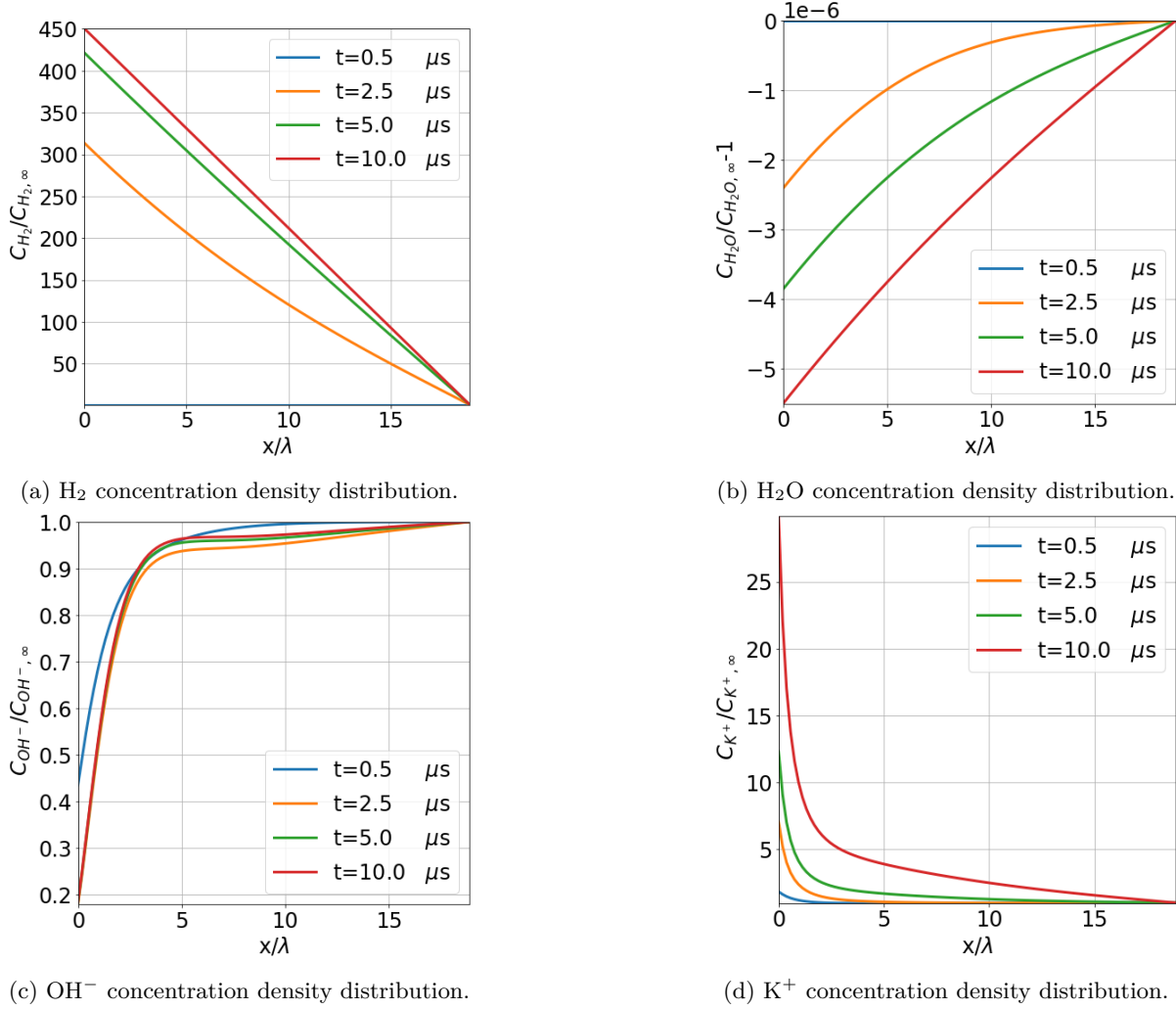


Figure 8.3: Species concentration evolution for $\Phi_s = -0.8$ V and $\Phi_{OHP} = -50$ mV.

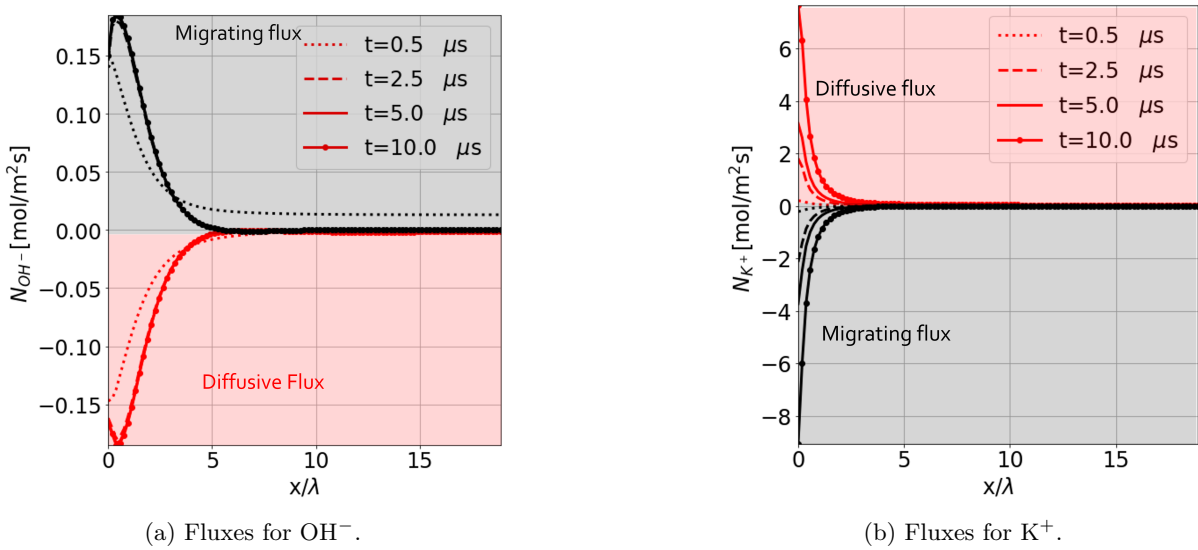


Figure 8.4: Migrating and diffusive flux evolution of ionic species for $\Phi_s = -0.8$ V and $\Phi_{OHP} = -50$ mV.

8.1.1 Influence of electrode potential Φ_o

The simulation results for different electrode potentials are compared to understand their influence on the reacting and produced species. As aforementioned the electrode potential (Φ_o) is used by the reaction kinetics solver to determine the overpotential (η), which is in turn used to determine the kinetic current density (\mathbf{J}). The overpotential increases linearly with the electrode potential for the same electrolyte concentration and temperature as shown in Fig. (8.5a). The hydrogen profile at $t=10.0 \mu\text{s}$ for different overpotential is represented in Fig. (8.5). The concentration density of H_2 at the left boundary increases with an increase in overpotential because the magnitude of reaction source flux at the left boundary is related to the current density which is directly related to overpotential.

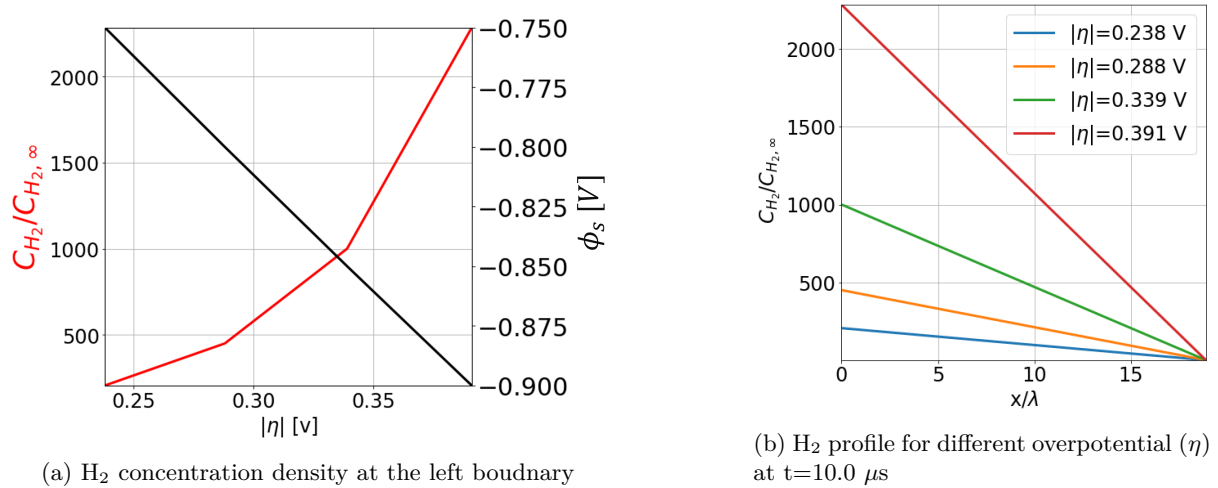


Figure 8.5: H_2 stats for different overpotential (η)

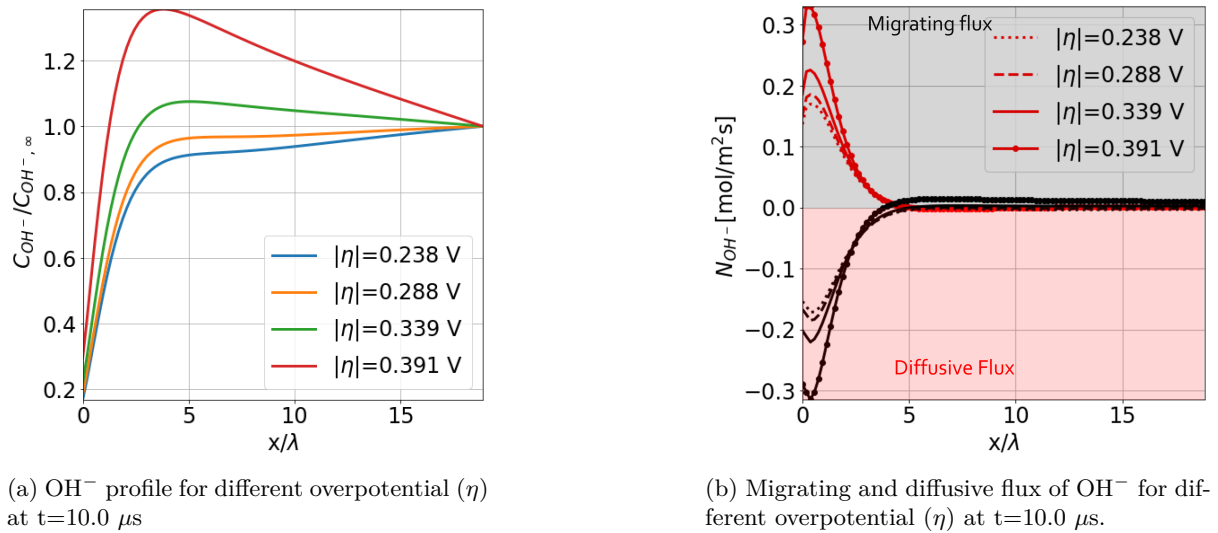


Figure 8.6: OH^- statistics for different overpotential (η)

The concentration density and flux profiles of OH^- for different overpotential at $t=10.0 \mu\text{s}$ are compared in Fig. (8.6). At the given time instance the electric field away from the EDL is negligible compared to that in the EDL. Thus, the migrating flux responsible for transporting these negative ions towards the bulk (right boundary) is negligible relative to that in the EDL. By increasing the overpotential, the magnitude of source flux at the reacting site (left boundary) for producing OH^- increases, resulting in enhanced migrating flux in the EDL because a large amount of negative ions are transported away from the reacting site. Thus ions that are migrated away from the reacting site due to the high electric field in EDL stall away from the EDL where the electric field is negligible. This is the reason for the 'hump' seen in the concentration profiles of OH^- in Fig. (8.6a). The negative gradient of concentration density

induces a positive diffusive flux for OH^- to move the ions towards the bulk. This is indicated by the inversion of diffusive fluxes from negative to positive values for $|\eta|=0.339, 0.391$ V in Fig. (8.6).

8.2 Spatially varying boundary condition

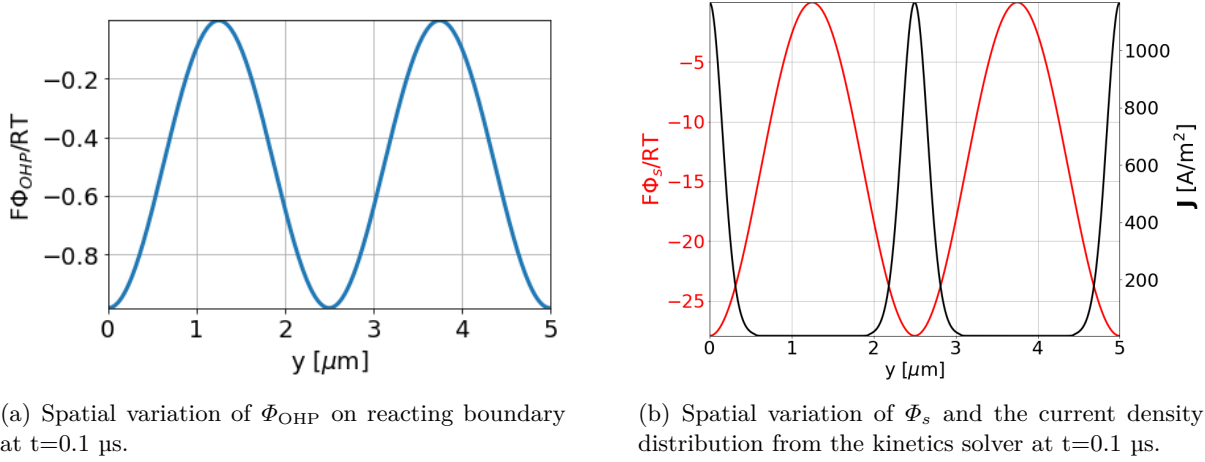


Figure 8.7: sinusoidal spatial variation imposed on the potentials at the reacting site and the resulting current density distribution from the kinetics solver at $t=0.1$ μs .

In reality, the nucleating bubbles screen the electrode-electrolyte interface and hence the reaction sites are not uniform. To replicate this system to some extent, a sinusoidal spatial variation of electrode potential (Φ_s) and OHP potential (Φ_{OHP}) is imposed on the reacting boundary. The sinusoidal wave used for this purpose is shown below in Fig. (8.7a). A domain size in physical space is 1×5 μm which scales to 250×1250 lattice units in lattice space. The dimension along the secondary direction (y -axis) is greater than the primary direction (x -axis) to ensure that there is a very smooth transition in potential along the secondary direction due to the applied sinusoidal variation. The total time of the simulation was taken to be 0.1 μs . The spatial variation has a maximum electrode potential $\Phi_o = -0.85\text{V}$ and $\Phi_d = -30$ mV. Thus, from the Fig. (8.7), the crests are the sites with the maximum reaction rate and the reaction does not occur at the trough sites as the electrode potential at those regions is lower than the magnitude of equilibrium potential for the local pOH.

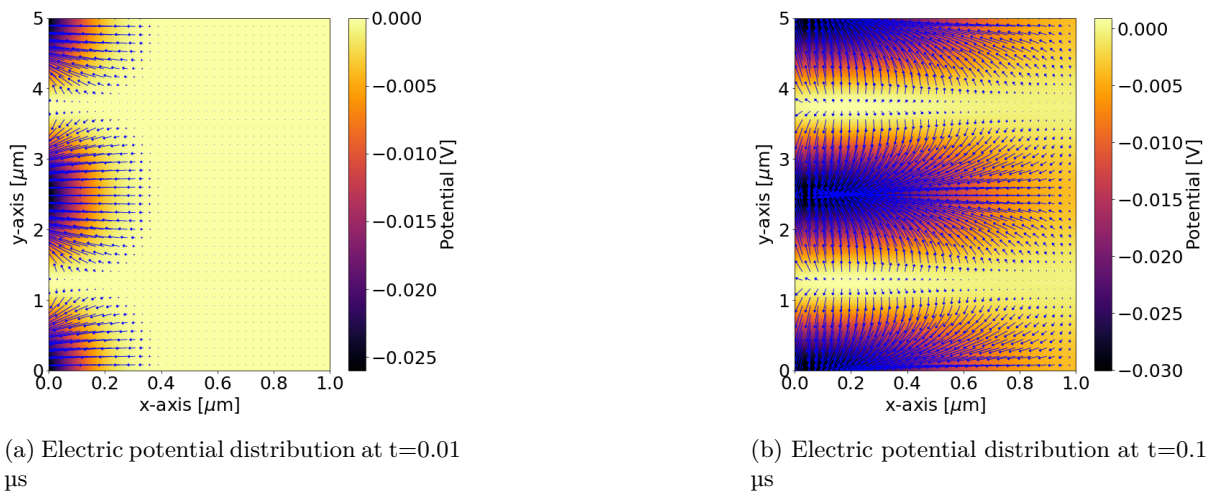


Figure 8.8: Electric potential distribution between the OHP and the right boundary (bulk) and the vector plot for electric field distribution at $t=0.01$ and 0.1 μs .

The right boundary is set to be zero potential gradient in the x -axis to let the boundary value evolve based on the solution in the domain. The evolution of the electric potential distribution from the Poisson

solver is shown in Fig. (8.8). The H_2 produced at local patches on the left boundary where there are non-zero current densities is shown in Fig. (8.9). The vectors indicate the diffusive flux of H_2 that transports the produced hydrogen away from the reaction site in both primary and secondary directions. The similar transport behavior of H_2O is shown in Fig. (8.10). The maximum local H_2 concentration is 0.03 mol/m^3 , which is lower than the solubility limit and hence it is in the aqueous state.

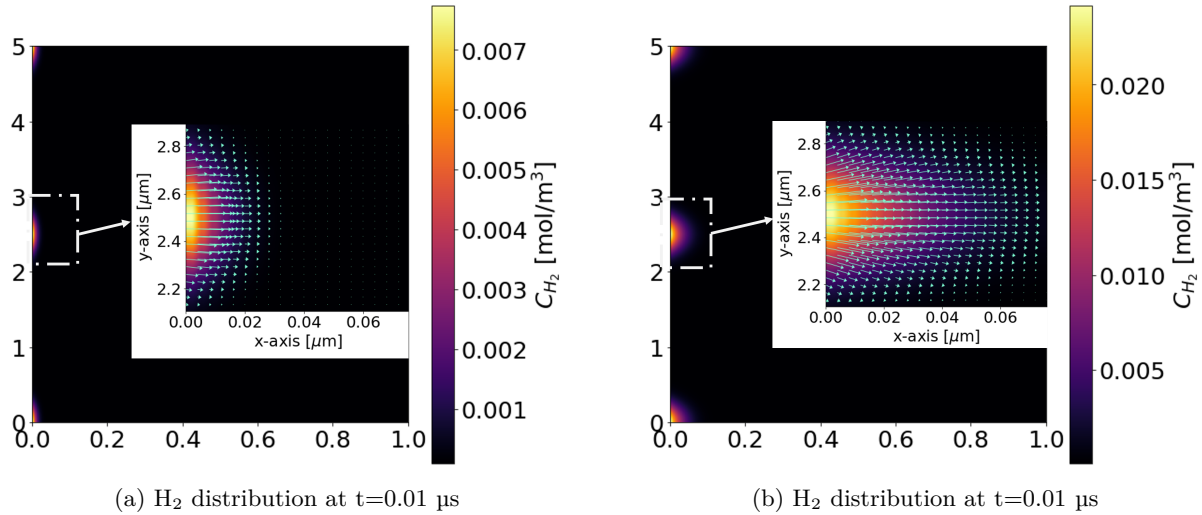


Figure 8.9: Local concentration density of H_2 and the vector plot for flux at $t=0.01$ and $0.1 \mu s$

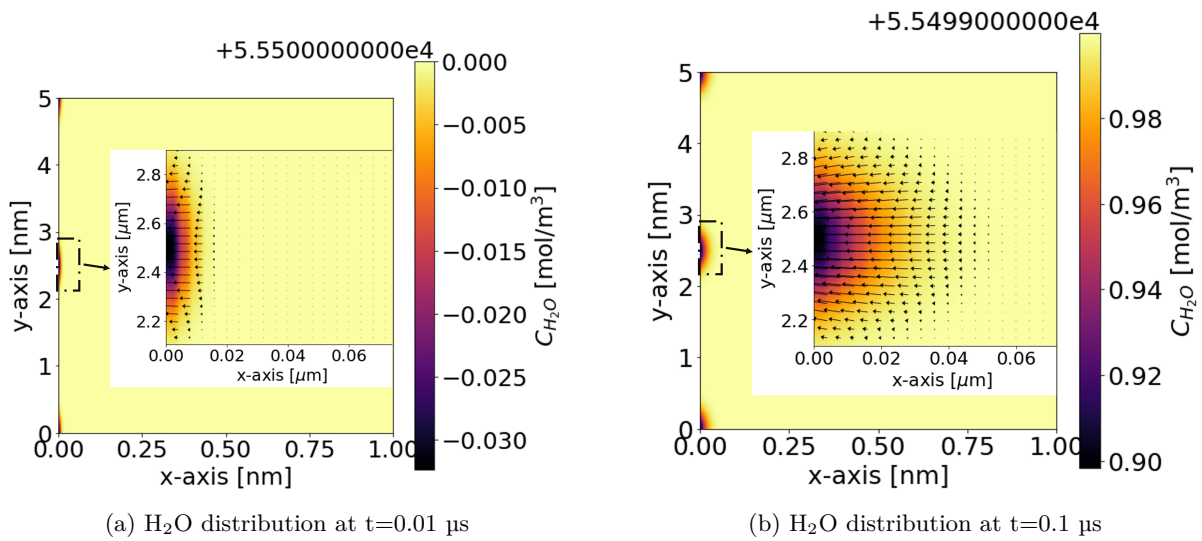


Figure 8.10: Local concentration density of H_2O and the vector plot for flux at $t=0.01$ and $0.1 \mu s$

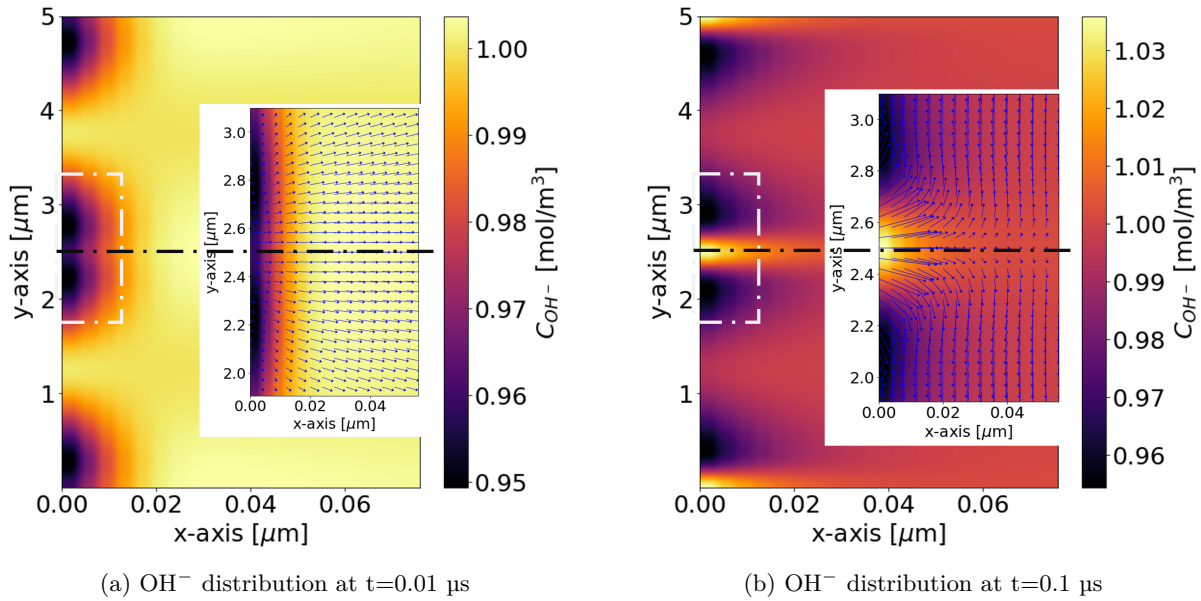


Figure 8.11: Local concentration density of OH^- and the vector plot for flux at $t=0.01$ and $0.1 \mu\text{s}$

The OH^- and K^+ local concentration density distribution along with their fluxes at regions of interest are shown in Fig. (8.11,8.12). For better visualization, the clip between $x=0$ and $x=0.07 \mu\text{m}$ has been represented. In the case of OH^- , while there are low-concentration zones adjacent to the center axis (indicated in the black axial line), a relatively high concentration exists along the axis. The sinusoidal spatial variation results in an electric field in the secondary direction (directed towards the center line Fig. (8.8)) migrating the negative ions away from the center line. The negative ions at the center line are not migrated in the secondary direction due to zero electric potential at the crest of the spatial variation. Thus, at the adjacent zones to the center axis, the OH^- ions produced at the local reacting sites are transported away by the migrating flux in both primary and secondary directions resulting in a low concentration zone. But along the center line, the produced OH^- ions are migrated only in the primary direction resulting in a relatively high concentration density at the center axis close to the reacting site. At $t=0.1 \mu\text{s}$, the potential gradient along the center axis tends to a low constant value (electric field vectors in Fig. (8.8b)) which further hinders the migration of OH^- away from the reacting site. This results in a higher accumulation of negative ions and the diffusive flux transporting the ions in the primary direction (x-axis).

In the case of K^+ ions, the spatial variation results in the migration of positive ions towards the center line while those along the center axis are not migrated in the secondary direction due to zero electric field in that direction. At the zones on either side of the center line, the positive ions are migrated towards the zone by both the secondary and primary electric fields, while the positive ions along the center axis are migrated only by the electric field along the primary direction. This results in a high accumulation of positive ions adjacent to the center line. At $t=0.1 \mu\text{s}$, there is an inversion in the direction of the flux in the primary direction along the center axis. Close to the reaction site along the center axis, the electric field component along the primary axis (x-axis) is zero (vector plots from the Fig. (8.8b)) resulting in the diffusive flux transporting the positive ions away from the left boundary due to the negative concentration gradient from the electrode surface towards the bulk.

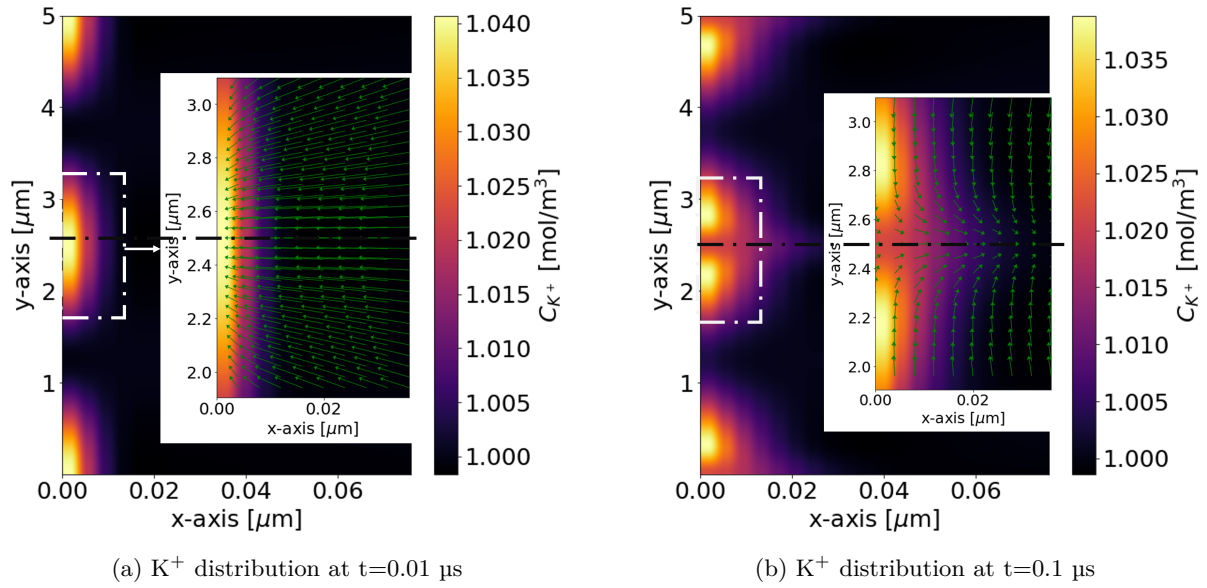


Figure 8.12: Local concentration density of K^+ and the vector plot for flux at $t=0.01$ and $0.1 \mu s$.

Thus, the transport behavior of the species due to the interplay between the fluxes in primary and secondary directions for the given case is studied. The distribution profiles for other time instances are given in the Appendix B.

Chapter 9

Heterogeneous reaction on a catalyst particle

In reality, electrodes used for AWE are porous in order to increase the surface area of activation sites. On resolving the porous electrode, it is seen that there is a random arrangement of catalyst particles with irregular geometry. The Migration-diffusion of the species with heterogeneous reactions occurring on the surface of the deformed boundary is interesting to study. Thus, a single catalyst particle with a simplified circular geometry is chosen as shown in Fig. (9.1).

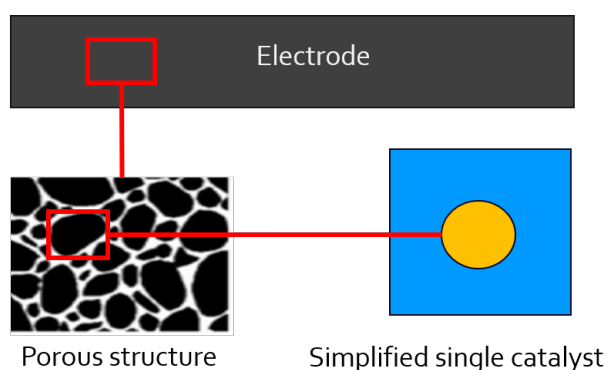


Figure 9.1: Schematic view of the porous electrode, the magnified porous structure, and simplified geometry of a catalyst particle.

For the simulation of the species transport in hydrogen half cell with the heterogeneous reaction occurring at the electrode-electrolyte interface, the geometry setup and the boundary conditions are given in Fig. (9.2). The total domain length is $0.1 \times 0.1 \mu\text{m}$. The disc of diameter 40 nm with center at $x = y = 0.05 \mu\text{m}$ is used to represent the simplified catalyst particle in the electrode. Thus, the region of interest is the area around the disc within the domain which is represented by the 'blue' shade in Fig. (9.2). In the region represented by the 'orange' shade, no physics of interest occurs and hence will be treated as a dead zone.

The electrode-electrolyte interface is the reacting site with electrode surface potential $\Phi_s = -0.85 \text{ V}$. The OHP potential around the catalyst is chosen to be $\Phi_{\text{OHP}} = -20 \text{ mV}$. The source/sink flux boundary condition is used by the Nernst-Planck solver at the electrode-electrolyte interface. The other boundaries in the domain are modeled using the statistics at the bulk of the electrolyte. Hence, these boundaries are set up with zero potential and bulk species concentration.

For the simulation purpose the nodes corresponding to the electrode, electrolyte, and the electrode-electrolyte interface (electrolyte node adjacent to electrode node) should be distinguished. Thus, an identification number is assigned to each node depending on whether the node represents the electrode, electrolyte, or electrode-electrolyte interface as shown in Fig. (9.3a).

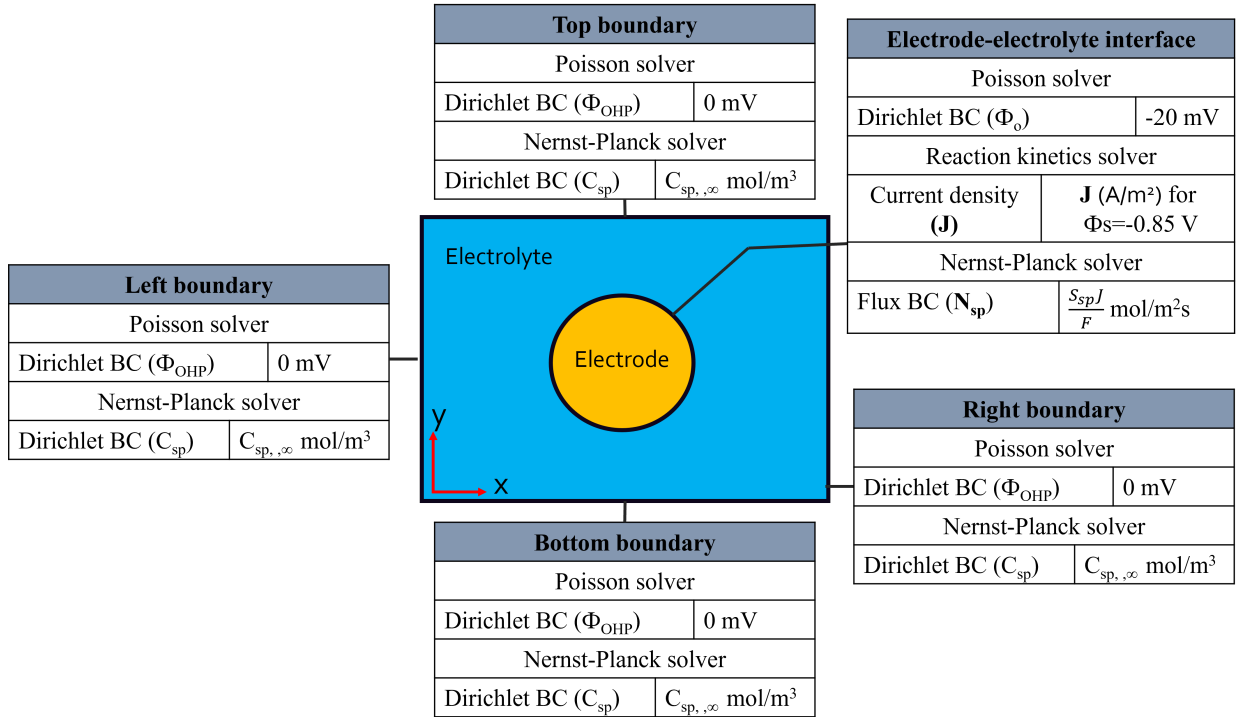


Figure 9.2: Setup of geometry and boundary condition for hydrogen evolution heterogeneous reaction around an electrode catalyst particle.

9.1 Modeling Methodology

The FDM in lattice space to solve Poisson’s equation is straightforward and identical to the approach explained in Chapter 5. The LBM used for the Nernst-Planck model has been slightly modified to model the domain with the solid and liquid nodes. The modified steps are discussed below.

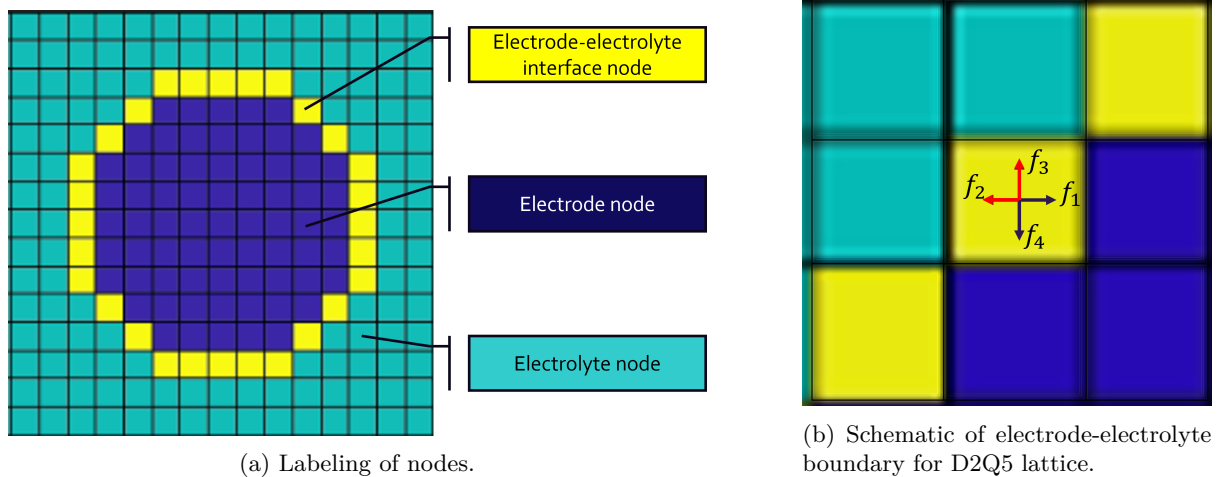


Figure 9.3: (a) Labeling of nodes to distinguish the nodes representing the electrode, electrolyte, and the electrode-electrolyte interface. (b) schematic of electrode-electrolyte boundary for bounce-back treatment of distribution functions.

9.1.1 Bounce-Back

Bounce-back is used to model solid stationary or moving boundary conditions and non-slip conditions. It implies that an incoming particle toward the solid boundary is bounced back into the flow domain. For the example shown in Fig. (9.3b), the functions streaming towards the electrolyte domain are f_2

and f_3 . With the Bounce-back model, these distribution functions are given by

$$f_2 = f_1, \quad f_3 = f_4. \quad (9.1)$$

For a non-reacting boundary condition (adiabatic), the bounce-back model can be used to determine the ion concentration at the electrode-electrolyte nodes when the migrating effect is modeled in the collision operator [43].

9.1.2 Modeling species flux

Since the flux at the electrode-electrolyte interface is directed normally to the surface, the flux vector (radial direction) for each electrode-electrolyte node is resolved into respective x and y components. Then either f_1 or f_2 is estimated to model the x-component and f_3 or f_4 is used to model the vertical component of the flux.

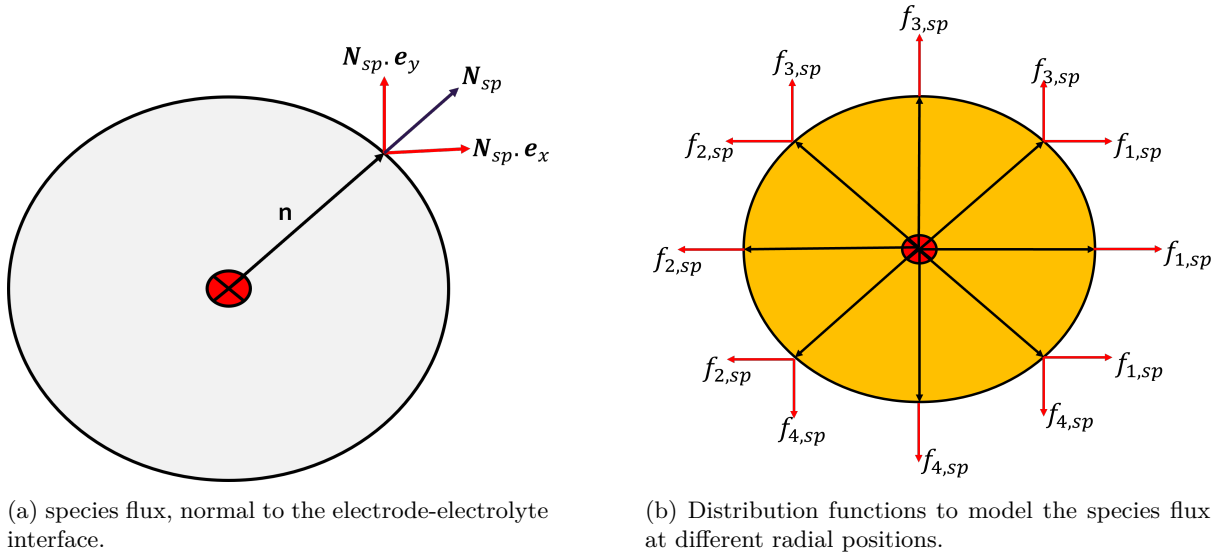


Figure 9.4: (a) Normal species flux to the electrode-electrolyte interface. (b) Choice of the distribution function to model the species flux at different radial positions on the electrode-electrolyte interface.

The expressions to model the appropriate distribution functions streaming towards the domain from the electrode-electrolyte interface can be obtained by extending the methodology used to derive eq. (5.62). The sequence of the steps to simulate the migration-diffusion of the species in the system is given as follows.

- The species concentration and the electric potential at the electrode nodes are set to zero. The electrolyte nodes are initialized with zero electric potential and bulk concentration of respective species given by,

$$C_{H_2O,\infty} = 55500 \text{ mol/m}^3, C_{H_2,\infty} = 10^{-4} \text{ mol/m}^3, C_{OH^-, \infty} = C_{K^+, \infty} = 1 \text{ mol/m}^3. \quad (9.2)$$

- The collision operation is performed as usual, which was explained in chapter 2. The post-collision distribution functions at the electrode-electrolyte interfacial nodes streaming towards the domain are updated using the flux boundary condition model for those distribution functions.
- Then the streaming operation is performed on the electrolyte nodes. The distribution functions at the electrode-electrolyte interfacial nodes are bounced back.
- After the streaming operation, the species concentration is computed at the electrolyte and electrode-electrolyte interfacial nodes using the zeroth-moment of distribution functions given by eq. (5.46). The sequence is repeated in a time loop until the final simulation is reached.

9.2 Results

The electrochemical transportation of the species in hydrogen half cell with the heterogeneous reaction for the domain given in Fig. (9.2) was simulated for a total time of $1 \mu\text{s}$. The simulation results are reported in this section.

9.2.1 Electric potential distribution

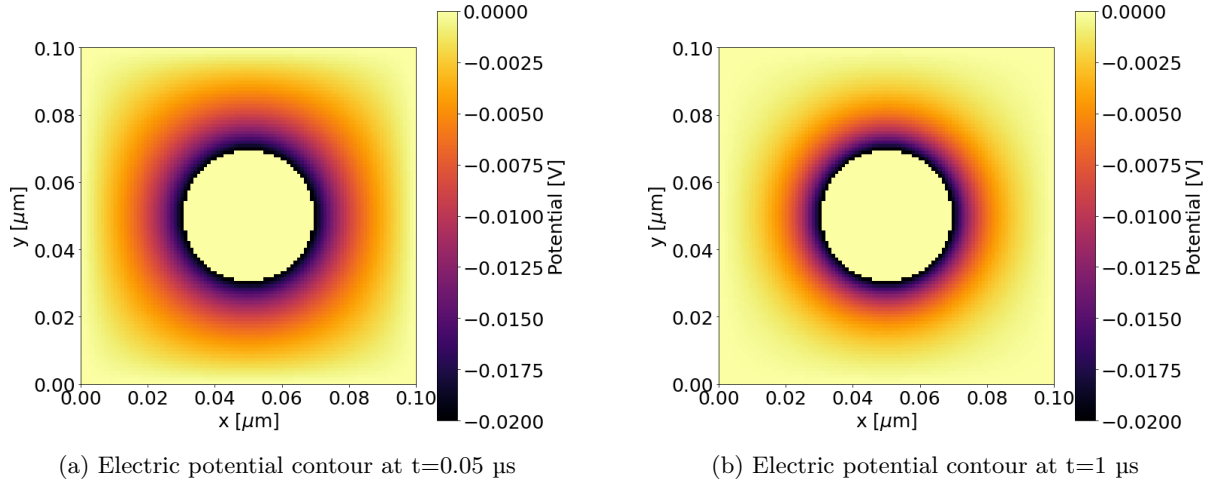


Figure 9.5: Electric potential distribution around the electrode catalyst particle at $t=0.05, 0.1 \mu\text{s}$.

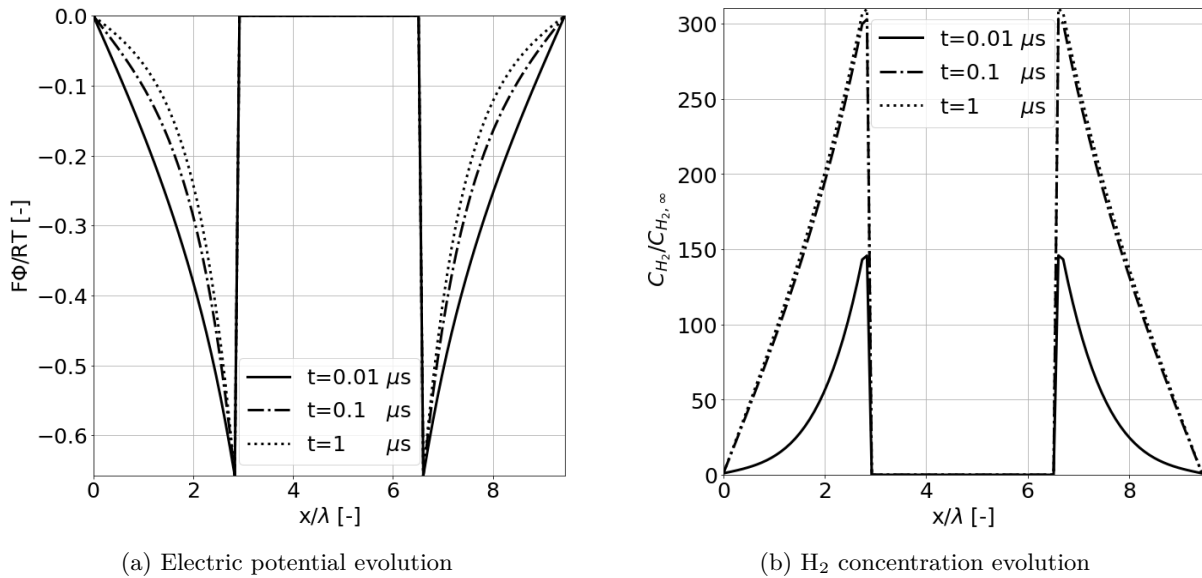


Figure 9.6: (a) Electric potential evolution. (b) H_2 concentration evolution for the electrode surface potential of $\Phi_s = -0.85 \text{ V}$.

The electric potential distribution in the electrolyte around an electrode catalyst particle is given in the Fig. (9.5) and the simulation holds the expected radial symmetry of the distribution. The distribution parallel to the x-axis passing through the center of the electrode is given in Fig. (9.6a). It is seen that the double layer around the electrode grows with time which shields the electric potential from the bulk of the electrolyte. Thus, the electric field across the evolving double layer also increases with time.

9.2.2 Species concentration

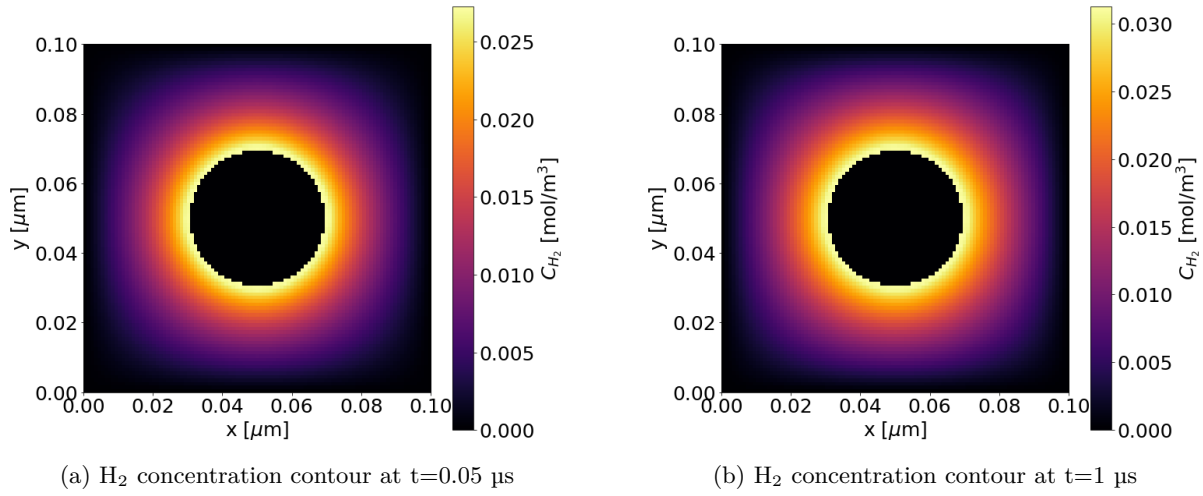


Figure 9.7: H_2 concentration distribution around the electrode catalyst particle at $t=0.05, 0.1 \mu s$.

According to the HER, H_2 is produced at the electrode-electrolyte interface and this results in the increased concentration around the electrode. The mode of transport of H_2 is the diffusive flux that moves it to a low concentration zone. The evolution of H_2 concentration along the axis parallel to the x -axis and passing through the electrode center is given in Fig. (9.6b). It is seen that the H_2 concentration around the electrode increases with time, but the rate of increase in concentration around the electrode decreases with time. This is because at early stages the source flux for H_2 production is higher than the diffusive flux responsible for transporting H_2 to low concentration zones. The diffusive flux evolves until it matches with the source flux at the electrode-electrolyte interface.

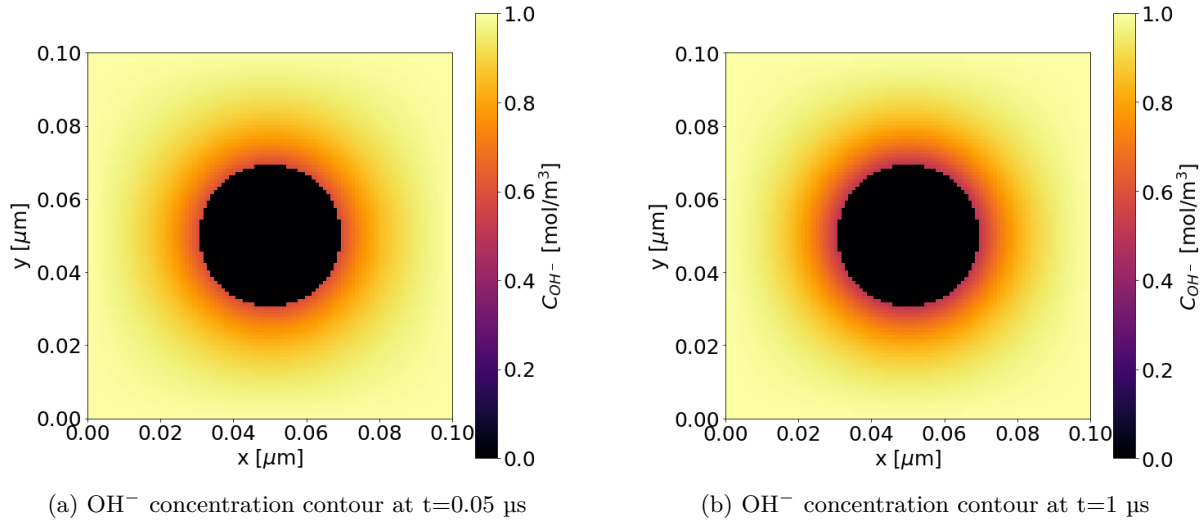


Figure 9.8: OH^- concentration distribution around the electrode catalyst particle at $t=0.05, 0.1 \mu s$.

The negative OHP potential repels the produced OH^- away from the electrode. This results in a lower concentration around the electrode. The mode of transport for OH^- is the migrating and the diffusive fluxes. Though the OH^- is produced at the electrode-electrolyte interface according to HER, the high electric field magnitude results in the migration towards the bulk where the electric field is negligible compared to that in the double layer. From Fig. (9.9a), the concentration of OH^- at the electrode-electrolyte interface decreases until the diffusive flux balances the migrating flux.

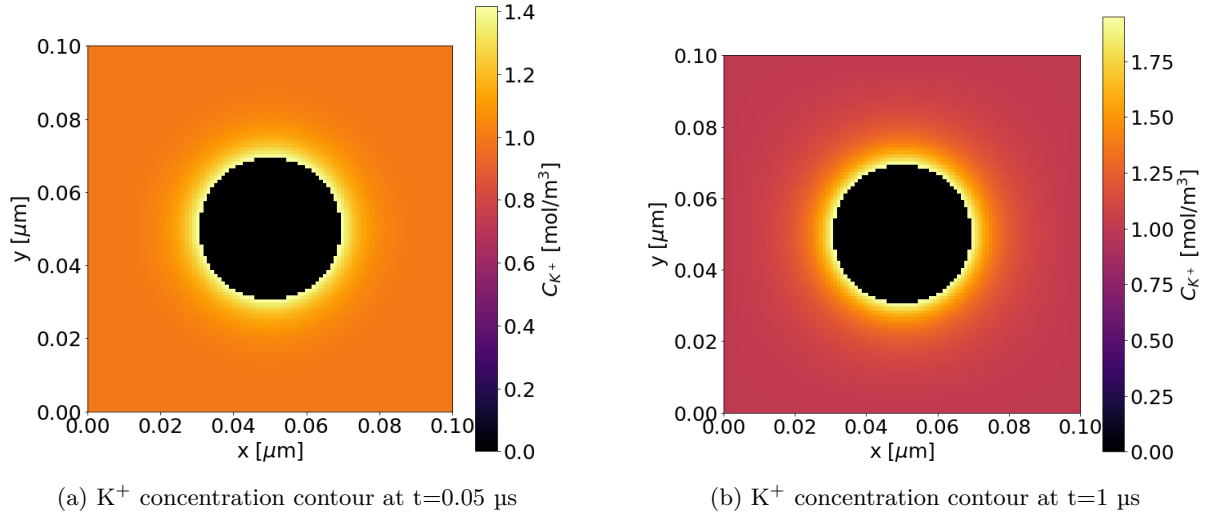


Figure 9.9: K^+ concentration distribution around the electrode catalyst particle at $t=0.05, 0.1 \mu s$.

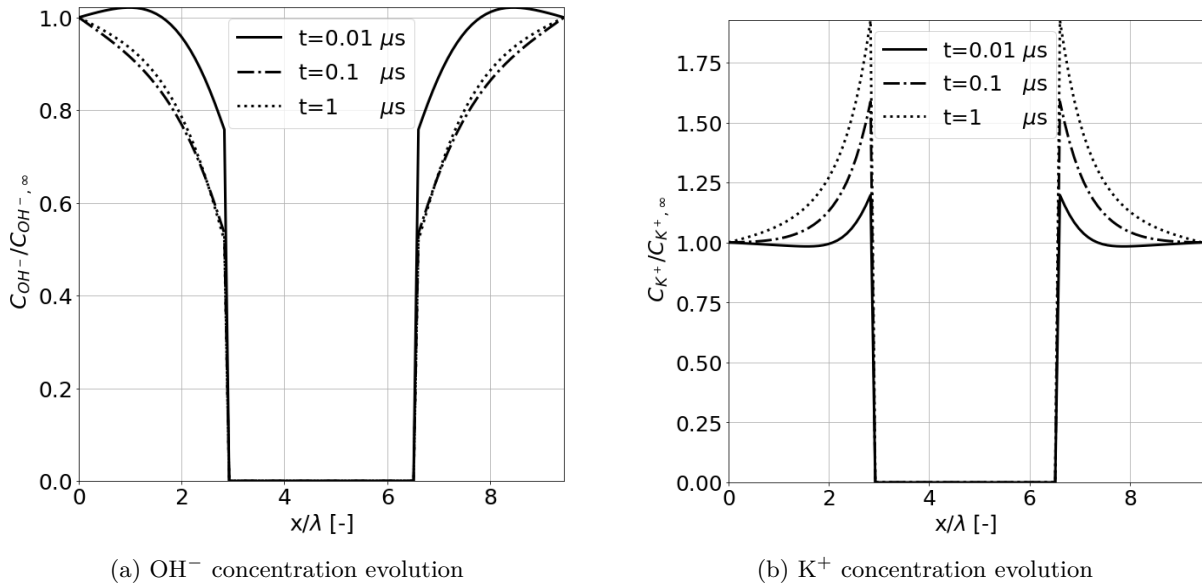


Figure 9.10: (a) OH^- concentration. (b) K^+ concentration evolution for the electrode surface potential of $\Phi_s = -0.85 V$.

The K^+ ions are attracted towards the negative OHP potential resulting in a higher concentration around the electrode. The rate of accumulation around the electrode decreases as the diffusive flux evolves to catch up with the migration flux. This accumulation of the K^+ is responsible for the double layer as the positive charges screen the negative OHP potential.

Thus, the methodology to simulate the species transportation in a domain with solid electrode catalyst is formulated and the simulation results have been studied. The limitation of the above mentioned methodology is that the radial vectors for species flux at the electrode-electrolyte interface are computed for a defined geometry. This method cannot be extended to a irregular geometry because its analytic definition is hard to predict.

Chapter 10

Conclusion and outlook

A hybrid FDM-LBM approach to simulate the transport phenomena with a heterogeneous reaction kinetics model for hydrogen half-cell of alkaline water electrolyzer has been formulated and studied. The Poisson model solves the electric potential distribution using the FDM technique in lattice space. The Pseudo-time LBM is not used for the Poisson solver to reduce the computational time and memory requirement. The BGK-LBM is used to estimate the species transport behavior using the heterogeneous Nernst-Planck model. All the species are modeled with the common evolution time, which is achieved by setting a common reference time (\mathcal{T}) for all the species resulting in species-specific relaxation time (τ_{sp}). This eliminates the internal iteration within the Nernst-Planck solver for each species (faster computation), which ensures that the data of the species transferred to the other solver at a time step are neither over-evolved nor under-evolved. It must be ensured that the relaxation time of the species are within the stability range for the reference scales chosen. Finally, the coupling of the Poisson-Nernst-Planck solver with the local reaction kinetics solver has been formulated.

The formulated methodology that solves the migration-diffusion problem without the reaction is put to the test against the Debye-Hückel theory. Adhering to this theory a domain of length $10 \times \lambda$ and a binary electrolyte was considered with appropriate boundary conditions. The electric potential was taken to be lower than the thermal voltage to ensure that the Debye-Hückel approximation is valid. After performing a grid independence study based on the EDL resolution, the steady-state results from the simulation were compared with the analytical expressions. There existed a good agreement in the distribution of the physical properties. Furthermore, a good agreement was found between the nature of the decay until 5λ . The finite domain size of simulation that violates the assumption of Debye-Hückel theory results in deviation in nature of the distribution function beyond 5λ .

The validated technique has then been used to simulate the transport phenomena in hydrogen Half-cell along with the HER dictated by the Butler-Volmer kinetics equation. To start with the reacting site with a fixed reaction rate was considered (constant \mathbf{J} , no reaction kinetics solver). The evolution of the electric potential, species concentration density, and fluxes has been studied. The shock effects at high electric potential were addressed by ramping it up with time. To overcome the steric effect at high electric potential, the Φ_{OHP} ($\mathcal{O}(\text{mV})$) was used for the Poisson solver, and the kinetics solver uses Φ_s ($\mathcal{O}(\text{V})$) to provide the activation energy for the reaction. The evolution of the kinetic and physical parameters was studied for a set of Φ_s and their results were also compared. It was observed that the accumulation of OH^- outside the EDL increases with the increase in Φ_s due to the increased migration flux across the EDL (outside the EDL, migration flux converges to approx. zero). This results in the inversion of the diffusive flux vector (of OH^-) to diffuse the accumulated OH^- ions from 'outside the EDL' to the bulk. To study the species transport under the influence of the primary and the secondary forces a spatially varying boundary condition was implemented. The ionic species distribution at the crest of the spatial variation that is affected by the counter-electric field along the secondary direction was studied. This scenario could be seen in species transport through a porous media where the EDL of the catalyst particles can overlap with one another resulting in counter-acting electric fields resulting in high OH^- concentration in the overlapping region.

As a starting step to study the species transport through the porous media, the simulation technique to model the migration-diffusion problem with solid-liquid interaction and the surface reaction occurring at the interface is modeled. A single catalyst particle (simplified to a circular shape) is considered for

the simulation, and the treatment of the interfacial nodes, for heterogeneous reaction modeling using BGK-LBM is explained and the results are discussed. This methodology can be extended to understand the species transport through porous media and also get insights about the local properties due to the EDL overlaps.

10.1 Outlook

From the study, the maximum local concentration of H_2 can be increased by raising the over-potential for the HER. Increasing the over-potential increases the kinetic current density resulting in higher source flux for H_2 (aqueous). From figure (7.1), the solubility limit drops with increased system temperature and KOH concentration. Though increasing the over-potential and temperature is forward, the increased KOH concentration would result in the need for a different high-fidelity transport model.

The Nernst-Planck model is suitable for dilute electrolytes where the transport phenomena of the species are independent of each other. But, at high concentration solution, this assumption is not valid and a transport model that accounts for the inter-species interactions has to be used. The Maxwell-Stefan model discussed in Chapter 1 can be used for concentrated electrolytes. Ju'an Huang formulated a Lattice Boltzmann model based on the advection-diffusion equation and is coupled with the Maxwell-Stefan equation by relaxation time [48]. The other issues with the model and the further work toward perfecting it from the perspective of accuracy, robustness, and ease of computation are discussed below.

10.1.1 Steric effects

The classical Poisson Nernst-Planck model that is used in this study which neglects the steric effects due to the finite size limit of the species in the electrolyte. As a result, unphysically high ionic concentration densities are predicted in the EDL at high electrode potential. As a result, this study assumes that a low electric potential at the inner diffuse layer of EDL ($\mathcal{O}(10^{-3})V$) based on the inferences from the literature [43],[47],[49]. Thus, the part of the EDL between the electrode surface and the inner diffuse layer is neglected in this study.

Further, the size-modified Poisson Nernst-Planck (SMPNP) equations that account for the finite size effects in both the Poisson equation and the Nernst-Planck equation can be used to resolve all regions of the EDL and expect a realistic distribution of the species in the EDL. The SMPNP is rooted in a lattice model for the free energy and has been previously utilized in CO_2 electrolysis [46]. The size modification in the Poisson equation is through the relative permittivity of the aqueous electrolyte which is assumed to vary with the local concentration of the cationic species (K^+) given by

$$\epsilon_r = \epsilon_r^o \left[\frac{M_{H_2O} - w_{K^+} C_{K^+}}{M_{H_2O}} \right] + \epsilon_r^{\min} \left[\frac{w_{K^+} C_{K^+}}{M_{H_2O}} \right]. \quad (10.1)$$

Where ϵ_r^o and M_{H_2O} are the relative permittivity at room temperature and molarity (mol/L) of water respectively. $w_{K^+} = 4$ denotes the number of water molecules bound to the cation. The dielectric constant of water at the dielectric saturation condition is denoted by ϵ_r^{\min} . The heterogeneous Nernst-Planck equation with the finite species size correction is given by

$$\frac{\partial C_{sp}}{\partial t} = \nabla \cdot \left[D_{sp} \nabla C_{sp} + \frac{D_{sp} C_{sp} z_{sp} F}{RT} \nabla \Phi + D_{sp} C_{sp} \left(\frac{\beta_{sp} A_n \sum_{j=1}^n a_j^3 \nabla C_j}{1 - A_n \sum_{j=1}^n a_j^3 C_j} \right) \right]. \quad (10.2)$$

The third term from left in the divergence operator is the added term to the Nernst-Planck model for finite species size correction. Here, a_j denotes the effective solvated size of the unhydrated species molecules. The magnification factor of the species relates the species size to that of the solvent species (H_2O) a_o given by

$$\beta_{sp} = \frac{a_{sp}^3}{a_o^3}. \quad (10.3)$$

To model the above equation using the LBM technique, the species velocity is modelled as a combined effect of the migrating flux and the size correction. The species velocity used in the equilibrium distribution

function f_{sp}^{eq} , eq. (3.7) becomes,

$$\mathbf{u}_{sp} = \frac{-D_{sp}z_{sp}F}{RT}\nabla\Phi - D_{sp}\left(\frac{\beta_{sp}A_n\sum_{j=1}^n a_j^3\nabla C_j}{1 - A_n\sum_{j=1}^n a_j^3 C_j}\right). \quad (10.4)$$

Thus, it is recommended to use the SMPNP model to better understand the behavior of the species in the DEL of hydrogen half-cell by extending the LBM technique used in this study.

10.1.2 Multi-relaxation time-LBM

The BGK-LBM technique is used in this work to solve the migration-diffusion problem. Note that the BGK collision operator is not the only possible collision operator. For example, there exist two-relaxation-times (TRT) and multi-relaxation-times (MRT) collision operators that utilize more than just a single relaxation time. (The BGK operator is also often called a single-relaxation-time (SRT) collision operator.) These extended collision operators allow for avoiding or mitigating some limitations of the BGK collision operator, such as stability and accuracy issues. For more details about TRT and MRT-LBM technique it is recommended to refer [40],[42].

10.1.3 Parallel computing

The LBM is more accurate compared to the FDM for complex flows, multi-phase and multi-species systems. However, it is computationally expensive and consumes a large amount of storage depending on the type of lattice configuration preferred for the simulation. Yet LBM is naturally suitable for parallel computing because the particles can be assigned to different processors. This can significantly reduce the computational time required to solve the problem. Due to its direct and highly local update scheme, which requires first-neighborhood information only in its linear streaming part, the LBM is inherently fit for shared-memory as well as large-scale distributed-memory parallelization.

Albeit, the LBM method proposed here, works well for low potential and dilute KOH electrolytic systems. Thus, the solver structure and methodology can be extended to solve the multi-phase problem such as H₂ bubble nucleation and growth by coupling with an appropriate multi-phase model.

Bibliography

- [1] The future of Hydrogen. <https://www.iea.org/reports/the-future-of-hydrogen>.
- [2] green hydrogen technology. <https://www.weforum.org/agenda/2021/07/clean-energy-green-hydrogen/>.
- [3] H-Vision (2019), Annexes to the H-Vision Main Report. <https://www.deltalinqs.nl/h-vision-en>.
- [4] Jude Majasan. “Investigation of Mass Transport Phenomena in Polymer Electrolyte Membrane Water Electrolysers”. In: Oct. 2019.
- [5] Annabelle Brisse, Josef Schefold, and Mohsine Zahid. “High temperature water electrolysis in solid oxide cells”. In: *International Journal of Hydrogen Energy* 33.20 (2008), pp. 5375–5382. ISSN: 0360-3199. DOI: <https://doi.org/10.1016/j.ijhydene.2008.07.120>. URL: <https://www.sciencedirect.com/science/article/pii/S0360319908008355>.
- [6] Dmitri Bessarabov, Haijiang wang, and Nana Zhao. PEM Electrolysis for Hydrogen Production: Principles and Applications. Jan. 2015.
- [7] RL LeRoy. “Industrial water electrolysis: present and future”. In: *International Journal of Hydrogen Energy* 8.6 (1983), pp. 401–417.
- [8] Jesús Rodríguez and Ernesto Amores. “CFD modeling and experimental validation of an alkaline water electrolysis cell for hydrogen production”. In: *Processes* 8.12 (2020), p. 1634.
- [9] Tahir, Tahir Abdul Hussain Ratlamwala, and Ibrahim Dincer. “Electrochemical, energy, exergy and exergoeconomic analyses of hybrid photocatalytic hydrogen production reactor for Cu-Cl Cycle”. In: Apr. 2015.
- [10] Xu Zhao, Hang Ren, and Long Luo. “Gas bubbles in electrochemical gas evolution reactions”. In: *Langmuir* 35.16 (2019), pp. 5392–5408.
- [11] Yan-Hom Li and Yen-Ju Chen. “The effect of magnetic field on the dynamics of gas bubbles in water electrolysis”. In: *Scientific reports* 11.1 (2021), pp. 1–12.
- [12] Dongke Zhang and Kai Zeng. “Evaluating the Behavior of Electrolytic Gas Bubbles and Their Effect on the Cell Voltage in Alkaline Water Electrolysis”. In: *Industrial & Engineering Chemistry Research* 51.42 (2012), pp. 13825–13832. DOI: [10.1021/ie301029e](https://doi.org/10.1021/ie301029e). eprint: <https://doi.org/10.1021/ie301029e>. URL: <https://doi.org/10.1021/ie301029e>.
- [13] Kai Zeng and Dongke Zhang. “Recent progress in alkaline water electrolysis for hydrogen production and applications”. In: *Progress in energy and combustion science* 36.3 (2010), pp. 307–326.
- [14] Cheng-Chien Wang, Chuh-Yung Chen, et al. “Water electrolysis in the presence of an ultrasonic field”. In: *Electrochimica Acta* 54.15 (2009), pp. 3877–3883.
- [15] Takami Iida, Hisayoshi Matsushima, and Yasuhiro Fukunaka. “Water electrolysis under a magnetic field”. In: *Journal of the electrochemical society* 154.8 (2007), E112.
- [16] Mingyong Wang, Zhi Wang, and Zhancheng Guo. “Water electrolysis enhanced by super gravity field for hydrogen production”. In: *International Journal of Hydrogen Energy* 35.8 (2010), pp. 3198–3205.
- [17] Daisuke Kiuchi et al. “Ohmic resistance measurement of bubble froth layer in water electrolysis under microgravity”. In: *Journal of The Electrochemical Society* 153.8 (2006), E138.

- [18] H Matsushima, Y Fukunaka, and K Kuribayashi. “Water electrolysis under microgravity: Part II. Description of gas bubble evolution phenomena”. In: *Electrochimica acta* 51.20 (2006), pp. 4190–4198.
- [19] Emily M Ryan and Partha P Mukherjee. “Mesoscale modeling in electrochemical devices—A critical perspective”. In: *Progress in Energy and Combustion Science* 71 (2019), pp. 118–142.
- [20] Xiaoyi He and Ning Li. “Lattice Boltzmann simulation of electrochemical systems”. In: *Computer Physics Communications* 129.1-3 (2000), pp. 158–166.
- [21] WKS Chiu, AS Joshi, and KN Grew. “Lattice Boltzmann model for multi-component mass transfer in a solid oxide fuel cell anode with heterogeneous internal reformation and electrochemistry”. In: *The European Physical Journal Special Topics* 171.1 (2009), pp. 159–165.
- [22] DA Aikens. *Electrochemical methods, fundamentals and applications*. 1983.
- [23] John Newman and Karen E Thomas-Alyea. *Electrochemical systems*. John Wiley & Sons, 2012.
- [24] G. Rocchini. “The determination of tafel slopes by the successive approximation method”. In: *Corrosion Science* 37.6 (1995), pp. 987–1003. ISSN: 0010-938X. DOI: [https://doi.org/10.1016/0010-938X\(95\)00009-9](https://doi.org/10.1016/0010-938X(95)00009-9). URL: <https://www.sciencedirect.com/science/article/pii/S0010938X95000099>.
- [25] Kenjiro Torii, Manabu Kodama, and Shuichiro Hirai. “Three-dimensional coupling numerical simulation of two-phase flow and electrochemical phenomena in alkaline water electrolysis”. In: *International Journal of Hydrogen Energy* 46.71 (2021), pp. 35088–35101.
- [26] Edmund JF Dickinson and Gareth Hinds. “The Butler-Volmer equation for polymer electrolyte membrane fuel cell (PEMFC) electrode kinetics: a critical discussion”. In: *Journal of the electrochemical society* 166.4 (2019), F221.
- [27] Jaeseung Lee, Afroz Alam, and Hyunchul Ju. “Multidimensional and transient modeling of an alkaline water electrolysis cell”. In: *International Journal of Hydrogen Energy* 46.26 (2021), pp. 13678–13690.
- [28] Dawn M Bernardi and Mark W Verbrugge. “A mathematical model of the solid-polymer-electrolyte fuel cell”. In: *Journal of the Electrochemical Society* 139.9 (1992), p. 2477.
- [29] S Langlois and F Coeuret. “Flow-through and flow-by porous electrodes of nickel foam. I. Material characterization”. In: *Journal of applied electrochemistry* 19.1 (1989), pp. 43–50.
- [30] E Potvin and L Brossard. “Electrocatalytic activity of Ni-Fe anodes for alkaline water electrolysis”. In: *Materials chemistry and physics* 31.4 (1992), pp. 311–318.
- [31] J_Y Huot, ML Trudeau, and R Schulz. “Low hydrogen overpotential nanocrystalline Ni-Mo cathodes for alkaline water electrolysis”. In: *Journal of The Electrochemical Society* 138.5 (1991), p. 1316.
- [32] Seyeong Lee et al. “Operational durability of three-dimensional Ni-Fe layered double hydroxide electrocatalyst for water oxidation”. In: *Electrochimica Acta* 315 (2019), pp. 94–101.
- [33] Diogo MF Santos, César AC Sequeira, and José L Figueiredo. “Hydrogen production by alkaline water electrolysis”. In: *Quimica Nova* 36 (2013), pp. 1176–1193.
- [34] Slobodan Petrovic. *Electrochemistry Crash Course for Engineers*. Springer, 2021.
- [35] Sona Aseyednezhad et al. “An accurate reduced-dimension numerical model for evolution of electrical potential and ionic concentration distributions in a nano-scale thin aqueous film”. In: *Advances in Water Resources* 159 (2022), p. 104058.
- [36] Tomasz Sokalski and Andrzej Lewenstam. “Application of Nernst–Planck and Poisson equations for interpretation of liquid-junction and membrane potentials in real-time and space domains”. In: *Electrochemistry communications* 3.3 (2001), pp. 107–112.
- [37] Markku J Lampinen and Marina Fomino. “Analysis of free energy and entropy changes for half-cell reactions”. In: *Journal of the Electrochemical Society* 140.12 (1993), p. 3537.
- [38] Min J Tham, Robert Dixon Walker Jr, and Keith E Gubbins. “Diffusion of oxygen and hydrogen in aqueous potassium hydroxide solutions”. In: *The Journal of Physical Chemistry* 74.8 (1970), pp. 1747–1751.
- [39] Venkatasubramanian Viswanathan et al. “Universality in oxygen reduction electrocatalysis on metal surfaces”. In: *Acs Catalysis* 2.8 (2012), pp. 1654–1660.

- [40] AA Mohamad. Lattice boltzmann method. Vol. 70. Springer, 2011.
- [41] XD Niu et al. “Investigation of stability and hydrodynamics of different lattice Boltzmann models”. In: *Journal of statistical physics* 117 (2004), pp. 665–680.
- [42] Timm Krüger et al. “The lattice Boltzmann method”. In: *Springer International Publishing* 10.978-3 (2017), pp. 4–15.
- [43] Rui Liu et al. “Pore-scale study of dynamic ion adsorption process in porous electrodes of capacitive deionization using lattice Boltzmann method”. In: *International Journal of Heat and Mass Transfer* 135 (2019), pp. 769–781.
- [44] CG Gray and Peter John Stiles. “Nonlinear electrostatics: the Poisson–Boltzmann equation”. In: *European Journal of Physics* 39.5 (2018), p. 053002.
- [45] Parsa Habibi et al. “A new force field for OH–for computing thermodynamic and transport properties of H₂ and O₂ in aqueous NaOH and KOH solutions”. In: *The Journal of Physical Chemistry B* 126.45 (2022), pp. 9376–9387.
- [46] Esaar Naeem Butt, Johan T Padding, and Remco Hartkamp. “Size-modified Poisson–Nernst–Planck approach for modeling a local electrode environment in CO₂ electrolysis”. In: *Sustainable Energy & Fuels* 7.1 (2023), pp. 144–154.
- [47] Li Zhang and Moran Wang. “Modeling of electrokinetic reactive transport in micropore using a coupled lattice Boltzmann method”. In: *Journal of Geophysical Research: Solid Earth* 120.5 (2015), pp. 2877–2890.
- [48] Ju’an Huang et al. “A combined approach of Lattice Boltzmann Method and Maxwell-Stefan equation for modeling multi-component diffusion in solid oxide fuel cell”. In: *arXiv preprint arXiv:1809.01600* (2018).
- [49] Hiroaki Yoshida, Tomoyuki Kinjo, and Hitoshi Washizu. “Coupled lattice Boltzmann method for simulating electrokinetic flows: A localized scheme for the Nernst–Planck model”. In: *Communications in Nonlinear Science and Numerical Simulation* 19.10 (2014), pp. 3570–3590.

Appendix A

Results for $\Phi_s = [-0.75, -0.85, -0.9]$ V

A.1 Surface potential $\Phi_s = -0.9$ V

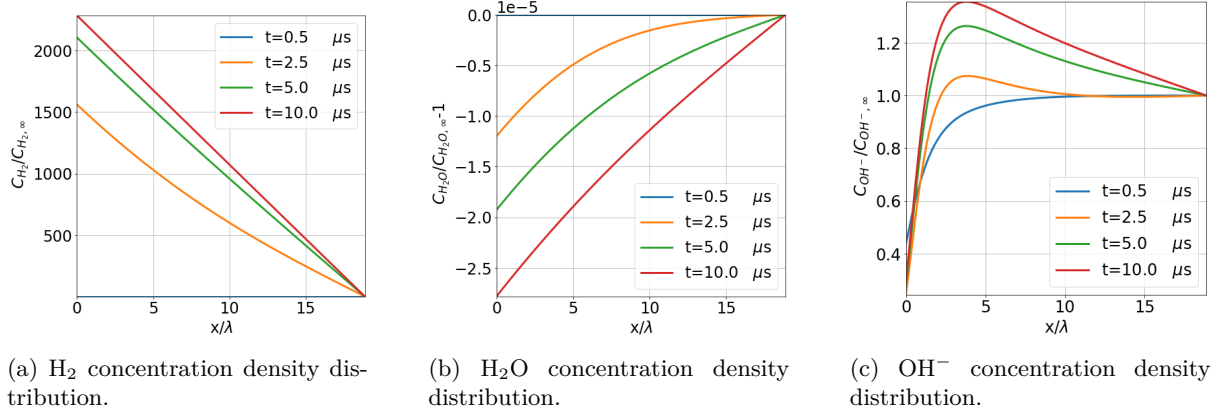


Figure A.1: Species concentration evolution for $\Phi_s = -0.9$ V and $\Phi_{OHP} = -50$ mV.

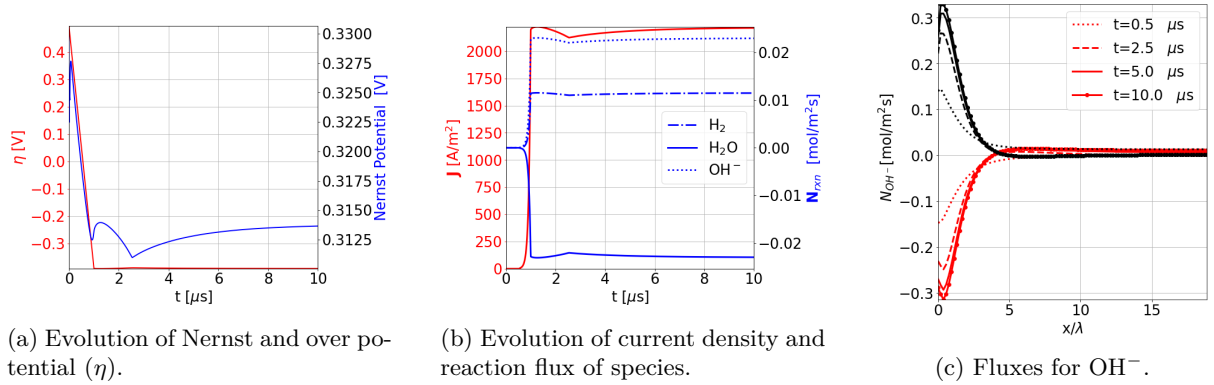
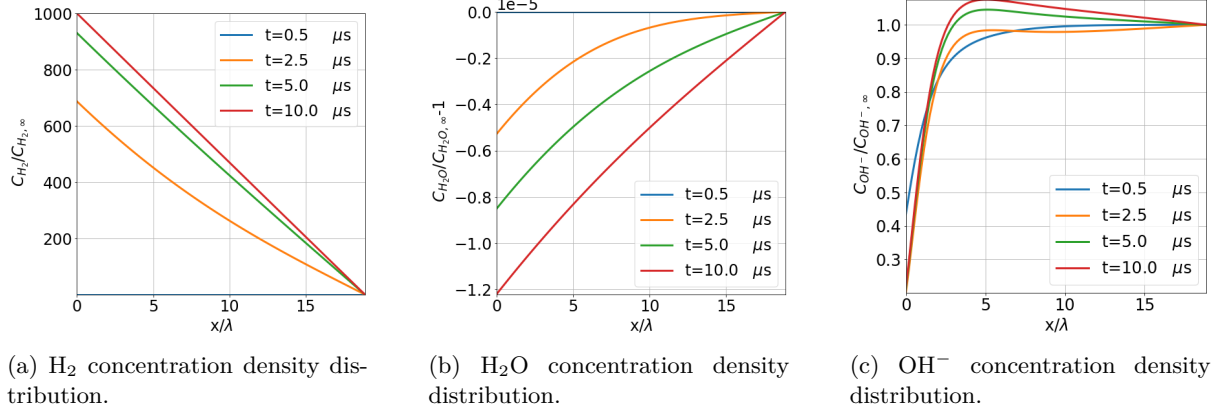
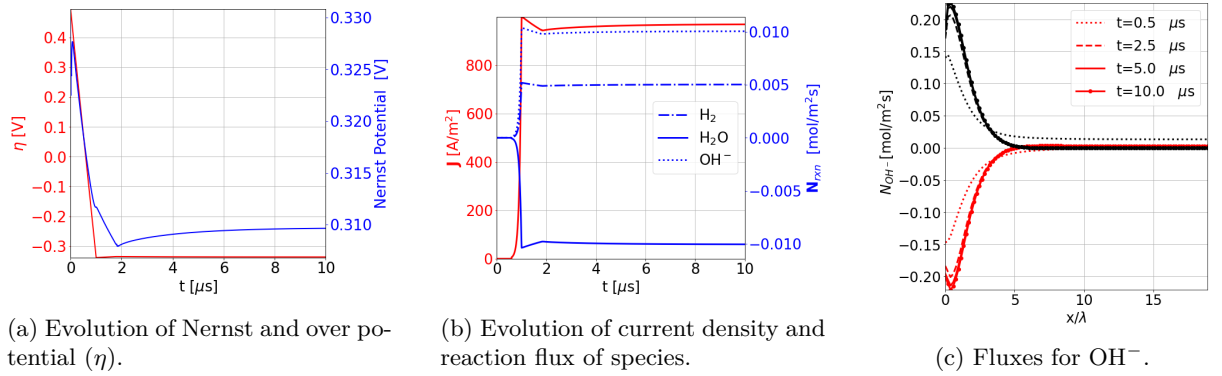
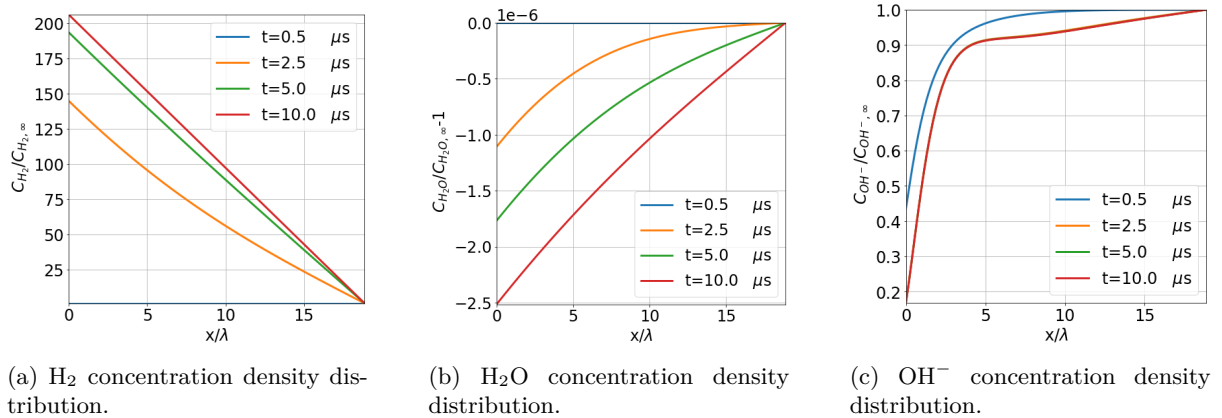


Figure A.2: Evolution of the over and Nernst potential, current density and species reaction flux at reacting boundary, flux evolution of OH^- for $\Phi_s = -0.9$ V and $\Phi_{OHP} = -50$ mV

A.2 For surface potential $\Phi_s = -0.85$ V


 Figure A.3: Species concentration evolution for $\Phi_s = -0.85$ V and $\Phi_{\text{OHP}} = -50$ mV.

 Figure A.4: Evolution of the over and Nernst potential, current density and species reaction flux at reacting boundary, flux evolution of OH^- for $\Phi_s = -0.85$ V and $\Phi_{\text{OHP}} = -50$ mV

A.3 For surface potential $\Phi_s = -0.75$ V


 Figure A.5: Species concentration evolution for $\Phi_s = -0.75$ V and $\Phi_{\text{OHP}} = -50$ mV.

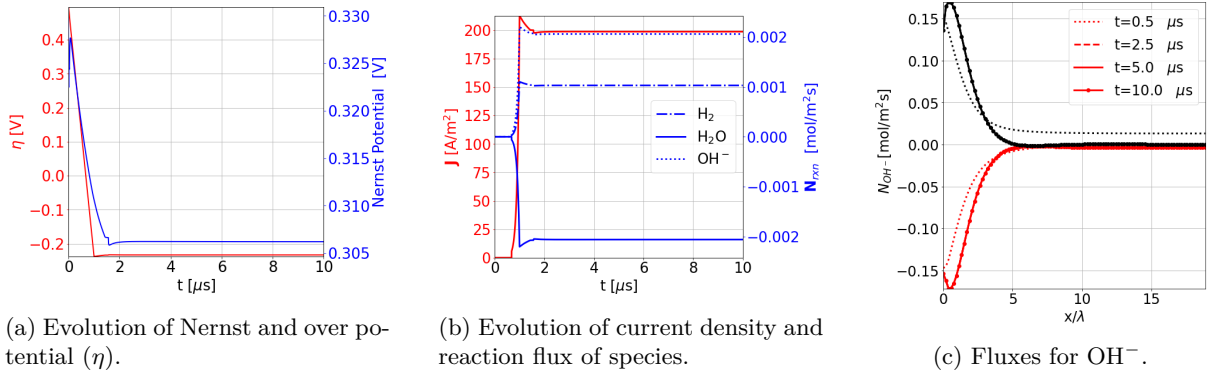


Figure A.6: Evolution of the over and Nernst potential, current density and species reaction flux at reacting boundary, flux evolution of OH^- for $\Phi_s = -0.75$ V and $\Phi_{\text{OHP}} = -50$ mV

Appendix B

Spatially varying Boundary condition

B.1 Potential distribution

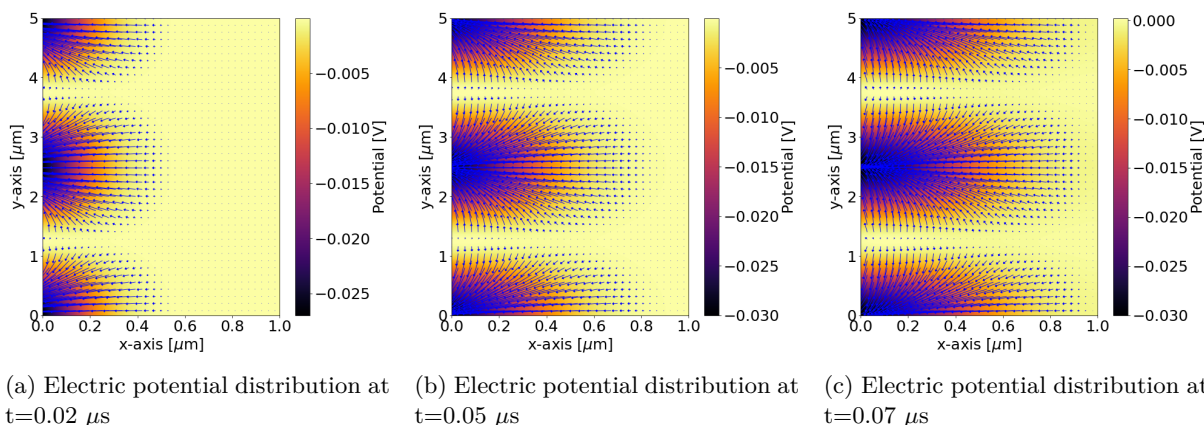


Figure B.1: Electric potential distribution between the inner diffuse layer and the right boundary (bulk) and the vector plot for electric field distribution at $t=0.02, 0.05, 0.07 \mu\text{s}$.

B.2 H_2 concentration density

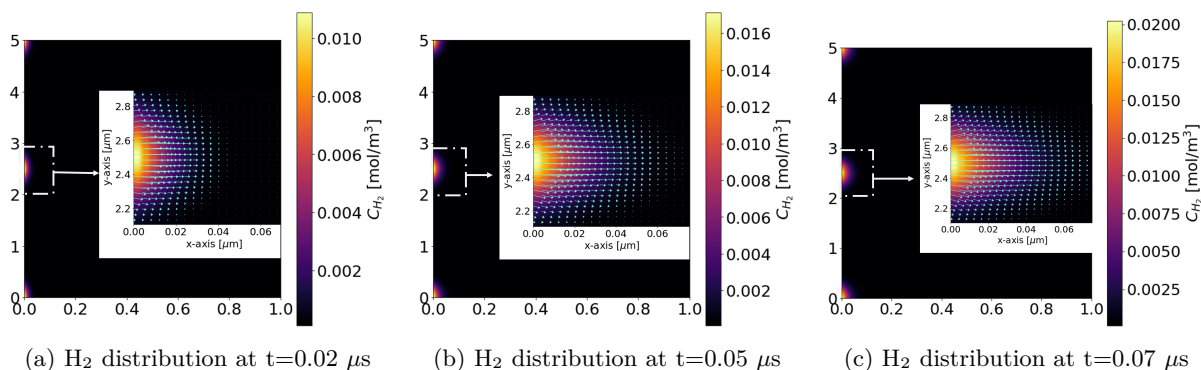
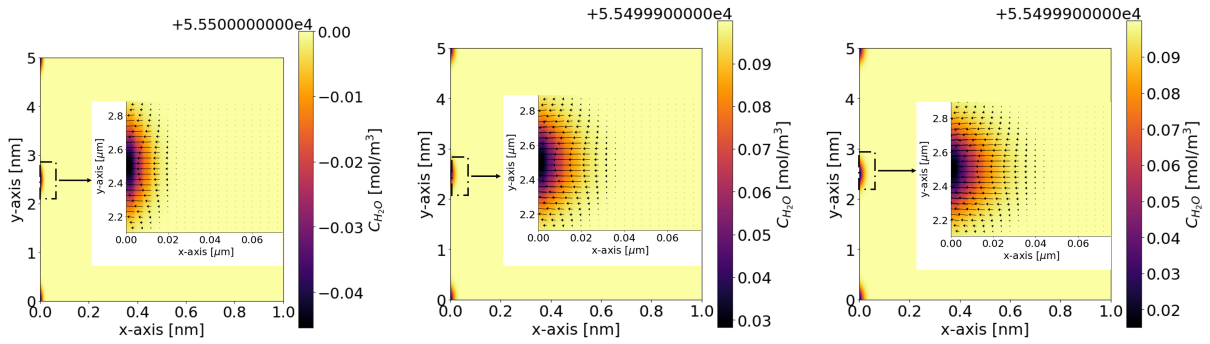


Figure B.2: Local concentration density of H_2 and the vector plot for flux at $t=0.02, 0.05, 0.07 \mu\text{s}$

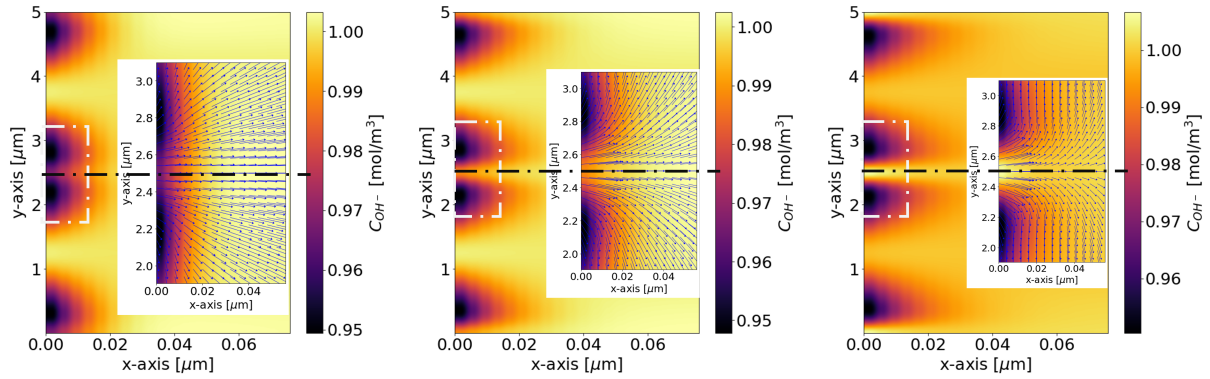
B.2.1 H₂O concentration density



(a) H₂O distribution at $t=0.02 \mu s$ (b) H₂O distribution at $t=0.05 \mu s$ (c) H₂O distribution at $t=0.07 \mu s$

Figure B.3: Local concentration density of H₂O and the vector plot for flux at $t=0.02,0.05,0.07 \mu s$

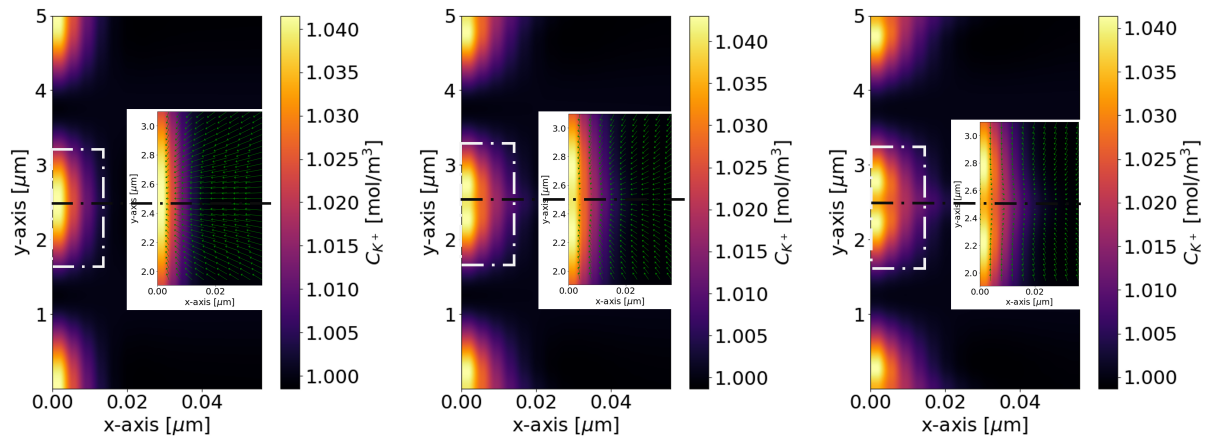
B.3 OH⁻ concentration density



(a) OH⁻ distribution at $t=0.02 \mu s$ (b) OH⁻ distribution at $t=0.05 \mu s$ (c) OH⁻ distribution at $t=0.07 \mu s$

Figure B.4: Local concentration density of OH⁻ and the vector plot for flux at $t=0.02,0.05,0.07 \mu s$

B.4 K⁺ concentration density



(a) K⁺ distribution at $t=0.02 \mu s$ (b) K⁺ distribution at $t=0.05 \mu s$ (c) K⁺ distribution at $t=0.07 \mu s$

Figure B.5: Local concentration density of K⁺ and the vector plot for flux at $t=0.02,0.05,0.07 \mu s$.